DOCTORAL THESIS

Petr Pospíšil

Fluorescence Spectroscopy: Advanced methods and their defined applications in protein science

Department of Biophysical Chemistry
J. Heyrovský Institute of Physical Chemistry of the CAS, v. v. i.

Supervisor of the doctoral thesis: Prof. Martin Hof, Ph.D., DSc.

Study programme: Physics

Specialization: Biophysics, Chemical and Macromolecular Physics

Prague 2017

I declare that I carried out this doctoral thesis independently, and only with the cited sources, literature and other professional sources.

I understand that my work relates to the rights and obligations under the Act No. 121/2000 Coll., the Copyright Act, as amended, in particular the fact that the Charles University in Prague has the right to conclude a license agreement on the use of this work as a school work pursuant to Section 60 paragraph 1 of the Copyright Act.

In Bzí 8.5.2017   Petr Pospíšil

Title: Fluorescence Spectroscopy: Advanced methods and their defined applications in protein science

Author: Petr Pospíšil

Department / Institute: Department of Biophysical Chemistry, J. Heyrovský Institute of Physical Chemistry of the CAS, v. v. i.,

Supervisor of the doctoral thesis: Prof. Martin Hof, Ph.D., DSc., Department of Biophysical Chemistry, J. Heyrovský Institute of Physical Chemistry of the CAS, v. v. i.,

Abstract:

The hydration and dynamics of the biomolecules appear to be vital for their proper biological functioning. In the presented thesis, various fluorescence techniques were developed and applied to access these properties and their changes upon the mutual interactions of the biomolecules. Initially, the solvent relaxation method based on recording time-dependent fluorescence shift (TDFS) was used to map DNA interactions with proteins and lipids by the newly synthesised fluorene dye covalently bound to the DNA. Secondly, copper-transporting ATPase was probed by Badan attached to the copper-binding cysteine-proline-cysteine motif. The variations in hydration were found to be crucial for the proper ATPase function. Third, a detailed study on quenching of Badan/Prodan fluorescence by tryptophan revealed the limitations of the TDFS method for protein studies, which is essential finding for further applications of TDFS. Fourth application involves investigations of heavy atom effects on the excited state relaxation processes by up-conversion approach in iodinated metallocorroles, which are promising dyes for biological imaging. The obtained findings shall help in further tuning of the optical properties of the corroles desired for the variety of applications. Finally, fluorescence correlation spectroscopy revealed surprising cooperation effects during the incorporation of two antimicrobial peptides, PGLa and Mag2, into the membrane.

Keywords: Solvent relaxation, Fluorescence correlation spectroscopy, Up-conversion, copper-transporting ATPase, metallocorroles.

Acknowledgements:

Contents

Introduction

The term fluorescence was first coined by G.G. Stokes, when he published his observation of fluorescence in quinine sulphate solution in 1852. Although, he was not the first person in history who observed the phenomenon of fluorescence, he is considered the first one who proposed fluorescence as an analytical tool. Since then people have discovered and developed a variety of new fluorescent dyes, techniques and applications. Biology has become one of the main field where fluorescence is applied mainly due to sensitivity and non-invasiveness of fluorescence techniques. Recent years have witnessed rapid growth of popularity of fluorescence methods in biology as well as the vast development of fluorescence probe technology and instrumentation. This effort, among many other scientific achievements, was recognized with the Nobel Prize in Chemistry in 2014 for a super-resolution fluorescence microscopy.

The main goal of this work is to present advanced fluorescent methods: time-resolved fluorescence spectroscopy and fluorescence correlation spectroscopy, together with their five selected applications mainly in protein science (chapter 3). These methods have been using for a long time, nevertheless, their application possibilities are still not fully explored.

The main part of this work deals with protein and DNA dynamics in a combination with environment-sensitive fluorescent dyes. The method of choice for studying such biomolecular interactions is a solvent relaxation technique. Fluorophores containing push-pull electron-donating and electron-withdrawing groups attached to a polarizable π-electronic system typically exert solvatochromic properties. They undergo intramolecular charge transfer in the excited state resulting in increased dipole moment of the molecule. Consequently, mainly due to the dipole-dipole interactions between the excited dye and its surroundings, solvatochromic dyes can report on a local hydration and dynamics in proteins, lipid membranes and cellular organelles, which are often associated with certain biological events.

In this work, time-dependent fluorescence shift (TDFS), determined by time-correlated single photon counting, was employed in order to reveal the solvent relaxation characteristics of short double stranded DNA and a membrane protein. In the first case, DNA was labelled with newly synthesised fluorescent 2′-deoxycytidine

nucleoside linked to a highly solvatochromic fluorene derivative (section 3.1). The fluorene-linked DNA was then used as a fluorescent probe for investigation of DNA-protein and DNA-lipid interactions. The latter is of great interest for investigation of the gene transfer into the cells.

In the second case, the investigation of the functional role of water entry into the transmembrane region of the copper-transporting P$_{IB}$-type ATPase (section 3.3), was investigated using polarity-sensitive fluorophore 6-bromoacetyl-2-dimethylamino-naphthalene (Badan) bound to the defined position within the protein scaffold (copper-binding cysteine-proline-cysteine motif). Water hydration plays essential role in the structure, stability, and dynamics of biomolecules. Hydration is particularly important for membrane proteins that facilitates transport of ions across lipid bilayer. Hydration shell of a solvated ion needs to be rearranged and partially removed in order to bind an ion within the protein scaffold before it is re-solvated upon exiting the membrane protein. Therefore, understanding membrane proteins function one has to know to what extent water is hydrating the crucial parts of these proteins.

Apart from the advantage of probing the desired spot within the protein scaffold, there are also interfering processes that might preclude the successful solvent relaxation measurements. One of such interfering processes, fluorescence quenching of Badan by tryptophan, is address in the section 3.2.

The fourth study investigates versatile fluorescence probes: iodinated corroles (section 3.4). Corroles are promising candidates for variety of spectroscopic applications mainly due to their tuneable optical properties. Moreover, they spontaneously form tightly bound conjugates with proteins which makes them interesting fluorophores for solvatochromic studies. Upon iodination, corroles exhibit microsecond phosphorescence in the near infrared part of the spectra which can be used to circumvent the most common obstacles to efficient biological imaging: tissue absorbance and intrinsic fluorescence. In order to specifically tune the properties of the corroles, one needs to understand the excited state relaxation process. However, emission decays of all iodinated complexes are too fast to be measured by time-correlated single photon counting to investigate ultrafast excited state dynamics. Therefore, fluorescence up-conversion with a femtosecond time resolution were employed for this purpose.

Application of fluorescence correlation spectroscopy to the study of two antimicrobial peptides is the last example of application of advanced fluorescent

methods in this work (section 3.5). Increasing bacterial antibiotic resistance has grown into one of the major threat to public health, however, antimicrobial peptides, the evolutionary ancient weapons, seems to be feasible way how to fight pathogens. The main reason is that antimicrobial peptides directly attack bacterial membrane and this makes the bacterial resistance almost improbable. However, the precise mechanisms of how the antimicrobial peptides kill bacteria is still unclear. In this part of the work, the surprising cooperation effects during the incorporation of two antimicrobial peptides, PGLa and Mag2, into the membrane are revealed.

The diversity of research topics presented in this work, attempts to demonstrate the versatility, application potential and significance of the employed advanced fluorescent methods in biophysics and biology. These methods, together with the instrumentations used, are briefly described in chapter 2. It is also common practice to outline the theory of the physical processes behind the selected methods. Fluorescence is the phenomenon which arises due to the interaction of the incident light and the sample. Since the theory of interaction of light and matter is broad and well known for decades, only the most important concepts sufficient for the explanation of the physical mechanisms and interpretation of the obtained results are described in chapter 1.

1. Interaction of light and matter

To understand interaction of light and matter, it is important to realize that processes like scattering or absorption arise from accelerating electrical charge.

Classically, one can explain this acceleration as a result of an oscillating electrical field of light resonantly interacting with charged particles. When a material exposed to light consists of single atoms or molecules, e.g. hydrogen gas or quinine solution, electrons start to oscillate within a nuclear framework of these atoms or molecules. This movement corresponds to oscillations of an electrical dipole that may absorb and eventually may re-emit energy. Thus, we can imagine the interaction of light and matter as a process in which energy is exchanged between the oscillating dipoles (electrons) and electromagnetic radiation (oscillating electrical field) [1].

Quantum mechanically, electrons in an atom or a molecule can exist in certain quantum states, that can be described by wavefunctions, where each of these states is associated with definite energy. For spectroscopy, the most interesting are the ground and excited electronic states. They are stationary states described by a specific set of wavefunctions called basis set. When light encounters an atom or a molecule, it perturbs their stationary state. The state of the system can be then expressed as a superposition of the ground and excited states, represented as a linear combination of the basis functions. Such system possess oscillating dipole but now represented as an oscillatory component of the dipole in a superposition of the ground and excited states [2]. The oscillating dipole can be related to a physical property called the transition dipole moment, which can be physically interpreted as a measure of the magnitude of the migration of charge that accompanies the transition from the ground to the excited state [3]. Transition from the ground to the excited state can happen provided the resonance condition is fulfilled, i.e. the energy of incident light corresponds to the energy gap between these two states.

Both classical and quantum mechanical concepts contain two significant approximations. First, the magnetic component of electromagnetic radiation is neglected. This approximation is acceptable because the effects of the magnetic field are usually much lower than the effects of the electrical field. Second, the amplitude of the electric component is considered constant for every possible position of interacting electrons; i.e. we can usually neglect higher order interactions (e.g. quadrupole, octupole, etc.) between electrical field and molecules. This approximation

is reasonable for atoms and most molecules (e.g. fluorophores), because they are typically small relative to the wavelength of visible light.

Although both concepts describe sufficiently well the underpinnings of the processes during spectroscopic transitions, the most common approach is to treat matter quantum mechanically with the time-dependent perturbation theory and light, the perturbation, as a classical oscillating electric field [2].

1.1 Transition dipole moment and oscillator strength

The two concepts, classical and quantum mechanical, can be connected through two important terms, which both describe the strength of an absorption band: aforementioned transition dipole moment and oscillator strength. We can define transition dipole moment as:

$$\mu_{fi} = \langle \psi_f | \hat{\mu} | \psi_i \rangle = \int \psi_f^* \hat{\mu} \psi_i dR \qquad (1.1)$$

where $\hat{\mu}$ is the dipole operator, ψ_f and ψ_i are the wavefunctions of the final and initial states, respectively. ψ_f^* is the complex conjugate of ψ_f and dR is the volume element. The square modulus of the transition dipole moment is proportional to the intensity of the transition. We can decide by evaluating the integral whether a particular transition can occur or not and formulate selection rules based on a spatial symmetry of a system. Transitions formally forbidden by the symmetry with the dipole operator can be sometimes weakly allowed by the quadrupole or octupole terms. In the case of a molecule, vibrational motions can perturb the symmetry or change the linear combination of wavefunctions contributing to the excited state. Then, this so-called vibronic coupling, can promote forbidden transitions as well. Last but not least, some transitions with small electric transition dipole moments can be driven by the magnetic field of light [2].

The oscillator strength is a dimensionless quantity that can range from 0 to 1. It characterises magnitude of the intensity of the transition compared to the intensity of an ideal classical isotropic electron oscillator, which has oscillator strength one. Therefore, oscillator strength is a useful quantity for comparing different transitions and it is often used to quantify transitions in newly synthetized fluorescent dyes. Furthermore, the theoretical quantity of the oscillator strength in the classical theory

of light absorption is directly related to the experimental quantity of the extinction coefficient of absorption (ε). The practical form of this relation is [3]:

$$f = 6.257 \times 10^{-19} \frac{\int \varepsilon(v) dv}{m^2 mol^{-1} s^{-1}} \tag{1.2}$$

where v is the frequency, ε is the molar extinction coefficient that expresses the ability of a molecule to absorb light in a given solvent and the integral of the extinction coefficient is the area of the absorption band. Finally, the oscillator strength can be related to the transition dipole moment, thus linking the classical theory with quantum mechanics. This connection can be expressed as follows [4]:

$$f = \frac{8\pi^2 m_e v_{fi}}{3e^2 h} |\mu_{fi}|^2 \tag{1.3}$$

where m_e is the electron mass, v_{fi} is the frequency of a transition, e is the electron charge and h is the Planck constant.

1.2 Absorption

Till now, mainly the effects of light on electrons in atoms and molecules were discussed. However, the nuclei need to be included in the case of molecules in order to obtain correct wavefunction for the description of the molecular states. Because nuclei have much larger masses compared to electrons and consequently motions of electrons are much more rapid than those of nuclei, it is reasonable to assume nuclei as more or less fixed in their positions during the transition. This assumption is the very well-known Born-Oppenheimer approximation and it allows to treat motions of electrons and nuclei separately, when solving Schrödinger equation. As a result of an electron transition (excitation), electron density is almost instantaneously shifted (10^{-15} s) from its equilibrium state, while nuclei response to the new distribution of electrons is much slower (10^{-12} – 10^{-10} s), i.e. the electronic transition occurs within a stationary nuclear framework. We can illustrate this state with the help of an energy diagram where the electronic ground and excited states are depicted as vibrational potential energy curves as functions of the nuclear configuration represented by a Morse potential [4]. The electronic transition is then depicted as a vertical line from the ground to the excited state (Figure 1.1).

In classical terms, we can imagine nuclei in the initial electronic state as stationary and separated by the equilibrium bond length. After the excitation, the nuclei suddenly

experience the new force field created by the new distribution of electrons and they begin to oscillate (vibrate). What was once a stationary point with equilibrium bond length in the ground state now becomes a turning point with the same bond length in the excited state. When the transition is complete, the molecule starts to vibrate with energy matching the corresponding vibrational energy, i.e. intersection of a vertical line with electronic excited state potential energy curve (Figure 1.1A).

The quantum mechanical description echoes the classical one, but now the state of the nuclei is expressed by the wavefunction. The transition occurs from the ground vibrational state to the excited vibrational state with non-zero overlap between the two wavefunctions that characterise the two states (Figure 1.1B). The non-zero overlap can be represented by a nuclear overlap integral. The square of such integral is called the Franck-Condon factor, which is related to the probability of the simultaneous electronic and vibrational (vibronic) transition. In most cases, it is assumed that vibrational states are essentially the same in the ground and excited electronic states,
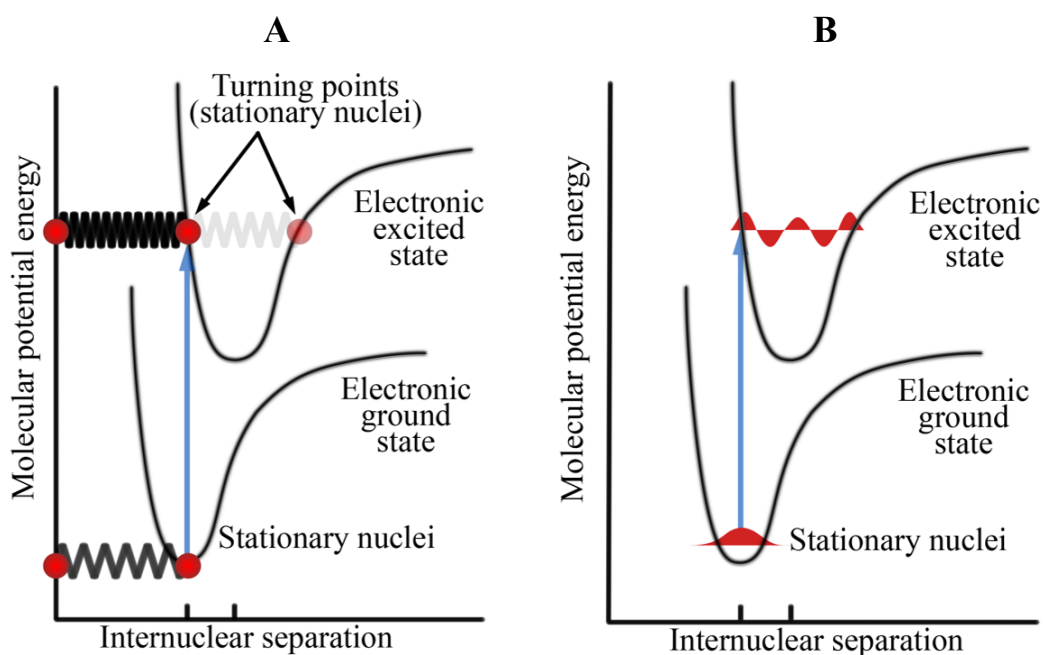
Figure 1.1: The Franck-Condon principle. **A)** Classical explanation of the Franck-Condon principle describes the bond between two nuclei (red circles) as a spring oscillator (zig zag black line). Upon excitation, i.e. transition to a state lying vertically above the stationary state (blue arrow), the electron distribution changes instantly and presses the nucleic spring oscillator, consequently turning the stationary state of the oscillator into the turning point state where the spring is pressed and therefore starts to oscillate. **B)** Quantum mechanical explanation of the Franck-Condon principle assumes that the vertical transition is to the vibrational state that most closely resembles the one in the ground state (blue arrow). In both cases (**A** and **B**), transitions to other vibrational levels occur, but with a lower probability (see Figure 1.2).

only the potential energy curves are displaced along the internuclear coordinate relatively to each other. This is caused mainly due to the more antibonding character of the excited state, where the equilibrium bond length increases. The interactions of a molecule with the surrounding solvent could also contribute to the displacement of the potential energy curves. This enhances the probability that more than one Franck-Condon factor is non-zero and multiple vibronic transition might be excited. Hence, the absorption spectrum of a molecule possesses vibrational structure of many energy lines (Figure 1.2).

The width of an absorption band of a molecule located in a particular environment depends on two effects: homogeneous and inhomogeneous broadening. Homogenous broadening depends on the time a molecule remains in the excited state. The shorter the lifetime of the excited state, the broader the width of the absorption line. Molecules in higher vibrational levels have more possible relaxation pathways, thus relax more rapidly than molecules in the lower levels [2]. Inhomogeneous broadening is caused by randomly changing interactions of a molecule with its surroundings and these effects also apply for the fluorescence spectra.
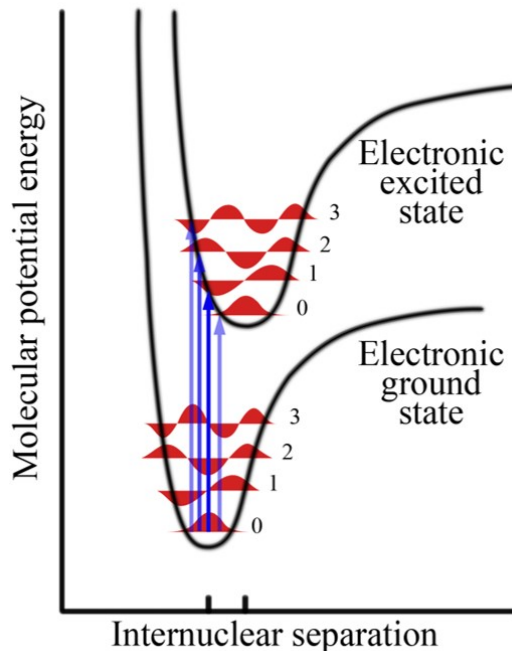
Figure 1.2: The Franck-Condon transitions to the multiple vibrational levels of the excited state, where the population of the vibrational levels is given by the Boltzmann law. At low temperatures, most molecules are in the lowest vibrational level (zero level) of the ground state, therefore the 0-0 is the lowest energy transition in the absorption spectra. In this picture, the strongest transition is the 0-1 (blue arrow), because of the greatest overlap between the two wavefunctions (red). The other transitions also occur but with lower intensity (fading blue arrows).

1.3 Fluorescence

1.3.1 Einstein coefficients

We have seen how light can excite molecules from the ground state to higher energetic states. Nevertheless, light can also stimulate emission from these excited states. It is a symmetrical but reversed process to the absorption described in the previous part. Albert Einstein in 1917 was the first to describe stimulated absorption and emission quantitatively [2]. He related the transition rate of stimulated absorption, i.e. the rate of change of the probability of finding the molecule in the excited state during a time interval, to the energy density of radiation (ρ) in the infinitesimal frequency range around the frequency of transition from the ground to the excited state (ν_{ge}):

$$W_{g \rightarrow e} = B\rho(\nu_{ge}) \tag{1.4}$$

where the constant B is the well-known Einstein coefficient, which can be directly related to the square of the transition dipole moment, i.e. intensity of the absorption (equation (1.1), (1.2) and (1.3)). When the ground state is populated with N molecules the total rate of absorption, i.e. the rate of change of the number of molecules excited during the time interval, is equal to the transition rate of a single molecule (equation (1.4)) multiplied by the number of molecules in the ground state.

Einstein described stimulated emission by the same equation as absorption (equation (1.4)), but this time the process starts in the excited state and ends in the ground state ($e \rightarrow g$). Einstein also recognized that at equilibrium, the rates of stimulated absorption and emission must be the same and consequently the coefficient B is the same for both processes. However, this requires the same population of the ground and excited states at thermal equilibrium which obviously contradicts the Boltzmann distribution. Therefore, Einstein suggested that there must be another way of radiative deexcitation independent of the incident light. He proposed that the excited state could undergo spontaneous emission characterised by the coefficient A, which he could directly relate to the coefficient B:

$$A_{eg} = \frac{8\pi h n^3 \nu_{eg}^3}{c^3} B_{eg} \tag{1.5}$$

where h is the Planck constant, c is the velocity of light in vacuum and n is the refractive index of the environment.

There are several important consequences of the equation (1.5). First, strong absorption inherently means strong emission since spontaneous emission is directly related to the intensity of the absorption. Coefficient A is also proportional to the cube of the transition frequency, therefore when raising the frequency of the incident light the spontaneous emission starts to dominate. For the visible region of light, all emission is essentially spontaneous. Finally, the main impact of the equation (1.5) is for the lasers operating at very high frequencies (e.g. X-rays). The construction of these lasers is very difficult mainly due to the cube of the transition frequency.

Spontaneous emission can be divided into fluorescence and phosphorescence, depending upon the character of the ground and excited states wavefunctions. At the beginning of the section 1.2, the description of nuclei had to be included into the wavefunction to explain correctly absorption by molecules. Now, the spin of an electron to obtain a complete picture of the emission has to be included too.

One can characterise fluorescence as the transition among ground and excited singlet states (S), i.e. symmetric spatial part and antisymmetric spin part of the singlet state wavefunction, with the zero-total angular momentum associated with electron spin. Whereas phosphorescence is the transition between an excited triplet (T) state to a ground singlet state, where triplet state wavefunction has antisymmetric spatial part and symmetric spin part, and the total spin is one. However, transitions between triplet and singlet states are formally forbidden because of the symmetry of the spatial parts of singlet and triplet states wavefunctions and symmetry of integration over the volume element result in a zero-transition dipole moment integral (equation (1.1)). Nevertheless, these forbidden transitions can be allowed under some conditions, e.g. by intersystem crossing from an excited singlet state. The spectrum of phosphorescence is located at longer wavelength than the fluorescence spectrum because the energy of the lowest excited triplet state (T_1) is lower than that of the singlet state (S_1). Besides, phosphorescence is a slow process and it is highly deactivated by other processes in a solution at room temperature.

Because the experimental part of this work (chapter 3) deals mainly with fluorescence, the main focus will be primarily on this phenomenon leaving phosphorescence aside in this theoretical introduction.

1.3.2 Radiative rate constant

The Einstein relationship between absorption and fluorescence is strictly valid only for systems that absorb and emit at a single frequency, but that is not the case for dissolved molecules possessing broad absorption and fluorescence spectra. Nevertheless, the radiative rate constant (k_r), a molecular version of Einstein A coefficient for spontaneous emission, can be correlated to the electronic transition dipole moment for emission from the excited to the ground state (μ_{eg}) [5, 6]. When this emission transition dipole moment is the same as the absorption one $(\mu_{ge} = \mu_{eg} = M)$, we can express the radiative rate constant as follows:

$$k_r = \alpha \langle v_f^{-3} \rangle^{-1} |M|^2 \tag{1.6}$$

where the factor $\langle v_f^{-3} \rangle^{-1}$ is defined as:

$$\langle v_f^{-3} \rangle^{-1} = \frac{\int F(v)dv}{\int v^{-3} F(v)dv} \tag{1.7}$$

where $F(v)$ represents the fluorescence spectrum and α is the constant dependent on the refractive index of the solvent. This correction for refractive index effects varies throughout the literature. α constant can be dependent either on square [5], cube [7] or even more complicated functions of the refractive index [8, 9]. This solvent dependent variety is caused by the fact, that various solvent effects are either omitted or counted in. From the experiments it seems that an appropriate correction for the refractive index of the solvent depends also on the solute molecules [8, 9].

Using the relationship between absorption spectrum and electronic transition dipole moment, equations (1.2) and (1.3) corrected for the refractive index effects, we can calculate the radiative rate constant from the absorption and fluorescence spectra [5], i.e. directly from the measurement quantities. As in the case of the oscillator strength, the radiative rate constant also connects theoretical and experimental quantities.

However, there is a more straightforward option for determining the radiative constant than using absorption and fluorescence spectra. The reciprocal of the radiative constant is the radiative lifetime (τ_r), sometimes called natural lifetime. Fluorescence lifetime is a crucial physical characteristic of the fluorophore and since fluorescence emission is a random process, fluorescence lifetime determines the average time spent by a molecule in the excited state [10].

1.3.3   Stokes shift, mirror image law and Kasha's rule

Fluorescence emission typically occurs from the lowest vibrational state of the first excited singlet state, although, higher vibrational states could be excited. This is caused by the ultrafast dissipation of the vibrational energy of the excited molecule before the emission can occur. This internal conversion, or vibrational relaxation, results in the shift of the fluorescence spectra to longer wavelength, compared to the absorption spectra, which is called the Stokes shift after G.G. Stokes who first observed this phenomenon. The shift can be explained by the relative displacement of the potential energy curves of the ground and excited states, as discussed in section 1.2. Besides, the interactions of fluorophore and local microenvironment of distinct polarity have profound effects on the electron distribution of the fluorophore, manifested as a decrease in the energy difference between ground and excited states. Thus, the Stokes shift reflects both intramolecular vibrational relaxation of the excited state and solvent relaxation in the vicinity of the molecule.

The similarity between the vibrational states of excited and ground states and the Born–Oppenheimer approximation result in similar Franck-Condon factors for corresponding transitions [2]. Consequently, fluorescence spectrum strongly resembles the mirror image of the absorption spectrum. The energies of allowed vibronic transitions in the absorption and emission spectra are symmetrically located on opposite sides of the 0–0 transition energy ($h\nu_{00}$) (Figure 1.3A). However, the vibrational structure is usually unresolved in the solution and emission spectra appears as a broad band (Figure 1.3B).

In most organic molecules, internal conversion from higher excited states to the lowest excited state occurs much more rapidly than fluorescence from the lowest excited singlet state (S_1) to the ground state (usually S_0). Internal conversion from S_1 to S_0 is also possible but is usually less efficient than conversion form higher energy levels to S_1 because of the much larger energy gap between S_1 and S_0. This generalization was introduced by Michael Kasha in 1950 and is known as Kasha`s rule. Although a few exceptions are known, like azulene or some corroles, where emission from the second lowest excited singlet state (S_2) occurs.
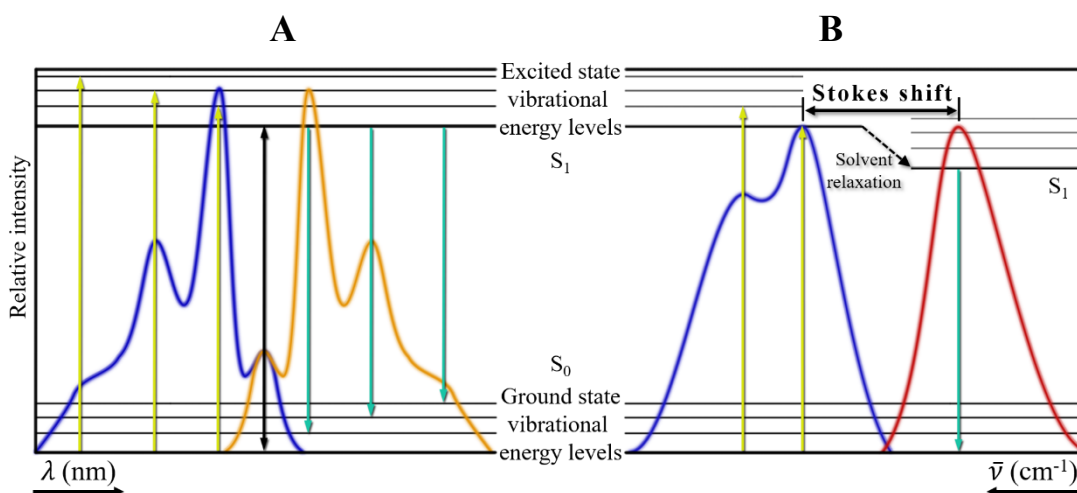
Figure 1.3: Mirror image law. **A)** The hypothetical absorption spectrum (blue) with the resolved vibrational structure (yellow arrows) is mirrored by the hypothetical emission spectrum (orange) with the similar vibrational structure (green arrows). **B)** Hypothetical absorption spectrum (blue) with resolved vibrational structure (yellow arrows) and hypothetical emission spectrum (red), where the vibrational structure of the absorption spectrum is not resolved in the emission spectrum (green arrow). The emission spectrum is shifted due to the solvent relaxation of the fluorophore, i.e. decrease in energy of the S_1 state. The resulting Stokes shift includes intramolecular vibrational relaxation of the excited state and solvent relaxation by the surroundings of the molecule. A rigorous comparison requires absorption and emission spectra in appropriate units, which are directly proportional to energy. Most often the wavenumber ($\bar{v}$) units expressed in reciprocal centimetres (cm^{-1}) are used. Wavenumbers are the reciprocal of the wavelength (λ), usually presented in nanometres (nm).

1.3.4 Non-radiative mechanisms and quantum yield

Fluorescence emission is not the only deexcitation mechanism of the S_1 state. There are non-radiative mechanisms competing with fluorescence emission. Since we are mainly interested in fluorescence, we can regard these mechanisms as fluorescence quenching, which is manifested as a decrease of fluorescence intensity of a sample and a decrease of the lifetime of the excited state. These mechanisms include internal conversion (k_{ic}), intersystem crossing (k_{isc}), resonant energy transfer (k_{ret}) and electron transfer (k_{et}). The rate constants for parallel processes are additive, thus the total rate constant (k_{tot}) and actual lifetime (τ) of the fluorescence can be expressed as follows:

$$\tau = \frac{1}{k_{tot}} = \frac{1}{k_r + k_{ic} + k_{isc} + k_{ret} + k_{et} + \cdots} = \frac{1}{k_r + k_{nr}} \qquad (1.8)$$

where k_{nr} is the non-radiative constant, sum of all non-radiative competing processes involved in the deactivation of the exited state, and

$$\tau_r = \frac{1}{k_r} \tag{1.9}$$

is the radiative lifetime.

Another important characteristic of the fluorophore is the quantum yield, which is the number of photons emitted relative to the number of absorbed photons [10]. For a homogenous sample that emits exclusively from the S_1 state, the quantum yield can be related to the radiative constant and lifetime:

$$\phi = \frac{k_r}{k_{tot}} = \frac{\tau}{\tau_r} \tag{1.10}$$

1.3.5   Fluorescence quenching

In this part, physical principles of some quenching mechanisms, that are important for this work, will be briefly described including resonance energy transfer, electron transfer, internal conversion and intersystem crossing. All these processes, that depopulates exited states of a molecule, can be schematically illustrated in a Jablonski diagram (Figure 1.4).

Although, quenching typically requires molecular contact between the fluorophore and quencher, the resonance energy transfer (RET) is at least one quenching mechanism that does not require contact of both molecules. RET is a consequence of a dipole-dipole interaction between transition dipole moments of donor and acceptor molecules. It can still be effective at distances of the order of 10 nm.

Electron transfer can be described as a coupling between molecular orbitals through a tunnelling, super-exchange or hopping process [11]. A special case of electron transfer is photon induced electron transfer (PET), where a charge transfer complex of the excited fluorophore and the quencher is formed. Depending on oxidation and reduction potentials, electron transfer from fluorophore, being the donor, to the quencher, being the acceptor, or vice versa can occur. This charge transfer complex usually relaxes to the ground state without emission, but in some cases exciplex emission is observed [10, 11].

During the internal conversion, the vibrational energy of the excited molecule is transferred into the vibrational modes of the molecules of the surrounding medium. The whole process depends on how closely the energy separation of the excited molecule matches those of surroundings. As a result, the lifetime of the excited state

of the molecule could be affected by varying the solvent. For example, water has rather high vibrational wavenumbers (directly proportional to energy): 1595, 3652, and 3756 cm^{-1} for its three normal modes, and its higher harmonics coincide with a range of typical electronic excitation. Hence, fluorescence lifetimes are often short in water [3].

Intersystem crossing is usually caused by spin-orbit coupling, which is the mutual interaction between magnetic dipoles associated with electron spin and orbital motion of an electron. During intersystem crossing from S_1 to T_1 the spin of the excited electron is flipped. To conserve total angular momentum of the system, the change of the spin must be compensated with a change in the angular momentum associated with another part of the system; it is typically orbital motions in organic molecules. Spin-orbit coupling is enhanced by the presence of heavy atoms in molecules or by collisional encounters between excited molecule and heavy atoms, e.g. Br, Pb or I. The thermally activated reversed process is possible provided the energy difference between S_1 and T_1 is small and the lifetime of T_1 is long enough. This is called delayed fluorescence, because emission has the same spectral distribution as normal fluorescence but with a much longer lifetime, which is prolonged due to the dwelling of the molecule in the triplet state before emitting from the singlet state.

Molecular contact between fluorophore and quencher can occur due to collisions (dynamic quenching) or due to complex formation (static quenching). Dynamic quenching is an additional rate process that depopulates the excited state, therefore the ratio of the quantum yield in the absence (ϕ_0) and the presence (ϕ) of the quencher will be equal to the ratio of corresponding lifetimes (τ_0) and (τ) as well as the ratio of fluorescence intensities (I_0) and (I). The dependence of dynamic quenching upon concentration is described by the famous Stern-Volmer plot:

$$\frac{\phi_0}{\phi} = \frac{\tau_0}{\tau} = \frac{I_0}{I} = 1 + k_q \tau [Q] \qquad (1.11)$$

where [Q] is the concentration of the quencher and k_q is the bimolecular quenching constant. This constant is related to the collisional frequency between freely diffusing molecules.

In static quenching a non-fluorescent complex is created between fluorophore and quencher. Therefore, static quenching does not decrease the lifetime, because only the fluorescent molecule can be observed, with its unquenched lifetime. However, a mixture of static and dynamic quenching can be observed in many systems, resulting in modified Stern-Volmer plot:
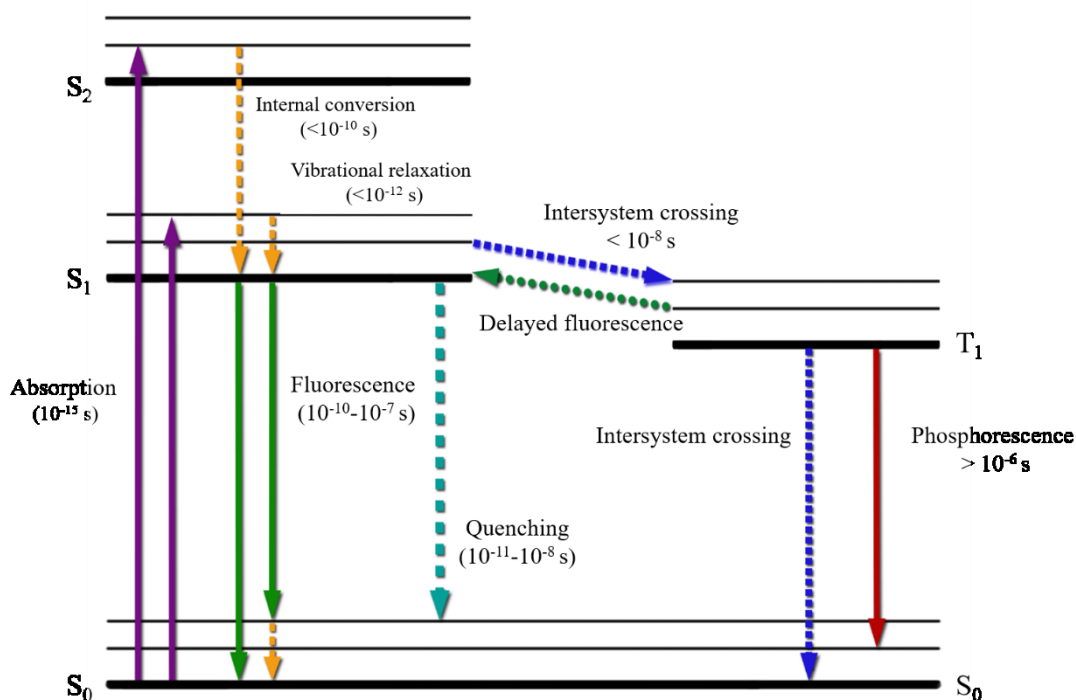
Figure 1.4: Jablonski diagram with important transitions, where some of them are shown along with their characteristic approximate times. Some of these times may vary throughout the literature.

$$\frac{I_0}{I} = (1 + k_q \tau [Q])(1 + K_s[Q])$$ (1.12)

where K_s is the stability constant of the non-emissive complex. Modified Stern-Volmer plot is no more first order but second order in [Q], i.e. it curves upward as the concentration of the quencher is increased. Although, the curvature may be apparent only at high concentrations of the quencher.

1.3.6   Fluorescence lifetime

Upon excitation of the sample a fraction of the fluorophores is excited to the higher energy states. These excited molecules then return to the ground state, either radiatively or non-radiatively, and the change in the number of excited molecules during time is directly related to the rate constants and number of excited molecules:

$$\frac{dN(t)}{dt} = (k_r + k_{nr})N(t)$$ (1.13)

16

Noting that the reciprocal of the sum of rate constants is the lifetime (section 1.3.2) and that fluorescence intensity $I(t)$ is proportional to the number of excited molecules, the solution of equation (1.13) can be expressed as:

$$I(t) = I_0 \exp\left(-\frac{t}{\tau}\right) \tag{1.14}$$

where I_0 is the intensity at time zero. However, monoexponential decays are quite unique in samples. More common is, for example, that more than one process is involved in depopulation of the excited state or fluorophores are exposed to surroundings with a broad range of different conditions. In that case, the intensity decay is multiexponential and the intensity can be assumed to decay as the sum of individual single exponential decays:

$$I(t) = \sum_{i=1}^{n} \alpha_i \exp\left(-\frac{t}{\tau_i}\right) \tag{1.15}$$

where τ_i are the decay times and α_i represents the amplitudes of components at time zero. The multiexponential model is one of the most powerful, because almost any intensity decay irrespective of its complexity, can be fit using equation (1.15). Nevertheless, the meaning of the parameters, τ_i and α_i, depends on the studied system and the data can also be consistent with other decay laws.

The problem with the interpretation of the parameters might be avoided by using the mean fluorescence lifetime:

$$\langle \tau \rangle = \frac{\int_0^\infty t I(t) dt}{\int_0^\infty I(t) dt} = \frac{\sum_i A_i \tau_i^2}{\sum_i A_i \tau_i} \tag{1.16}$$

This definition of the average lifetime preserves the expression for quantum yield in equation (1.10). Irrespective of the interpretation of the parameters, the fractional contribution of each decay time to the steady state intensity can be also determined:

$$f_i = \frac{A_i \tau_i}{\sum_i A_i \tau_i} \tag{1.17}$$

Then the mean lifetime can be defined as follows:

$$\langle \tau \rangle = \sum_i f_i \tau_i \tag{1.18}$$

In this part, it is assumed that the molecule is excited by an infinitely short pulse of light expressed as the Dirac δ function. However, the measured intensity decay is a convolution with the excitation pulse, which has finite time duration (see section 2.2).

2. Fluorescence spectroscopy

2.1 Absorption and emission measurements

There are many possibilities how to collect absorption and emission spectra, however, only typical instrumentation that are most common in many research labs are described here.

Absorption is usually measured as a decrease in the intensity of a light beam passing through a sample. The decrease in the intensity over the course of a small volume element is proportional, according to the well-known Beer-Lambert law, to the intensity of the light entering the sample, concentration of absorbers, and the length of the path through the sample. The light from a lamp passes through a monochromator, where the light is usually diffracted from the grating, and the sample can be scanned with defined narrow bands of wavelengths of light. The absorption spectrum is the wavelength distribution of the absorbance of a sample. Absorbance is the common logarithm of the ratio of incident to transmitted light intensity through the sample. Absorbance is dimensionless, however, sometimes it is reported in AU, "arbitrary units". Absorption spectrometers usually possess a reference spot, where a cuvette with solvent could be placed. Comparing the absorption of the sample and reference, e.g. pure solvent, one can simply obtain the absorption of the dissolved molecules alone.

Fluorescence emission, in contrast to absorption measurements, is usually collected at a right angle to the incident beam. Fluorometers typically possess two monochromators to collect emission and excitation spectra. The emission spectrum is the wavelength distribution of the emission measured at a single, constant, excitation wavelength. Conversely, an excitation spectrum is the dependence of emission intensity, measured at a single emission wavelength, upon scanning the excitation wavelength. Such spectra can be presented on either a wavelength scale (λ) with typical unit in nanometres (nm), or a wavenumber scale ($\bar{v}$) with typical unit in reciprocal centimetres (cm^{-1}). Even though the wavenumber scale is linear in energy, most commercial instrumentations yield spectra in wavelength. Unlike absorption spectra, emission spectra must be corrected for factors influencing the shape and intensity of the spectra, e.g. the lamp intensity profile, different wavelength sensitivity

18

of the detector, or the influence of monochromator components in the case of polarization measurements.

2.1.1   Instrumentation

Stationary emission spectra were obtained on Fluorolog-3 spectrofluorometer (model FL3-11; HORIBA Jobin Yvon) equipped with a 450W Xenon-arc lamp. Emission spectra used for calculation of time dependent Stokes shift were measured at magic angle polarization.

Absorption spectra were measured on Shimadzu UV-2600 with 50 W halogen lamp and deuterium lamp.

2.2 Time correlated single photon counting

The method was first conceived in nuclear physics and then for a long time primarily used to analyse the light emitted as fluorescence during the relaxation of molecules from an optically excited state to a lower energy state [12]. This process can be simply characterized by the fluorescence lifetime, i.e. the average time the molecules of interest spend in excited state (section 1.3.6). The main goal of time correlated single photon counting (TCSPC) is still measurement of fluorescence decay curves, nevertheless, modifications and extensions of the early designs allow for the recovery of much more information from the detected photons and enable entirely new applications, e.g. fluorescence lifetime imaging (FLIM) [13]. In this work, we used old fashioned TCSPC instrument designed mainly to investigate fluorescence lifetimes.

When an excitation pulse excites fluorophores within the sample, numerous photons are emitted during their deactivation. The time course of this emission is called decay curve. One would like to record this in a single shot, but such a weak signal cannot be detected with sufficient signal-to-noise ratio. The detection method of choice is single photon counting. TCSPC is based on repetitive, precisely timed registration of single photons. This is equivalent to sampling of the decay curve, photon by photon. The reference for the timing is the corresponding excitation pulse and the number of photons detected after distinct delay times is stored in a form of a histogram. Provided

the probability of registering more than one fluorescence photon per excitation pulse is negligibly low (in practice this is assured by keeping the photon detection rate below 2% of the excitation pulse repetition rate), the histogram of photon arrival times represents the fluorescence decay curve. The precondition of single photon counting probability must be met, otherwise the histogram would be biased towards shorter delay times. The reason is the unavoidable dead-time of the electronics. After an excitation pulse, only the first incoming photon would be timed, never the second, later arriving photon in that pulse period. This effect is called classic pile-up in TCSPC.

The main issue is to measure the arrival time of the photon precisely. In TCSPC, typical detectors are photomultiplier tubes (PMT) or microchannel plate (MCP) detectors. The amplitude of their electrical output pulses as a response to a single photon impact may vary, obeying a broad distribution. The constant-fraction-discriminator (CFD) is used to extract precise timing information from such variable amplitude pulses. A CFD divides the electrical signal into two copies. One pulse is inverted and its amplitude added to the other pulse shifted by a constant time delay. The result is an output waveform that intersects the time axis, i.e. has zero amplitude and changes polarity, at a well-defined moment, when the original signal pulse reaches a certain constant fraction of the original peak amplitude. The moment of zero crossing is therefore independent of the amplitude of the original pulse.

The signal pulse from the excitation source (start pulse) is passed to the time-to-amplitude converter (TAC), which generates a voltage ramp, i.e. voltage linearly increasing with time on the nanosecond timescale. A second pulse from the detected photon emitted from the sample, whose arrival time is accurately determined using a CFD, sends a signal to stop the voltage ramp. The TAC now contains a voltage proportional to the time delay between the excitation and emission signals. The signal is then amplified and if it is within the defined range of voltages, the voltage is turned into a digital value with an analog-to-digital converter (ADC) and stored as a single event in the histogram. The defined range of voltages should minimize false reading. As a single-photon-sensitive detector, in addition to those already mentioned, a single photon avalanche diode (SPAD) or hybrid PMT can be used (Figure 2.1).

As mentioned earlier, the determination of lifetimes in this work was performed in a classical TCSPC setup and therefore, the reverse start-stop mode was used for data acquisition. The process is the same as described above except that the emission pulse is used to start the TAC and the excitation pulse is used to stop the TAC. By reversing

the start and stop signals in the time measurement, the conversion rates are only as high as the actual photon rates generated by the fluorescent sample. This procedure is used mainly because the old fashioned TAC cannot handle the typically high repetition rates of the used excitation lasers [13]. In modern TCSPC this problem is solved with time-to-digital converters (TDCs), which are high speed digital circuits. There are many variants of TDC implementations, nevertheless, the simplest solution for a TDC is a digital counter running at the speed of a fast crystal locked clock. Suitable counter implementations in fast semiconductor technologies such as SiGe can in principle be operated at clock rates as high as 40 GHz, thus providing time resolutions of 25 ps [12].

2.2.1   TCSPC instrumentation

Time-resolved fluorescence decays were measured using the TCSPC technique in an IBH 5000 U SPC instrument equipped with a cooled Hamamatsu R3809U-50 microchannel plate photomultiplier with 30 ps time resolution. The time setting for the results presented in the chapter 3 was ranging from 7 ps to 14 ps per channel. The bandwidths for both the excitation and emission monochromators range from 32 nm to 8 nm. In order to eliminate scattered light, appropriate cut-off filters were used. In the case of first three studies (sections 3.1, 3.2 and 3.3), samples were excited at 375 nm with an IBH NanoLED-11 diode laser (70 ps fwhm) with a repetition frequency of 1 MHz. In the case of corroles study (sections 3.4), samples were excited at 405 nm with a Picoquant LDH-D-C-405 diode laser (50 ps fwhm) with a repetition frequency of 2.5 MHz. The detected signal was kept below 2% of the light source repetition rate to avoid shortening of the recorded lifetime due to the pile-up effect. Fluorescence decays were fitted, using the iterative reconvolution procedure with IBH DAS6 and PicoQuant FluoFit® software, to a multiexponential function (equation (1.15)) convoluted with the instrument-response-function IRF ("prompt"), yielding sets of lifetimes τ_i and corresponding amplitudes A_i:

$$I(t) = \sum_i A_i \exp\left(-\frac{t}{\tau_i}\right) \otimes IRF \qquad (2.1)$$

There is a fundamental resolution limit to exponential analysis, determined by the signal-to-noise ratio (SNR) in the input decays. The maximum resolution that can be reached in experimental setups, i.e. τ_{i+1}/τ_i, is about 1.6 to 1.8, provided SNR varies

from 10^3 to 10^4 [14]. In our case, the SNR value usually exceed 10^3 and investigated lifetimes usually differs more than a factor of 2.
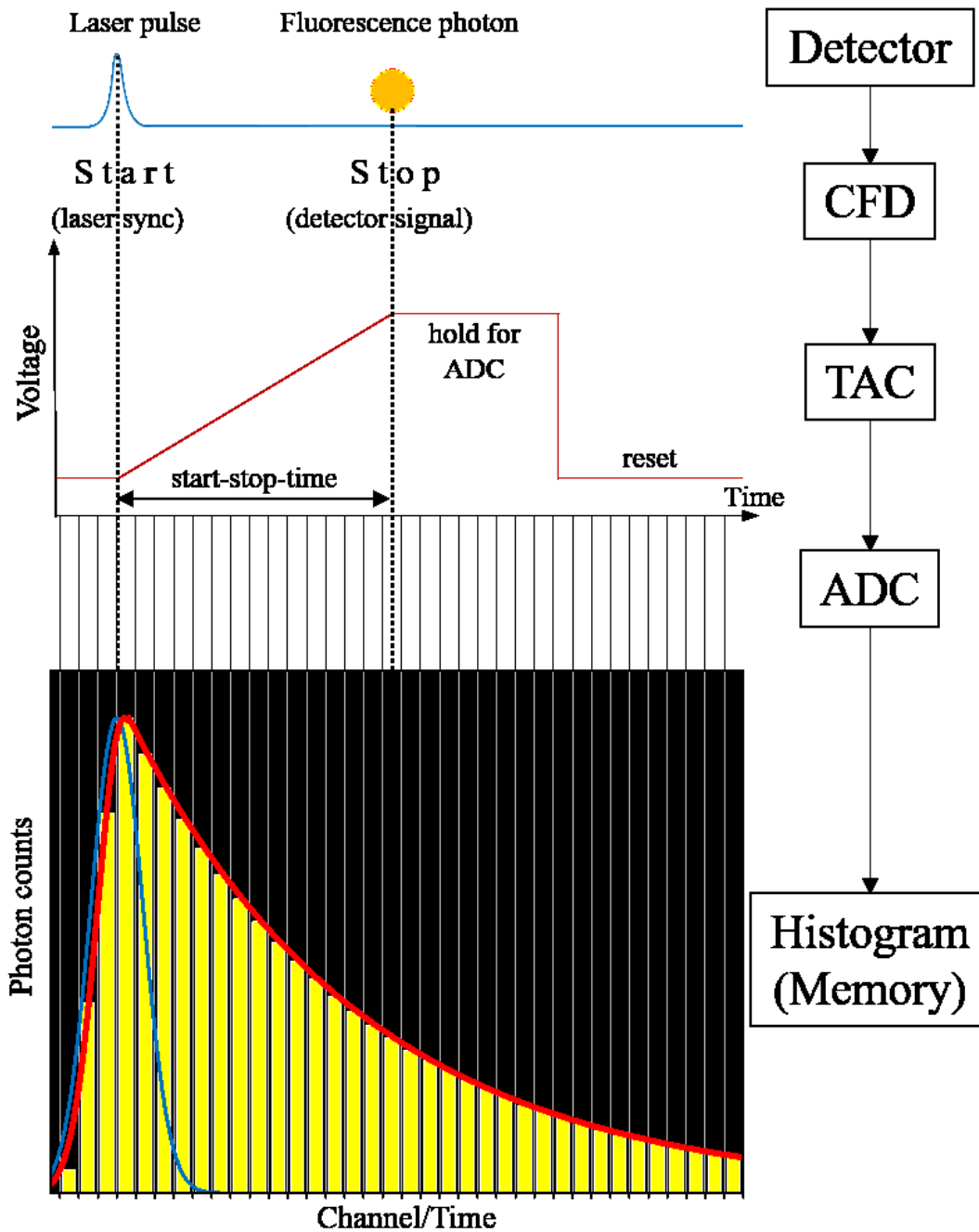
Figure 2.1: TCSPC principles and scheme of operation. In the direct start-stop mode, the laser pulse is precisely determined by CFD and the voltage ramp is started within TAC. When a fluorescence photon is detected and after precise determination of the arrival time, the voltage ramp is stopped. The voltage obtained from the TAC is then guided to the ADC, which provides the digital timing value. This value is then sent to the memory (histogram memory cell). After the measurement, the output is a histogram of number of photons stored within a certain time channel (yellow columns at the bottom picture). The blue curve at the bottom picture is the instrument-response-function (IRF) and the broadening of its full-width-at-half-maximum (FWHM) reflects the contribution introduced by all components of TCSPC to the total IRF.

22

2.3 Fluorescence up-conversion

The time resolution of TCSPC is assumed, under favourable conditions, as 1/10 of the IRF, where IRF is typically in tenth of picoseconds [12]. Better time resolution, i.e. femtoseconds, is provided by optical methods that bypass the limited time resolution of the detection electronics, and rely on the fs pulse widths available with modern lasers. These methods manage to cut a short time slice of the sample emission, which can be measured with relatively slow photodetectors. This can be imagined as optically controlled gate for the sample emission.

The basic idea is to generate two short pulses, pump and gate (probe), at desired wavelengths and vary the delay between them. The pump pulses, usually with double frequency than gate pulses $(2v)$, excite the sample and the fluorescence signal is passed through a non-linear crystal (NL). The gate pulses, with frequency (v), are passed to the delay line and then directed to the same NL crystal. Both the gate and the emission pulses are focused at the NL crystal, which is the key component in providing femtosecond time resolution. The crystal mixes the gate fundamental frequency, v, and the emission frequency, v_{em}, to generate the sum frequency, $v_{sum} = v + v_{em}$. The light intensity at v_{sum} is measured by the detection system. Because the frequency of the detected signal is shifted up by value v relative to the emission frequency v_{em}, the method is called up-conversion (Figure 2.2A).

The signal at the sum frequency is generated only when both the gate pulse and the emission signal hit the crystal, i.e. only during the time interval when the gate pulse and emission overlap each other. The phase matching condition for the efficient sum frequency generation requires certain orientation of the NL crystal. This is achieved by cutting the crystal at certain crystallographic orientation, and by angular fine tuning of the crystal, to satisfy the phase matching condition for the gate and emission wavelengths. Different non-linear crystals can be used to generate sum frequency, e.g. LiIO$_3$, KDP and BBO.

The light intensity at sum frequency, v_{sum}, is proportional to the product of the instant intensities of the gate and emission. Since the gate pulse intensity is constant, we can probe the emission intensity at different delay times (Δt) by scanning the delay line. The result is the time profile of the emission with resolution determined by the width of the gate pulse (Figure 2.2B).
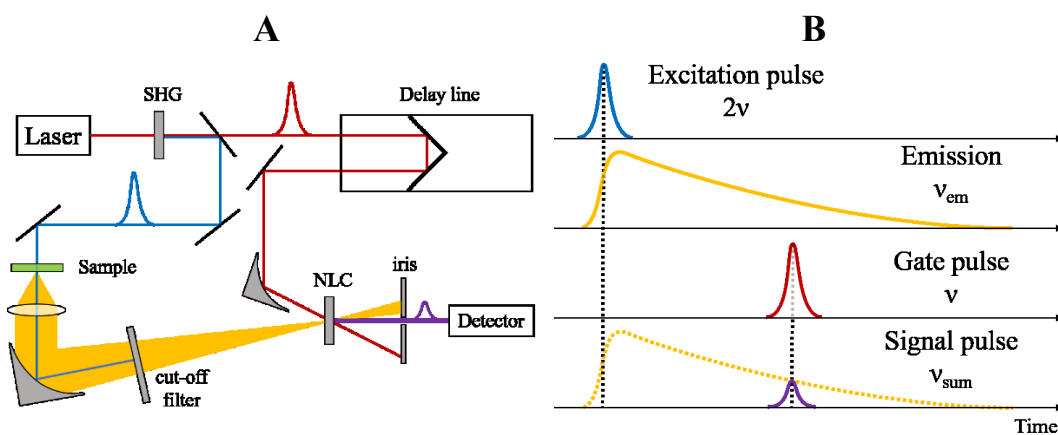
Figure 2.2: Up-conversion schemes. **A)** Simplified scheme of the fluorescence up-conversion instrumentation. SHG is second harmonic generator and NLC is non-linear crystal. **B)** Scheme of the frequency mixing of the emission and gate signal.

2.3.1   Up-conversion instrumentation

Fs-resolved fluorescence was measured using a setup of fluorescence up-conversion (FlUC) at École polytechnique fédérale de Lausanne (EPFL), where the broadband emission detection is implemented to the up-conversion setup with a time resolution around 100 fs in the visible range [15]. Pulses at 400 nm were obtained by frequency doubling 80 fs pulses at 800 nm provided by a Coherent Rega Ti: Sapphire regenerative amplifier operating at 150 kHz repetition rate. The excitation light was focused onto a 0.2 or 0.1 mm thick quartz flow-cell, where the sample solution flowed continuously. The light emitted by the sample was collected by a parabolic mirror in forward-scattering geometry, and directed to a second mirror that focuses it onto a 0.25 mm thick β-barium borate (BBO) crystal. The luminescence was then upconverted by mixing with the 800 nm gate pulse. The up-converted signal was spatially filtered and detected with a spectrograph and a liquid nitrogen cooled CCD (charge-coupled device) camera. The kinetics of the emitted signal were measured by delaying the gate beam with respect to the onset of the fluorescence, while keeping the BBO crystal at a given angle. Polychromatic detection was obtained by rotating the BBO crystal via a computer-controlled motor, during the accumulation time of the CCD camera, to phase-match a wide spectral region at each time delay. A 140 fs IRF was estimated by measuring the water Raman signal, allowing us to safely determine lifetimes approx. 3-times shorter using deconvolution. Kinetics were analysed by singular value decomposition (SVD) and global fitting [16].

2.4 Fluorescence solvent relaxation technique

Solvent polarity and the local environment have profound effects on the spectral properties of the emission from fluorophores. The effects of solvent polarity contribute to the Stokes shift, as mentioned in section 1.3.3. However, environmental effects are complex and even solvent polarity cannot be described using a single theory. The Lippert-Mataga equation partially explains the effect of solvent polarity, but does not account for other effects such as hydrogen bonding to the fluorophore or internal charge transfer that depends on solvent polarity [10]. The equation describes general solvent effects where the fluorophore is considered to be a dipole in a continuous medium of uniform dielectric constant. In this way, we can relate the Stokes shift (Figure 1.3B), i.e. the difference between the ground and excited state energies described by the absorption and emission maxima $\overline{v_A}$ and $\overline{v_F}$ in wavenumbers, to the refractive index and dielectric constant of the solvent:

$$\overline{v_F} - \overline{v_A} \propto (\mu_E - \mu_G)^2 \left(\frac{\varepsilon - 1}{2\varepsilon + 1} - \frac{n^2 - 1}{2n^2 + 1} \right) \qquad (2.2)$$

where μ_E and μ_G are the permanent dipole moments of the excited and ground state respectively. The square of the refractive index (n) is a high frequency component of the dielectric constant, which characterises the immediate response of the electrons of the solvent molecule to the external electric field. On the contrary, the dielectric constant (ε) is a static property, which depends on both electronic and molecular motions. Therefore, the term in parentheses in equation (2.2) is called orientation polarizability and reflects only the orientation of the solvent molecules around fluorophore. The polarizability can be expressed in various versions depending on theoretical assumptions, however, the physical meaning remains unchanged [17, 18].

The Lippert-Mataga equation is only an approximation and does not include, for example, effects of electronic polarizability. The solvent can be polarized electronically by both the permanent and the transition dipoles of the fluorophore and reciprocally, the fluorophore experiences a similar inductive polarization by fields from the solvent. As a result, an increase in refractive index of the solvent allows both the ground and excited states of the fluorophore to be instantaneously stabilized by movements of electrons within the solvent molecules. This electron redistribution results in a decrease in the energy difference between the ground and excited states, i.e. the energy of the absorption band is decreased. For this reason, most fluorophores

display a red shift of the absorption spectrum in solvents relative to the gas phase. An increase in dielectric constant will also result in stabilization of the ground and excited states. However, the energy decrease of the excited state due to the dielectric constant occurs only after reorientation of the solvent dipoles [2, 10]. The detailed mathematical description of the solvent-solute relationship depends on the set of assumptions that each particular dielectric solvation theory formulates.

However, when the fluorophore is immersed in one particular solution, its absorption spectra are less sensitive to the solvent polarity because the molecule is exposed to the same local environment in the ground and excited states. In contrast, the emitting fluorophore is exposed to the environment, that contains solvent molecules orienting around the newly created or changed dipole moment of the excited state, thus continuously changing the energy of this state. The characteristics of this dynamic process can be revealed by the time-resolved measurements.

2.4.1   Time dependent fluorescence shift

Time dependent fluorescence shift (TDFS) experiments are based on an ultrafast change in the dipole moment of the fluorescent dye caused by the electronic excitation. Consequently, dipole moments of the solvent molecules are forced to adapt to the new situation and start to reorient in order to reach an energetically favourable state. This dynamic process starting from the initial non-equilibrium Franck-Condon state (FC), i.e. the excited molecule is in the lowest vibrational state and solvent molecules remain as they were before excitation, and gradually proceeding towards the fully relaxed excited state, is called solvent relaxation (SR) [19, 20]. The decreasing energy of the system is manifested by a continuous red-shift of the recorded time-resolved emission spectra (TRES). The higher the polarity of the solvent, the lower the energy of the relaxed state and the larger the red-shift of the emission spectrum (Figure 2.3).

TRES contain complex information about microenvironment in the vicinity of the fluorescent probe. As it was shown for a large variety of neat liquids, following the temporal changes in the frequency of TRES maximum $v(t)$ allows micropolarity and microviscosity of the dye microenvironment to be assessed [19]. The micropolarity can be characterized by the total amount of the TDFS which is defined as:

$$\Delta v = v(0) - v(\infty) \tag{2.3}$$

26

This difference is attributed to the difference between the initial Frank-Condon $(v(0))$ and the fully relaxed state $(v(\infty))$ energies. It was also shown, that Δv is directly proportional to the polarity function of the solvent shell around the fluorescent probe [21]. For example, proteins are usually dissolved in water, thus the total amount of the TDFS can reflect the hydration in the vicinity of the fluorescence probe covalently bound to the protein.

The second parameter yielded from TRES, which reflects microviscosity (mobility) of the microenvironment of the fluorescent dye, is quantified by normalizing the temporal dependence of TRES maxima $v(t)$ to the total amount of the shift:

$$S(t) = \frac{v(t) - v(\infty)}{v(0) - v(\infty)} = \frac{v(t) - v(\infty)}{\Delta v} \qquad (2.4)$$

The $S(t)$ function, also known as spectral response function, reflects the rearrangement kinetics of the immediate vicinity of the dye. Moreover, nonequilibrium spectral response function $S(t)$ can be related to the equilibrium fluctuations of the difference in solvation energies $(\delta \Delta E)$ between the ground (S_0) and excited (usually S_1) electronic
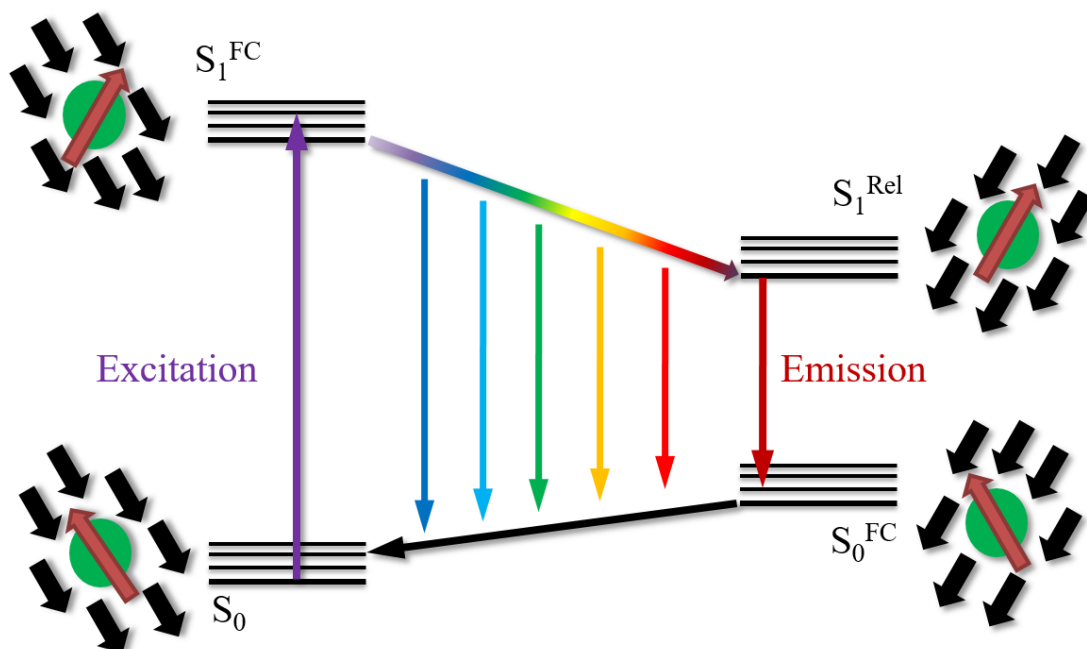
Figure 2.3: The principle of solvent relaxation manifested by the TDFS. The result of excitation (purple arrow) is the non-equilibrium Franck-Condon state (S_1^{FC}), where the dipole moment of the fluorophore is changed (green circle with the red arrow) compared to the ground state S_0. The subsequent relaxation of the solvent in the vicinity of the fluorophore (black arrows), i.e. interaction of the solvent dipoles with the electric field of the fluorophore dipole, decreases energy of the excited state (S_1^{Rel}) which is manifested by the red-shift of the fluorescence emission during the time of the process (blue to red arrows).

states of the unperturbed dye, supposing the perturbation caused by the electronic transition is within reasonable limits, e.g. fluorophore does not exhibit unique excited state photochemical properties like photoinduced proton transfer or large conformational changes [22, 23]:

$$S(t) \cong \frac{\langle \delta \Delta E(0) \delta \Delta E(t) \rangle}{\langle \delta \Delta E^2 \rangle} \qquad (2.5)$$

where $\delta \Delta E(t) = \Delta E(t) - \langle \Delta E \rangle$. $\Delta E(t)$ represents solvation energy gap between the ground and excited states of the fluorophore as a function of time and $\langle \Delta E \rangle$ represents the average value of the difference in these two energies.

The relationship (2.5) implies that the relaxation of the excited dye-solvent system to the equilibrium state reflects the very same dynamics as the relaxation of naturally occurring fluctuations in the unperturbed dye-solvent system at equilibrium. This assumption is the core of the general principle called the fluctuation-dissipation theorem. The response of a system to the external perturbation is characterised as a linear response relaxation from prepared non-equilibrium state. It is quite common that the linear response relaxation takes the form of one or more exponential decays, thus $S(t)$ can be fitted to one or, if necessary, to more exponentials too:

$$S(t) = \sum_i B_i e^{-t/\tau_i^{TC}} \qquad (2.6)$$

where τ_i^{TC} are relaxation time constants. The second possibility is numerical integration of $S(t)$ to give a simple measure of the TDFS kinetics:

$$\tau_R = \int_0^\infty S(t) dt \qquad (2.7)$$

where average relaxation time τ_R was shown to be closely proportional to the viscosity of the solvent, spanning time scales from hundreds of femtoseconds to seconds [24, 25].

Although, $S(t)$ can be connected to the solvent fluctuation within the linear response framework, there is no guarantee that linear response theory is valid for given system [23, 26]. However, this connection appears to be justified for most of the experimentally studied systems [22, 27]. Besides, the ability to study relaxation of the naturally occurring fluctuations, which reflects the dynamics of the system, is one of the key motivations for using this method [28, 29].

The $S(t)$ function can be determined by "spectral reconstruction" [24], which requires a minimum of a priori assumptions and has been used in this work. TRES

points $S(\lambda, t)$ are calculated by a normalization of the fitted fluorescence decays $I(\lambda, t)$ to the steady state spectrum $S_0(\lambda)$ at a given time:

$$S(\lambda, t) = \frac{I(\lambda, t)S_0(\lambda)}{\int_0^\infty I(\lambda, t)dt} \tag{2.8}$$

The normalization guaranties that the fluorescence decay functions can be used to calculate fluorescence intensity at any wavelength and time, thus correct calculation of the TRES points. These points should be then transformed into wavenumber domain and fitted. The log-normal line shape function [30], which gives a realistic picture of broad, asymmetric electronic emission bands, appears to be the right choice for the fit of the TRES [20, 21]:

$$F(v, t) = h \begin{cases} \exp\left[-ln2\left\{\frac{\ln(1 + \alpha)}{\gamma}\right\}^2\right] : \alpha > -1 \\ 0 \qquad\qquad\qquad\qquad\quad : \alpha \leq -1 \end{cases} \tag{2.9}$$

where

$$\alpha \equiv 2\gamma(v - v_p)/\Delta \tag{2.10}$$

The time evolution of the fitted parameters, i.e. the peak height (h), the peak position (v_p), the asymmetry parameter (γ), and the width parameter (Δ), which are obtained via a nonlinear least-squares fitting of the TRES points, fully describes the rates of relaxation and the nature of the relaxation process. If the log-normal model fails to fit the data, excited state processes other than pure continuous solvent relaxation may be considered [20]. The evaluation of TRES is mainly limited by the temporal resolution of the lifetime measurements (section 2.2), therefore the first several spectra within this temporal resolution are unreliable. Figure 2.4 shows schematically calculation of TRES and TDFS from measured decays.

The temporal behaviour of the full width at half maximum (FWHM, (Δ)) of the TRES provides rough but useful information on the extent of the observed solvent relaxation. It has been shown that in homogeneous systems of low molar mass molecules, the FWHM decays monotonically. However, in spatially inhomogeneous systems, e.g. phospholipid bilayers [31] or supercooled liquids [32], where the microenviroments of the fluorophores differ, the time evolution of FWHM passes a distinct maximum [20, 33]. The broadening of the FWHM at intermediate times is theoretically explained by the fact that each solvation shell of each particular fluorophore differs and responds at a different relaxation rate to the change in the local
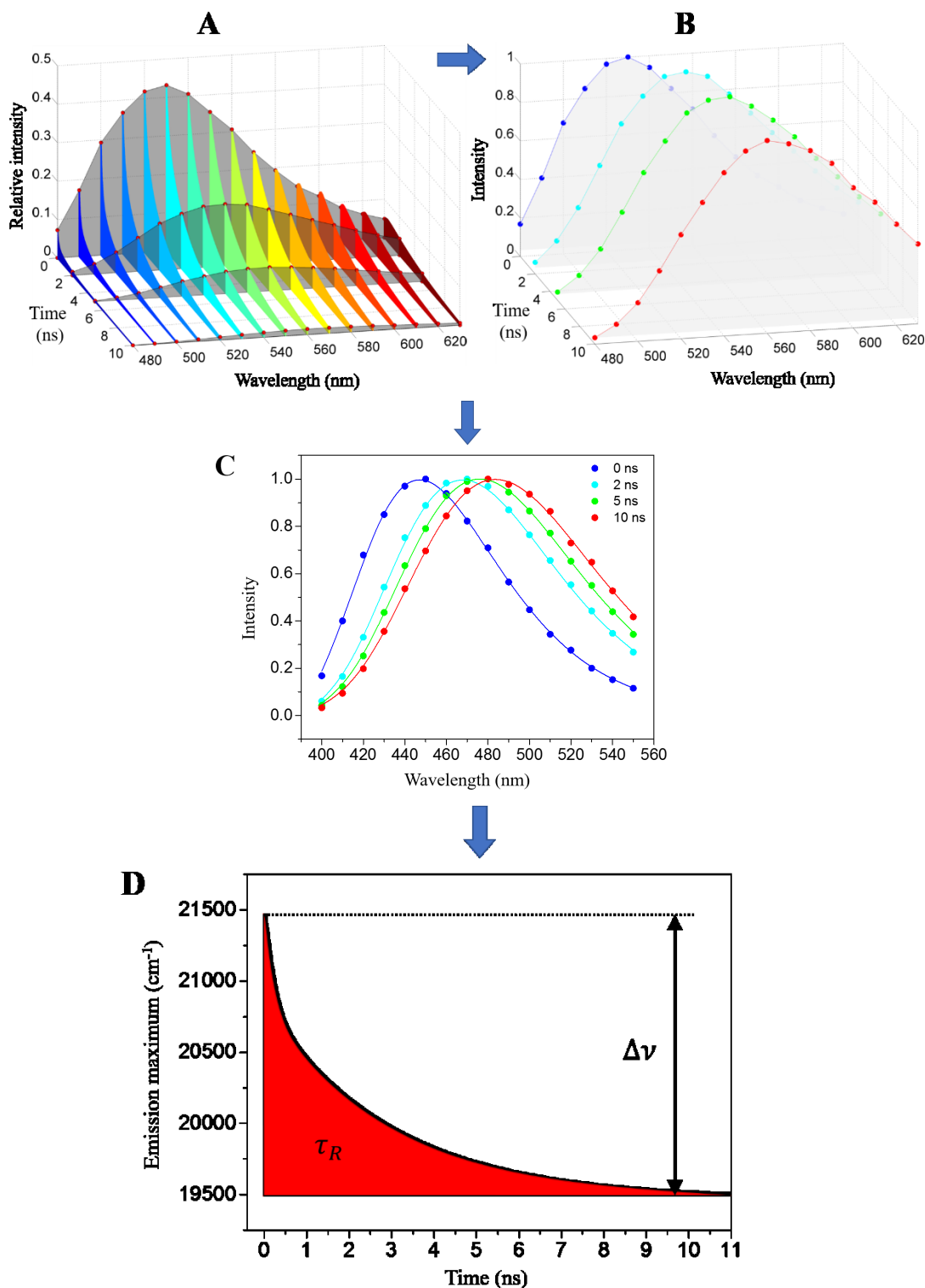
Figure 2.4: Reconstruction of the TDFS from the measured fluorescence lifetime decays. After the normalization of the decays according to the equation (2.8) **(A)**, the TRES can be calculated at the desired wavelength. The normalization of the TRES is made just for the visual reasons here **(B)**. TRES points are fitted with the log-normal distribution (equations (2.9) and (2.10)) in order to obtain the temporal dependency of the position of emission maxima ($\Delta \nu$) **(C)**. $\Delta \nu$ is directly obtained from the subtraction of the first (first reliable spectrum concerning the time resolution of the instrumentation) and the last spectrum. τ_R is represented by the area under the normalized TDFS curve (equation (2.7)) **(D)**.

electric field invoked by the fluorophore excitation. The extent of FWHM broadening is directly related to the heterogeneity of the dye microenvironment [34].

One can take advantage of this effect when investigating whether the entire response or merely part of it was captured within the time-window of the experiment. When only a decrease in the FWHM is observed, the early part of the relaxation process is possibly beyond the time resolution of the equipment. On the other hand, when only an increase is detected, the process is fairly slow under given conditions and the lifetime of the used fluorophore is not long enough to completely monitor the relaxation [35].

Concerning this work, TRES of the labelled proteins and DNA showed only a decrease of the temporal evolution of FWHM. Accordingly, we needed to employ another method to obtain the total TDFS.

2.4.2   Time-zero estimation

The estimation of the position of the so called time-zero spectrum $\nu(0)$ is essential for the calculation of the total TDFS. This spectrum is a hypothetical fluorescence emission spectrum of the molecules that are in the Frank-Condon state. The estimation of this spectrum based on the extrapolation of the measured TRES back to t=0, has been shown to be strongly affected by the time resolution of the instrumentation and often leads to significant errors in calculated TDFS parameters. The procedure for estimating the time-zero emission spectrum used in this work was described by Fee and Maroncelli [36] and it is based on the model of electronic spectra of solvatochromic probes described in detail in Fee et al. [37]. It has already been performed with success for selected coumarines [36, 38], Patman and Prodan [39], amino-cyano-stilbenes [40] and 4-aminophthalimide (4AP) [41]. In the case of 4AP, Sajadi et al. showed that the time-zero estimation agrees satisfactorily with the prediction of the continuum theory but also fits well with the experimental observations from ultrafast measurement.

The time-zero estimation needs only the absorption spectrum of the fluorescent dye in the polar system of interest (A_p), absorption (A_{ref}) and emission (F_{ref}) spectra measured in a non-polar reference solvent, thus making this method independent of the experimental temporal resolution. The spectra measured in a non-polar reference

solvent are used to simulate spectral properties of the Frank–Condon state. The time-zero estimation assumes that the solvent environment affects the absorption spectra of an individual molecule only by an overall frequency shift (δ) and that the site distribution function $p(\delta)$ has the Gaussian profile:

$$p(\delta) = \frac{1}{\sqrt{2\pi\sigma^2}} \exp\left(\frac{-(\delta - \delta_0)}{2\sigma^2}\right) \qquad (2.11)$$

where δ is basically the measure of the displacement of the ground and excited state potential energy curves (solvent coordinate) for every molecule in the ensemble (section 1.2 and 1.3.3), δ_0 is the average shift induced by the polar solvent and σ is the variance. Such distribution is usually assumed and observed to be appropriate in models of polar solvation [37].

One can consider that the line-shape function $g(v)$ describes the absorption spectra of all solute molecules including the underlying vibronic structure and any homogeneous broadening of the absorption spectrum:

$$g(v) \propto \frac{A_{ref}(v)}{v} \qquad (2.12)$$

Bearing these assumptions in mind, we can just simply find the site distribution function $p(\delta)$ by fitting its convolution with $g(v)$ to the measured absorption spectrum A_p in the polar solvent:

$$A_p(v) \propto v \int g(v - \delta)p(\delta)d\delta \qquad (2.13)$$

Once the $p(\delta)$ distribution is found, the time-zero emission spectrum, observed immediately after monochromatic excitation (v_{ex}), can be computed from the convolution with absorption $g(v)$ and emission $f(v)$ line-shape functions:

$$F_p(v, t = 0, v_{ex}) \propto v^3 v_{ex} \int g(v_{ex} - \delta)p(\delta)f(v - \delta)k_{rad}(\delta)d\delta \qquad (2.14)$$

where:

$$f(v) \propto \frac{F_{ref}(v)}{v^3} \qquad (2.15)$$

and $k_{rad}(\delta)$ is the radiative rate constant. Figure 2.5 illustrates the time zero estimation method.

The radiative rate k_{rad} depends on the $\langle v_f^{-3} \rangle^{-1}$ (equations (1.6) and (1.7)). Maroncelli et al. showed that $\langle v_f^{-3} \rangle^{-1}$ for typical solvatochromic probes varies with δ (solvent coordinate) and that this variation causes an observable time dependent Stokes
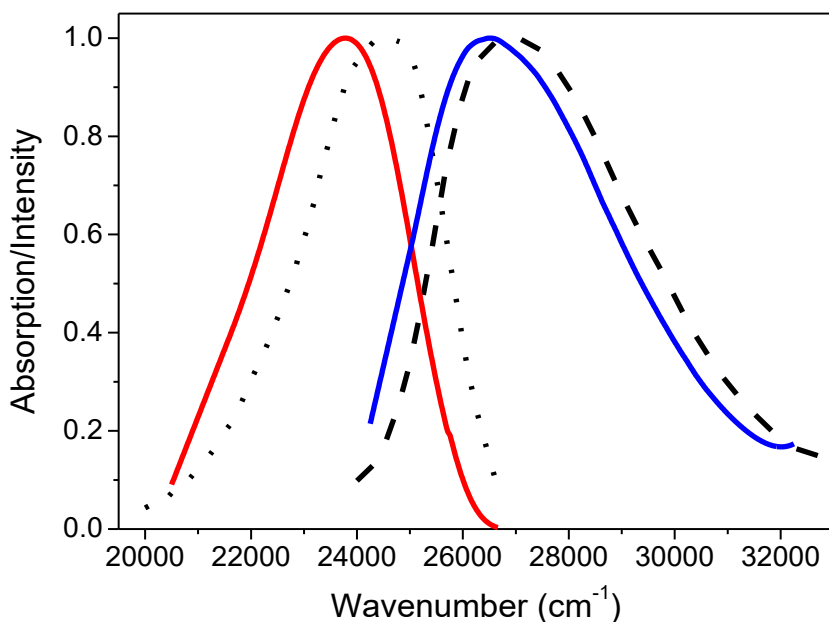
Figure 2.5: The estimated time-zero emission spectrum for Badan bound to the active site of the c382s mutant (red line, see section 3.3) and the spectra used for its calculation. Absorption (dashed line) and emission (dotted line) spectra were measured in cyclohexane to obtain line-shape functions $g(\nu)$ and $f(\nu)$, respectively. Absorption spectrum of Badan bound to the active site of the c382s mutant (blue line) were used for calculating Gaussian site distribution function $p(\delta)$.

shift of these probes in frozen solvents [7, 37]. However, at room temperatures this effect is negligible, therefore it is not mentioned in the previous section. Moreover, the effect of k_{rad} on the time zero estimation is also negligible, thus we can assume it as constant. The factors of ν in the denominators of equations (2.12) and (2.15) are used so that $g(\nu)$ and $f(\nu)$ are directly proportional to the Einstein B coefficients for absorption and emission (equations (1.4) and (1.5)). These line-shape functions incorporate all of the vibronic structure of the isolated molecule spectrum, i.e. gas phase, and in addition account for some spectral broadening, i.e. repulsive and non-polar attractive interactions of the probe with the non-polar solvent. When using these line-shape functions for polar solvents, we assume that the non-polar spectra are purely homogenously broadened and that this homogenous broadening is the same in all solvents. These assumptions seem to be justified for highly polar probes of the kind used in this work and many others where the effects of polar interactions dominate in determining spectral shifts and width [36].

The uncertainty of this estimation procedure was shown to be usually less than 200 cm⁻¹ [20, 36]. When the excitation is near the maximum of the absorption and
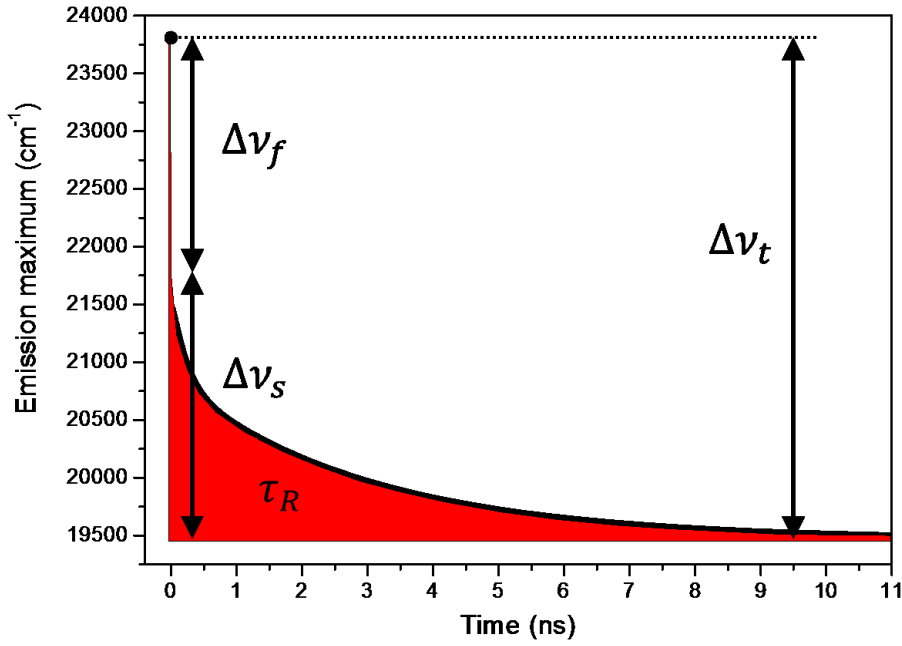
Figure 2.6: The total amount of TDFS $\Delta\nu_t$ is obtained from the time-zero estimation, which accounts for the fast (below instrumental resolution) TDFS ($\Delta\nu_f$), and from the experimentally resolved slower (above instrumental resolution) TDFS ($\Delta\nu_s$). The average relaxation time (τ_R) is defined as area under the normalized TDFS curve (equation (2.7)).

individual vibrational modes are not resolved (the absorption and emission spectra are unstructured), then the estimation of the position of the emission maxima at time zero $\nu_{em}^p(0)$ can be simplified as follows:

$$\nu_{em}^p(0) \approx \nu_{abs}^p - (\nu_{abs}^{np} - \nu_{em}^{np}) \qquad (2.16)$$

where ν_{abs}^p, ν_{abs}^{np} and ν_{em}^{np} are the absorption frequency in the polar medium, absorption and emission frequencies in nonpolar medium, respectively. The uncertainty of this simplified time-zero estimation was found to be less than 250 cm^{-1} [36]. Only when time-zero estimation is included, one can speak about the total amount of TDFS, provided the lifetime of the fluorophores is long enough to cover the whole relaxation process (Figure 2.6).

2.5 Fluorescence correlation spectroscopy

Fluorescence correlation spectroscopy (FCS) has been developed in the early seventies as a special case of relaxation analysis. Classical relaxation methods induce certain kinds of external perturbations such as optical excitation, temperature or

pressure jump, and then measure the rate of the relaxation of the system back to thermodynamic equilibrium (section 2.4.1) [42]. These methods take advantage from the formulation of the fluctuation–dissipation theorem, which states that the dynamics governing the relaxation of a system out of equilibrium are embedded in the equilibrium statistics [43]. On the other hand, FCS investigates the system at thermal equilibrium, where all of the processes are in fact statistical fluctuations around equilibrium. Such fluctuations are represented as noise patterns of the measured signal, in this case fluorescence. The FCS method is based on a statistical analysis of these fluorescence intensity fluctuations which have two important parts. The temporal part (duration of the fluctuations) provides information about kinetic properties, e.g. diffusion, and the amplitude part (magnitude of the changes in fluorescence intensity) provides thermodynamic properties, e.g. particle number fluctuations.

Although, the principal ideas behind FCS as well as its main applications were already established since its beginnings, the technique was still rather cumbersome and poorly sensitive mainly because of low detection efficiency, large ensemble numbers and insufficient background suppression. Its renaissance came in 1993 with the introduction of the confocal illumination scheme in FCS [42–44].

Figure 2.7A illustrates the principle of the confocal microscope, where the incident excitation light is reflected by a dichroic mirror and focused by an objective with high numerical aperture into the sample. The emitted red shifted fluorescence passes through the dichroic mirror and is imaged onto a pinhole which filters out-of-focus light and afterwards onto a fast detector, e.g. a photomultiplier tube, PMT, or avalanche photodiode, APD. The signal is then processed by the computer.

Nowadays, FCS is typically performed on a fluorescence confocal microscope. The spatial resolution of the confocal microscope is limited via diffraction to roughly 1 fL. The rejection of out of focus light is trade of with the possibility of capturing the whole image at once, thus it is necessary to record the image point by point instead. The optical response of the microscope to a point source at the centre of the focus is referred to as the point-spread-function or observation volume [45]. The observation volume is the overlap between the excitation, detection and sample volumes and is usually approximated by a three-dimensional Gaussian with different lateral and axial dimensions (Figure 2.7B). The highest signal-to-noise ratio is obtained when there is on average approximately one particle in the detection volume. Thus, the size of the
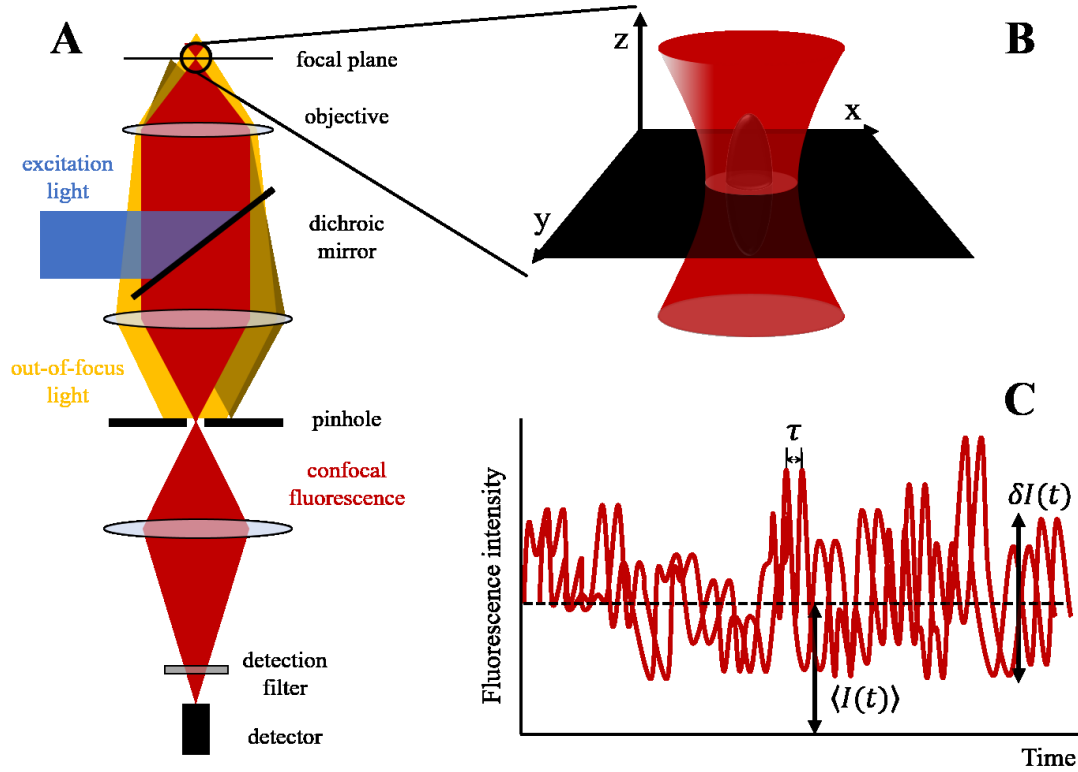
Figure 2.7: Principles of fluorescence confocal and correlation spectroscopy. **(A)** Simple scheme of confocal microscope, where a laser is used not because of the coherence properties of its light, but due to its stability and high power. **(B)** A schematic diagram of the focus of the confocal microscope with the excitation (red cone shaped) and detection (black ellipsoidal) volumes. **(C)** Self similarity of fluorescence intensity fluctuations $\delta I(t)$ around equilibrium $\langle I(t) \rangle$.

focal volume, in combination with low concentration, minimizes the number of emitting species, and therefore gives relevance to fluctuations (Figure 2.8).

One can use a mathematical tool, called autocorrelation analysis (therefore the name fluorescence correlation spectroscopy, FCS) in order to gain information about the florescence intensity fluctuations $I(t)$. The autocorrelation function is defined as [46]:

$$G(\tau) = \frac{\langle I(t) \cdot I(t + \tau) \rangle}{\langle I(t) \rangle^2} = \frac{\langle \delta I(t) \cdot \delta I(t + \tau) \rangle}{\langle I(t) \rangle^2} + 1 \qquad (2.17)$$

where

$$\langle I(t) \rangle = \frac{1}{T} \int_0^T I(t) dt \qquad (2.18)$$

denotes the time average of the signal and

$$\delta I(t) = I(t) - \langle I(t) \rangle \qquad (2.19)$$

are the fluctuations around the mean value $I(t)$.

The autocorrelation function $G(\tau)$ correlates a signal at a certain time t with the same signal delayed by lag time τ, and takes the temporal average. In other words, it measures self-similarity of the fluctuations, reflecting the probability that the signal at different times still belongs to the same molecular event (Figure 2.7C). Therefore, the decay time or diffusion time τ_D of the autocorrelation function is related to the residence time of the molecules in the observation volume [47].

In order to obtain desired parameters, diffusion coefficient and concentration, one have to fit the experimental autocorrelation function to a model function, which describes the sources of the intensity fluctuations. The most basic model describing the diffusion of a molecule through a three-dimensional (3D) Gaussian observation volume, with the diffusion coefficient and concentration parameters is:

$$G(\tau) = 1 + \frac{\gamma}{PN} \frac{1}{1 + \left(\frac{\tau}{\tau_D}\right)} \left(\frac{1}{1 + \left(\frac{\tau}{\tau_D}\right)\left(\frac{\omega_{xy}}{\omega_z}\right)^2} \right)^{1/2} \qquad (2.20)$$

where ω_{xy} is the radial distance and ω_z is the axial distance from the centre of the observation volume (considered as the point where the intensity has decayed by $1/e^2$), PN is the particle number and γ is the correction factor considering the intensity profile in the focal volume (Figure 2.8). This factor was introduced by Thompson and its value depends on the experimental geometry setup. In the case of 3D Gaussian volume element profile, the value of the correction factor γ is equal to $2^{-3/2}$ and in the case of the 2D Gaussian profile, its value is 0.5 [45, 48]. The main motivation for including the correction factor into the model is the difficulty in determining the observation volume. Nevertheless, many research groups choose $\gamma = 1$. With this approach, the amplitude of autocorrelation function is inversely proportional to the average number of observed molecules in the observation volume, $G(0) = 1/N$, and thus to the concentration of the fluorescent particles in the solution. The effective volume is then given by:

$$V_{eff} = \pi^{\frac{3}{2}} \omega_{xy}^2 \omega_z \qquad (2.21)$$

One can determine V_{eff} by measuring a dye with known diffusion coefficient D by obtaining the τ_D, which is directly related to the diffusion coefficient:

$$\tau_D = \frac{\omega_{xy}^2}{4D} \qquad (2.22)$$

Knowing the size of the focus, one can estimate its volume and therefore the concentration of the solution as well as the diffusion coefficient of the investigated system. Although the radius of the beam-waist is determined, the real shape of the detection volume may differ from the assumed one, e.g. because of beam astigmatism.
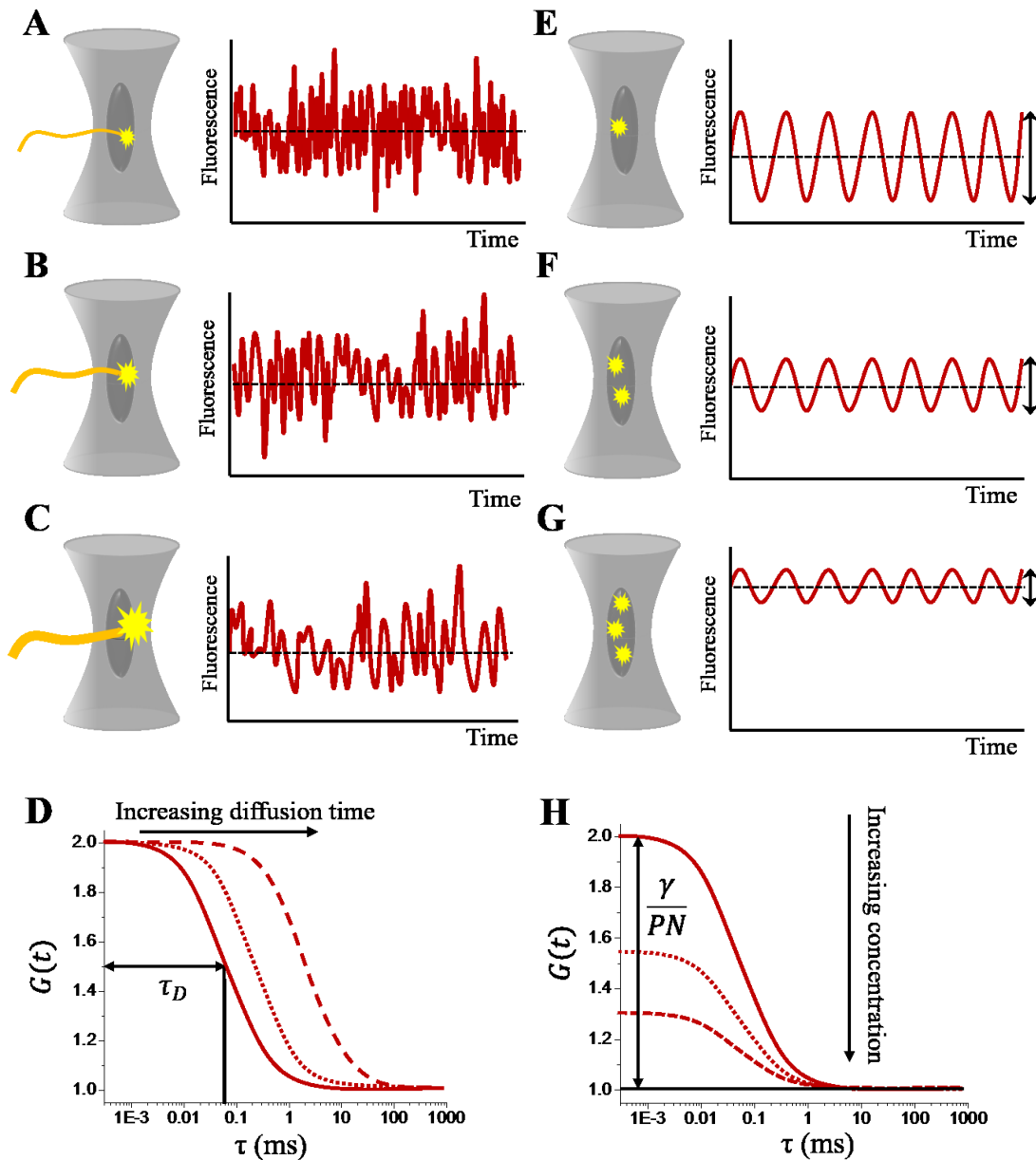
Figure 2.8: Diffusion time **(D)** and amplitude **(H)** are prominent parameters that can be extracted from the autocorrelation function. With increasing mass, the residence time of the molecule in the observation volume is longer and thus the corresponding diffusion time increases **(A-C)**. The half-value decay time provides a good estimate of the average diffusion time, from which the diffusion coefficient can be determined. An increase in particle number results in an increase in average fluorescence intensity, but the individual signal fluctuation caused by one specific molecule entering or leaving the observation volume becomes less pronounced **(E-G)**. The autocorrelation amplitude is inversely proportional to the particle number, thus an increase in particle number or concentration, means a decrease in amplitude. Adapted from [50].

38

Furthermore, the radius of the beam-waist in the reference solution may vary from that in the sample of interest, because of differences in refractive indices.

In the case of a two-dimensional sample like a planar lipid bilayer, the observation volume is actually defined by the intersection of the focus and the plane of the sample. In that case, the observation area can be described by a diffraction limited 2D Gaussian profile and the autocorrelation function is given by [49]:

$$G(\tau)_{2D} = 1 + \frac{\gamma}{PN} \frac{1}{1 + \left(\frac{\tau}{\tau_D}\right)} \tag{2.23}$$

In general, it is not only the diffusion through the observation volume that leads to fluctuations in the fluorescence intensity. Other sources like internal dynamics, the rotation of the fluorophores connected to varying excitation probabilities, or photophysical fluctuations, e.g. due to population of the triplet state, can occur [47]. The triplet state can be considered non-fluorescent. Therefore, an average fraction of fluorophores in triplet state T and intersystem crossing relaxation time τ_{tr} in the theoretical model needs to be included [48]:

$$G(\tau)_{2DT} = 1 + (1 - T + Te^{-\frac{\tau}{\tau_{tr}}}) \left(\frac{\gamma}{PN[1 - T]}\right) \left(\frac{1}{1 + \left(\frac{\tau}{\tau_D}\right)}\right) \tag{2.24}$$

In experiments with lipid bilayers where molecules partition weakly to the membrane, 3D dimensional diffusion in the aqueous phase of the molecules not associated with the membrane, can be observed. In such situations we have to include the contributions from 2D and 3D diffusion to the autocorrelation function [48, 51]:

$$G(\tau)_{2D3DT} = 1 + \frac{1}{PN(1 - T)} \left(1 - T + Te^{-\frac{\tau}{\tau_{tr}}}\right) \cdot$$

$$\left(\frac{2^{-\frac{3}{2}} \cdot FRa}{1 + \left(\frac{\tau}{\tau_{D3}}\right)} \frac{1}{\left(1 + \left(\frac{\tau}{\tau_{D3}}\right)\left(\frac{\omega_{xy}}{\omega_z}\right)^2\right)^{\frac{1}{2}}} + \frac{0.5 \cdot (1 - FRa)}{1 + \left(\frac{\tau}{\tau_{D2}}\right)}\right) \tag{2.25}$$

where FRa is the percentage of bound molecules within the PN value. τ_{D2} and τ_{D3} are diffusion times of membrane bound (2D) and unbound (3D) molecules within the observation volume. τ_{D3} is determined by a measurement in bulk solution.

2.5.1 Z-scan FCS

FCS in planar systems suffers also from errors caused by irreproducible axial positioning of the very thin sample (like lipid membrane) within the detection volume. If the plane of the sample does not coincide exactly with the waist of the focus, the divergence of the beam leads to a larger detection area and, thus, larger PN and τ_D. Z-scan technique overcomes the need for external calibration for correct determination of the diffusion coefficients and concentrations. By using a laser-scanner that deflects the laser beam in two directions directly in front of the objective lens, it is possible to convert the confocal microscope into a laser-scanning confocal microscope (LSCM), which may also be used for fluorescence imaging of the sample. In our case, we used LSCM to scan along the z-axis of the microscope (therefore Z-scan), thus changing the distance between the sample and the waist of the focus. The principle of this approach is based on the acquisition of individual point measurements along the optical axis of the microscope with a defined step (Δz) of typically 150 or 200 nm (Figure 2.9A). Diffusion time and particle number depend quadratically on Δz [48, 49]:
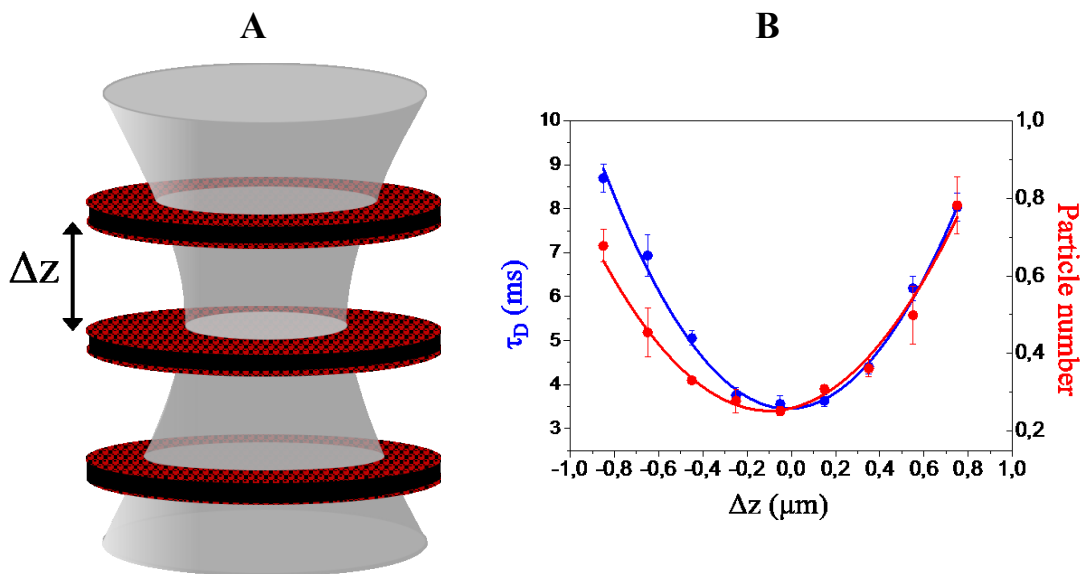
Figure 2.9: Principles of the Z-scan technique. **(A)** Schematic illustration of the influence of the axial sample position on the size of the detection area, thus on particle number and diffusion time. In order to obtain correct parameters, planar lipid bilayer is scanned along the z-axis within the focused beam and the autocorrelation curve is recorded at each point of the scan. **(B)** Both prominent parameter, τ_D and PN, are plotted against the Δz position. Desired parameters, diffusion coefficient and concentration, are directly obtained from the fit of the parabolic dependencies with the suitable model (equations (2.26) and (2.27)).

$$\tau_D = \frac{\omega_{xy}^2}{4D}\left(1 + \frac{\lambda^2 \Delta z^2}{\pi^2 n^2 \omega_{xy}^4}\right) \tag{2.26}$$

$$PN = \pi c \omega_{xy}^2 \left(1 + \frac{\lambda^2 \Delta z^2}{\pi^2 n^2 \omega_{xy}^4}\right) \tag{2.27}$$

where D is the lateral diffusion coefficient, c is the average concentration of diffusing fluorescence molecules in the illuminated area, n is the refractive index of the medium, and λ is the excitation wavelength (Figure 2.9B).

2.5.2   Fluorescence cross correlation spectroscopy

Cross correlation analysis is a straightforward way to find common features in two independently measured signals. In the case of fluorescence cross-correlation spectroscopy (FCCS), splitting the fluorescence into two detection channels and performing the cross-correlation between them is the simplest solution for unwanted artefacts introduced by the detector, e.g. the so-called "afterpulsing" of an APD or intensity fluctuations of the illumination source. The more interesting case, however, is the dual colour mode of FCCS. In principle, this FCCS mode involves two spectrally different fluorophores that are excited within the same detection element using two overlapping laser beams and separate detection pathways. The intensity traces from the two spectral channels, here called red and green channels, $I_r(t)$ and $I_g(t)$, are used to calculate the autocorrelation functions, $G(\tau)_r$ and $G(\tau)_g$, as well as the cross-correlation function:

$$G(\tau)_{rg} = \frac{\langle I_r(t) \cdot I_g(t + \tau)\rangle}{\langle I_r(t)\rangle\langle I_g(t)\rangle} = \frac{\langle \delta I_r(t) \cdot \delta I_g(t + \tau)\rangle}{\langle I_r(t)\rangle\langle I_g(t)\rangle} + 1 \tag{2.28}$$

A cross-correlation is detected when the signal fluctuates simultaneously in both channels, for example due to the fact that differently labelled molecules are diffusing as a complex. Therefore, FCCS has been applied to, for example, investigate molecular binding in solution as well as direct protein-protein binding in living cells [52, 53].

There are several factors that affect FCCS measurements. One of the main complications is that usually the red and green detection volumes have different sizes and that chromatic aberrations cause an axial shift between the detection volumes. The resulting imperfect overlap leads to a reduced cross-correlation. Quantitative analysis of spectral cross-correlation curves requires the knowledge of the spatial overlap, as

well as the sizes of the red and green detection volume [54]. This can be overcome by calibration measurements using a cross-correlation standard with a known degree of double labelling. Often short DNA or RNA fragments labelled with both red and green fluorophore are used, but 100% labelling cannot usually be guaranteed. In this work, we used two-colour labelled DNA. The ratio of the cross- and autocorrelation curve amplitudes for green and red dye, $(G(0)_{rg}/G(0)_g$ and $G(0)_{rg}/G(0)_r$, respectively, were used as the estimation of the maximum possible cross-correlation that can be obtained by our setup. These ratios were then used as correction factors for the cross-correlation measurements.

Another problem is the spectral cross-talk, where the fluorescence signal of one of the fluorophores is detected in the other channel. It is caused mainly by the fact that the fluorophore with the longer wavelength emission can typically be excited with both lasers. This introduces additional similarities between the fluorescence fluctuations in the two channels and can therefore result in a false-positive cross-correlation [45]. To eliminate spectral cross-talk, the pulsed interleaved excitation (PIE) can be used, where two alternating excitation laser sources are synchronized to a master clock. The fluorescence signal is recorded with a TCSPC detection unit, and information regarding which excitation source generated the detected photon is recorded (Figure 2.10).

However, there are more subtle problems concerning FCS and dual colour FCCS, the potential artefacts mentioned above are the main source of errors in data interpretation. Detailed information can be found in original papers, books and reviews [43, 45, 47, 53–55].

2.5.3   FCS instrumentation

Experiments were performed on home build confocal microscope consisting of an inverted confocal microscope commercial base IX71 (Olympus). For excitation, pulsed diode lasers (LDH-P-C-470, $\lambda = 470$ nm and LDH-D-C-635, $\lambda = 635$ nm, both Picoquant) with repetition rate 13 MHz and 10 μW were used. The pulsed interleaved excitation was used in order to avoid artefacts caused by spectral cross-talk. The light was up-reflected to a water immersion objective (UPLSAPO 60x, Olympus) with a 470/635 dichroic mirror. Signal was detected by two single photon avalanche diode

detectors using 515/50 and 697/58 band pass filters (Chroma) for green and red channel, respectively. Z-scans were performed at the top of single vesicle. The membrane was vertically scanned in 15 steps spaced 200 nm apart from each other. At each step 60-second-long single point measurement was recorded. Data obtained by Z-scan method were analysed using home-written scripts in Origin (OriginLab).
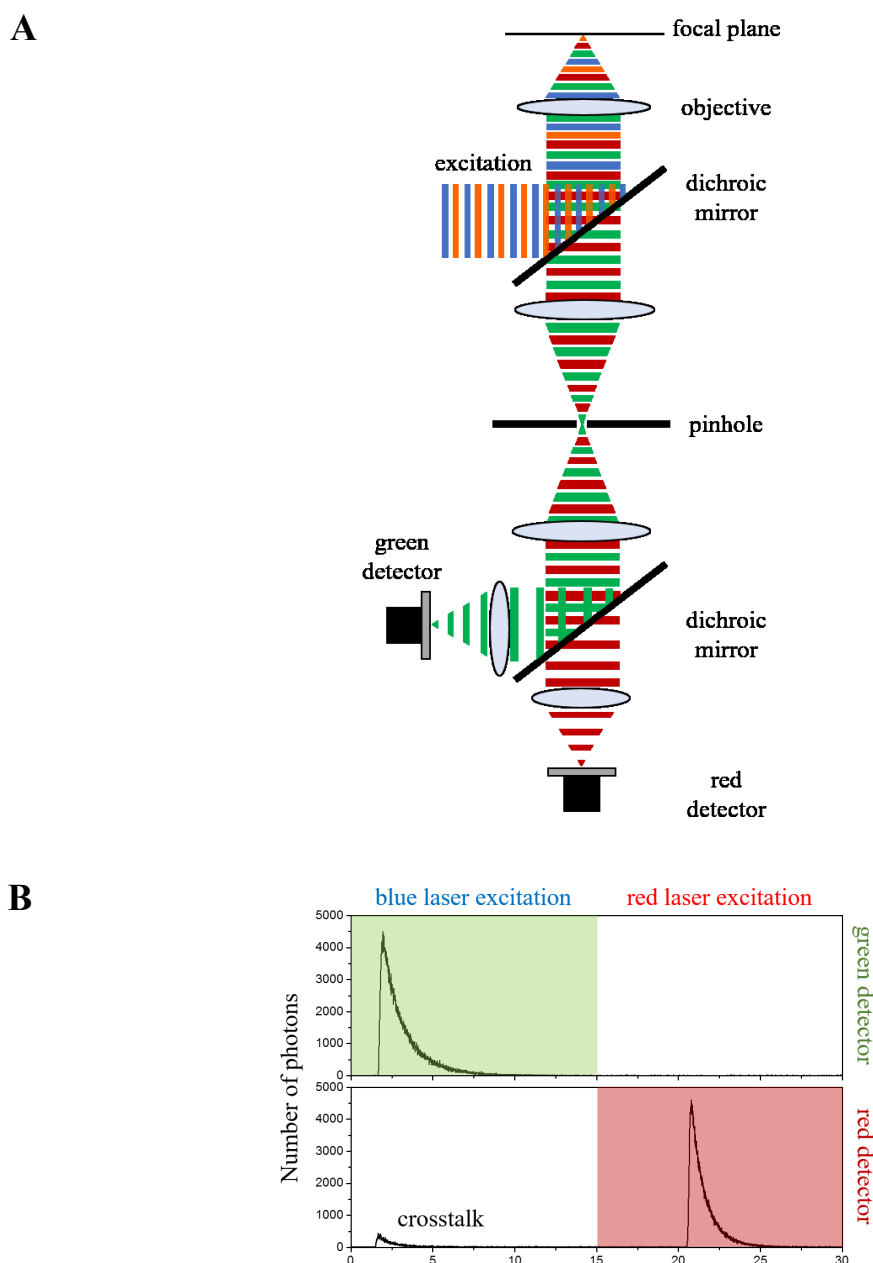
Figure 2.10: Principle of pulsed interleave excitation. **(A)** Schematic diagram of a dual-channel confocal microscope with pulsed interleaved excitation. The excitation pulses are shown in blue and orange whereas fluorescence is depicted in green and red. **(B)** Fluorescence decays measured by the TCSPC unit. Photons arriving after the blue laser excitation (470 nm) are detected during the first 15 ns and photons arriving after the red laser excitation (637 nm) are detected between 15 and 30 ns. The photons detected in the red detector before 15 ns are from fluorophores that were excited with the blue laser but emit in the red part of the spectra. This signal is called crosstalk.

3. Applications of fluorescence spectroscopy in protein science

3.1 Solvatochromic fluorene-linked nucleoside and DNA as colour-changing fluorescent probes for sensing interactions

Investigations of DNA solvation dynamics have been performed with diverse environment-sensitive fluorescent nucleoside analogues (FNAs) and their corresponding oligonucleotide probes placed inside the duplex-DNA either by covalent attachment or by non-covalent minor groove binding [56]. Apart from 2-aminopurine and other FNAs which respond to changes in the microenvironment by changing fluorescence intensity [57–71], solvatochromic fluorophores provide changes in emission maxima (emission colour) as an additional source of information. For example, nucleosides with tethered 6-propionyl-2-(dimethylamino)-naphthalene (Prodan) moiety [72], have been used to monitor microenvironmental changes in the major and minor grooves of B and Z-DNA [73, 74] and for the detection of single nucleotide polymorphism [75].

The characterized dynamics in DNA were found to be mainly nonexponential and extended in subpicosecond to nanoseconds timescales, best described by a power-law relaxation [76]. There is no unified explanation of such dispersed dynamics primarily because of the complicated coupling between motions of components localized in the closest (< 1 nm) vicinity of the probe: water molecules, segments of the DNA molecule as well as cations. However, for an interpretation one should keep in mind that the solvent relaxation response of bulk water occurs on the sub-picosecond time scale [77] and slower responses (i.e on the ps and ns time-scale) have to be attributed to DNA dynamics [23].

In this part of the work, a new fluorescent 2′-deoxycytidine nucleoside linked to a highly solvatochromic fluorene derivative through a non-conjugated tether was converted to dNTP and then used in enzymatic synthesis of color-changing DNA probes. The fluorene-linked DNA can be used as fluorescent probes for DNA-protein (p53) or DNA-lipid interactions exerting significant colour changes visible even by the naked eye. They also appear to be suitable for time-dependent fluorescence shift studies in DNA yielding information on DNA hydration and dynamics.

44

3.1.1 Experimental

Solvatochromic push-pull fluorene fluorophore building block 8 and labelled nucleoside dC^{FL} bearing the fluorene fluorophore were designed and synthesised (Figure 3.1). Furthermore, the 50-base pair fluorene labelled double stranded DNA were synthesized (DNA^{FL}) bearing two tethered solvatochromic fluorene moieties and contains the consensus recognition site of human transcription factor p53. Synthesis of fluorene label and the DNA^{FL} was done by Dmytro Dziuba from Michal Hocek group at IOCB in Prague. Details about synthesis and sample preparation can be found in Attachment I.

TDFS measurements with the DNA^{FL} in variety of environments were performed: DNA^{FL} in buffer, DNA^{FL} in buffer-glycerol mixture, DNA^{FL}-p53CD_GST (the core domain of the human transcription factor p53 with a GST tag expressed in bacteria as a model DNA-binding protein [78, 79]) and DNA^{FL}-DOTAP (1,2-dioleoyl-3-trimethylammonium-propane). DOTAP was obtained from Avanti Polar Lipids, Inc.

TDFS measurements were performed using steady state and TCSPC instrumentation as described in sections 2.1.1 and 2.2.1, respectively. Measurements were performed at 5°C except DNA^{FL}-DOTAP measurements which was performed at 23°C. TDFS data were evaluated as described in section 2.4.1 and time zero estimation were performed as described in section 2.4.2.

In order to prepare DOTAP liposomes, appropriate volume of DOTAP stock solution (10 mM in $CHCl_3$) was transferred into a glass vial and then the solvent was evaporated using a stream of nitrogen. The vial was placed into a vacuum desiccator for 20–30 min in order to remove the traces of chloroform. The dried lipid was vortexed (2500 rpm, 5 min) with appropriate volume of PBS (10 mM sodium phosphate buffer pH 7.4, 200 mM NaCl) to reach 1 mM DOTAP concentration. Then sample was sonicated for 10 min using a tip sonicator (Sonopuls HD 2070, Bandelin electronic GmbH, Germany) at 10% power, while cooled with a water bath at room temperature to give Small Unilamellar Vesicles (SUVs). SUVs were centrifuged at 16110g (Eppendorf centrifuge 5415 D) for 20 min to separate the contaminating metallic particles from the sonicator tip. The supernatant was collected and used without any additional treatment. Details about preparation of other samples can be found in Attachment I.
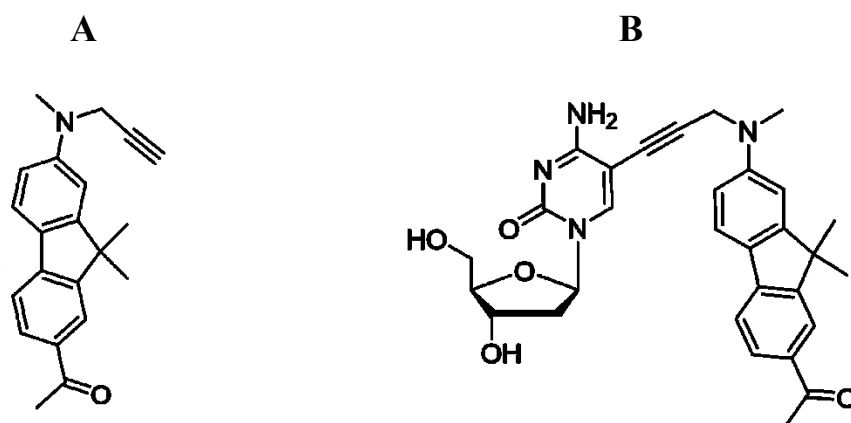
A   **B**

Figure 3.1: Chemical structures of building block 8 **(A)** and nucleoside dC^{FL} **(B)**.

3.1.2   TDSF   measurement   of   DNA^{FL} in   different microenvironments

The TDFS of the labelled DNA^{FL} with dC^{FL} exposed to the major groove of DNA in several microenvironments was measured. The experimentally observed transient Stokes shifts for DNA^{FL} in buffer, buffer-glycerol mixture (1:1) and DNA^{FL} – p53CD_GST complex are 70 cm^{-1}, 130 cm^{-1}, and 40 cm^{-1}, respectively. These values are negligible compared to the total amount of the Stokes shift of 5320 cm^{-1}, 5020 cm^{-1}, and 5120 cm^{-1}, respectively, obtained by the time-zero estimation (Figure 3.2A and Table 3.1). These findings indicate that the nano-vicinity of the probe is different than the probe nano-vicinity in plain water (estimated total amount of the Stokes shift of dC^{FL}TP is about 5600 cm^{-1}), but highly hydrated. The significant smaller Stokes shift for the DNA^{FL}-p53CD_GST complex indicates a less hydrated probe environment when compared to the free DNA molecule. As practically the entire solvation dynamics is occurring on a time-scale faster that the resolution of the experiment (i.e faster than 30 ps), the ensemble solvent dynamics is due to fast segmental motions of the DNA with possibly some contribution of bulk water. These observations are comparable with literature reported dynamic Stokes shifts. Independent of chromophore (Coumarine 102, 4′,6-diamidino-2-phenylindole (DAPI), Hoechst 33258 and 2-hydroxy-7-nitro-fluorene (HNF)), and way of labelling (nucleobase replacement or non-covalent minor groove-binding), the largest part of the transient Stokes shift occurs on the time scale faster than 30 ps [76, 80–84]. However, in all these cases, except for HNF, a minor, but significant nanosecond component is present [56, 83, 85].

A significantly different picture was observed for the DNA^{FL} incorporated in DNA^{FL}-DOTAP lipoplexes. While the total amount of the Stokes shift decreased only slightly to 4650 cm^{-1}, the experimentally observed transient Stokes shifts increased to 65% and 72% of the total amount of the Stokes shifts in the cases of 1:1 DNA^{FL}-DOTAP charge ratio and 1:4 DNA^{FL}-DOTAP charge ratio, respectively (Figure 3.2B and Table 3.1). Now, almost the entire solvation dynamics occurred on the nanosecond time scale. Upon addition of DOTAP to the DNA^{FL} accompanied by lipoplexes formation between the DNA^{FL} and DOTAP, the nano-vicinity of the DNA^{FL} became less hydrated compared to the DNA^{FL} alone in the buffer and the microenvironment mobility decreased dramatically. Addition of more DOTAP to DNA^{FL}-DOTAP lipoplexes resulted in a further decrease of the slower relaxation time (τ_R) while the hydration stayed at almost the same level. This observation suggests that the lipoplexes structure is getting more compact upon addition of DOTAP, which is in line with previously reported results, where the experiments with the addition of DOTAP resulted in more compressed lipoplexes and growths of their size [86]. As the time-scale of the TDFS is comparable with probes located at the external interface of a lipid [20], we speculate that the dC^{FL} dye incorporated in the DNA^{FL} double-helix is probing mainly the hydrated positively charged DOTAP headgroups which are in close contact with the DNA^{FL} incorporated in DNA^{FL}-DOTAP lipoplexes.

Parameter	DNA^{FL} buffer	DNA^{FL}/DOTAP charge ratio 1:1	DNA^{FL}/DOTAP charge ratio 1:4
Δv [cm^{-1}]	5320	4615	4650
τ_R [ns]	<0.04	0.31	0.54

Table 3.1: TDSF parameters for DNA^{FL} in different environments.

3.1.3   Discussion

The modified nucleoside was shown to be suitable for probing site-specifically dynamics and hydration of the DNA using TDFS measurements. Notably, such a nanosecond TDFS has not been described for the DNA system yet. Together with the large total amount of the Stokes shift, it makes this probe a prospective versatile tool for investigating DNA interactions in biophysical and bioanalytical studies. Furthermore, lipoplexes investigation is of the great interest for the gene transfer to the

cells. Studying the DNA^{FL} lipoplexes could reveal not only DNA dynamics itself, but also the processes involved in DNA delivering into the cells [87].
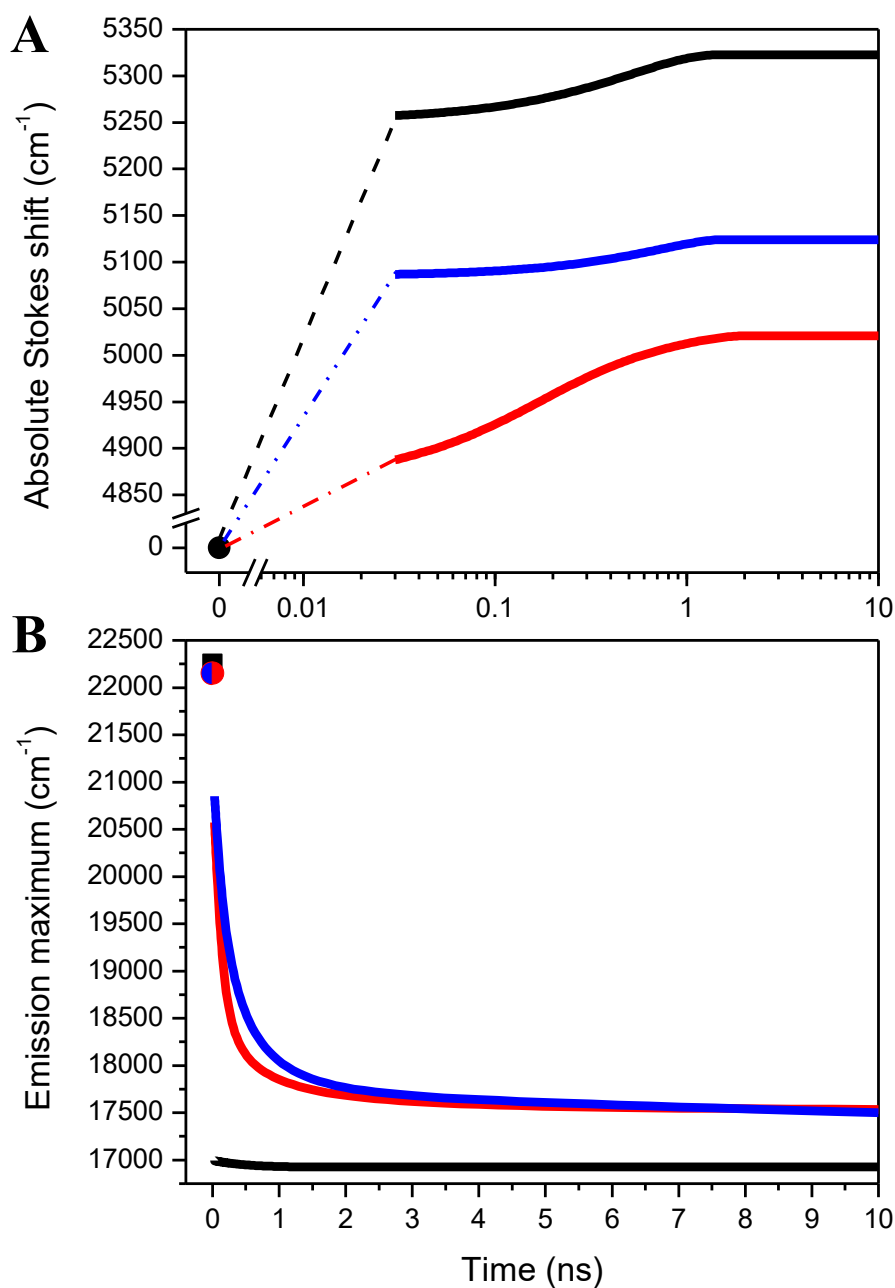
Figure 3.2: A) Time evolution of the TRES maxima $v(t)$ subtracted from the time zero estimation (black point) for labelled DNA in buffer (black), in a mixture of buffer and glycerol (ratio 1:1 - red), and in buffer with protein (blue). **B)** Time evolution of the TRES maximum for DNA in buffer (black), DNA^{FL}-DOTAP 1:1 charge ratio (red) and DNA^{FL}-DOTAP 1:4 charge ratio (blue). Time zero ($v_{em}^{p}(0)$) is estimated at 22 250 cm⁻¹ for DNA (black square) and 22 150 for DNA^{FL}-DOTAP (red and blue point).

3.2 Fluorescence quenching of (dimethylamino)naphthalene dyes Badan and Prodan by tryptophan in cytochromes P450 and micelles

We have investigated fluorescence quenching of two 2-(N,N-dimethyl)aminonaphthalene-6-propionyl dyes Badan and Prodan by tryptophan (Trp) in two cytochrome P450 mutants and in Brij® 58 micelles (Figure 3.3 and Figure 3.4). Fluorescence of dimethylnaphthalene–based dyes originates from an intramolecular charge transfer excited state in which electron density is transferred from the NMe_2 group to the electron-accepting carbonyl substituent at the naphthalene 6-position [4, 10, 20, 88, 89]. Their photophysics are strongly medium-dependent, presumably due to the molecular dipole moment increasing upon excitation and specific solvation, including hydrogen bonding [4, 89]. The dyes are frequently used as probes to estimate polarity and dynamics of the local environment in proteins [10, 90, 91] as well as micelles and membranes [4, 10, 20, 88] by measuring stationary and time-resolved fluorescence spectra [10]. The environmental dependence of Badan fluorescence lifetimes was employed, for example, in a glucose sensor [92]. This utility prompted the development of dimethylnapthalene-based dyes with a broad range of protein labelling groups, including Badan (thiol-reactive bromine, Figure 3.3), Acrylodan (cysteine-reactive ethylene), the unnatural amino acid Aladan for incorporation into peptide chains, Danca, which binds apomyoglobin in a single orientation through a carbonycyclohexyl group, and Dansyl, where the 6-propionyl is replaced by a sulfonamide. Prodan (and its derivatives with long aliphatic chains) are typically used as non-covalent membrane probes [10, 20].

(Dimethylamino)naphthalene-type dyes also serve as energy acceptors from electronically excited tryptophan (*Trp) [10, 93] or as energy donors toward hemes in cytochromes, as utilized in FRET experiments [94, 95]. Photoinduced electron transfer, in contrast, is not a common quenching mechanism of these dyes, although Badan photoreduction by Trp was proposed to occur in one of the CYP3A4 conformers [96]. An opposite process, photooxidation of a (dimethylamino)naphthalene by a guanine cation has been observed in a protein-DNA complex [97].

In this part of the work, the compelling evidence for ET quenching of Badan fluorescence by comparing the behaviour of Badan-labelled cytochrome P450 mutants
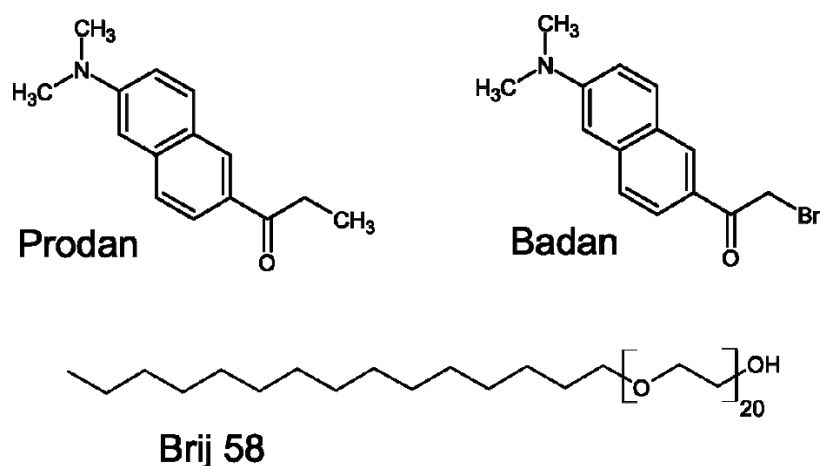
Figure 3.3: Chemical structures of Badan and Prodan dye molecules (top), and the Brij® 58 detergent molecule (bottom).

(CYPs, Figure 3.4) with and without a Trp residue in the dye vicinity, is presented. The occurrence of photoinduced ET from Trp to electronically excited 2-dimethylnaphthalene-6-propionyl dyes is further supported by electrochemistry and by fluorescence quenching of Badan and Prodan in Trp-containing micelles. Observation on an ET quenching mechanism for these dyes highlights an important constraint for their use as microenvironmental probes, while opening new avenues for study of ultrafast dynamics associated with short range interactions in biological systems.

3.2.1   Experimental

Badan and Prodan were obtained from Anaspec and Invitrogen, respectively, and used without further purification. Brij® 58 and tryptophan were obtained from Sigma Aldrich. Badan (Prodan) was added in a 1:2000 ratio to a ~8 mM solution of the detergent Brij® 58 in 20 mM TRIS buffer (pH 8) in order to prepare Badan (Prodan)/Trp-containing micelle solutions. The Brij® 58 concentration was kept two orders of magnitude above the critical micelle concentration (CMC ~ 0.08 mM)[98]. Trp was dissolved separately in a basic aqueous solution (NaOH, pH ~ 12). Aliquots of the Trp solution were added stepwise to the solution of Badan (Prodan)-containing micelles to achieve desired Trp concentrations. Samples were mixed by manual shaking directly in the cuvette, followed by measuring stationary fluorescence spectra and decay traces. To measure corresponding I_0 and τ_0 values, the same aliquots of aqueous NaOH solution not containing Trp were added to the same micelle/dye stock
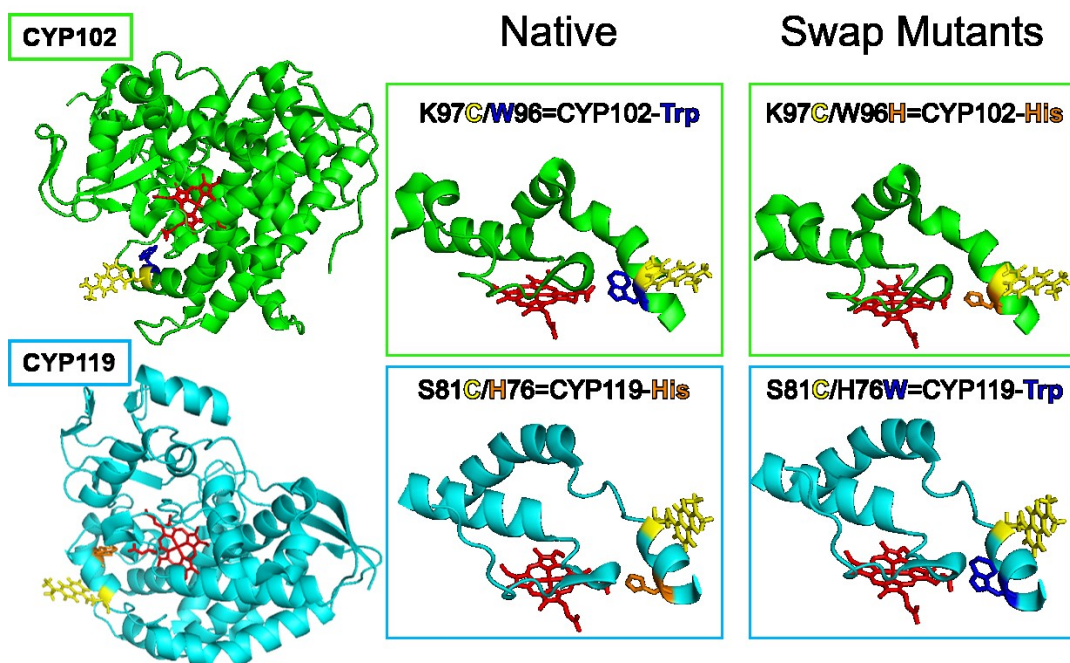
50

Figure 3.4: Schematic structures and abbreviations of investigated Badan-labelled cytochrome P450 mutants *Bacillus megaterium* CYP102 (top, also known as P450 BM3 or CYP102(A1)) and *Sulfolobus acidocaldarius* CYP119 (bottom). Badan (yellow) is attached to Cys97 and Cys81, respectively. Native residues Trp96 of CYP102 and His76 of CYP119 (middle panels) are replaced by His96 and Trp76, respectively, in the swap mutants (right panels). Based on unlabelled protein structures: pdb 2IJ2 [99] (CYP102-Trp), pdb 1IO7 [98] (CYP119-His), and yet unpublished structure of CYP102-His, the heme (red), His (orange), Trp (blue), Cys and Badan (yellow) are shown. The Badan orientation was chosen arbitrarily for illustrative purposes.

solution, thus eliminating possible pH and concentration effects on the quenching measurements. The Trp concentration range examined in Badan quenching experiments was limited to about 20 mM since Badan aggregation occurred at higher Trp concentrations due to increased pH. Aggregation onset was indicated by a fluorescence blue shift and lifetime shortening (Figure 3.5). In the case of Prodan, no aggregation effect was observed. All measurements were performed at 23°C.

Protein expression and labelling were done by Katja E. Luxem and Maraia Ener from Harry Gray group at Caltech in California. Details about the CYP102 (also called P450 BM3 or CYP102(A1)) C62A/C156S/K97C triple mutant (CYP102-Trp) and histidine-containing mutant C62A/C156S/K97C/W96H (CYP102-His) and CYP119 mutants S81C/H76 (CYP119-His) and S81C/H76W (CYP119-Trp) preparation can be found in Attachment II.

Instrumentations for the measurements of stationary emission spectra and time-resolved fluorescence decays are described in sections 2.1.1 and 2.2.1, respectively. Fluorescence decays were fitted according to the equation (2.1) and average lifetimes
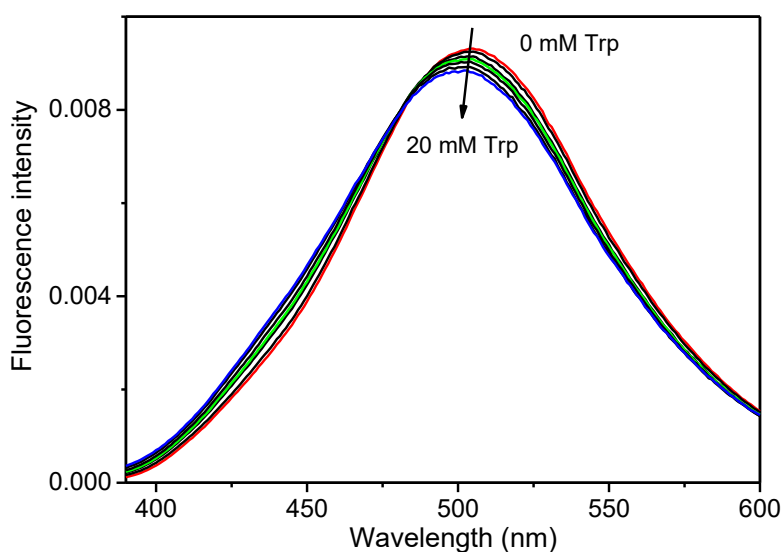
Figure 3.5: Area-normalized Badan fluorescence spectra in Brij® 58 micelles as a function on Trp concentration in the 0 – 20 mM range. Excited at 370 nm.

were calculated according to the equation (1.16) defined in section 1.3.6, where theoretical background and evaluation of fluorescence lifetime are described. Fluorescence decay was investigated at 550 nm, within the red side of the emission band. The emission wavelength of 550 nm was chosen in order to avoid interference from fast decay components due to medium relaxation instead of population decay. Instrumentation for the electrochemical measurements can be found in Attachment II.

3.2.2   Fluorescence quenching in Badan-labeled CYP mutants

All four investigated CYPs show a typical Badan fluorescence band at about 485 nm using excitation at 370 nm (Figure 3.6). Figure 3.7 shows that fluorescence of CYP102-Trp and CYP119-Trp decay faster than in the case of their His counterparts. Emission decay kinetics were multiexponential for all mutants, regardless whether Trp or His was present. Fitting to a triple exponential function yielded kinetics components occurring in the tens-of-picosecond (τ_1), hundreds-of-picosecond (τ_2) and nanosecond (τ_3) ranges (Table 3.2). Substituting His by Trp shortened all three lifetimes and strongly increased the relative amplitude of the fastest process (A_1) indicating that the excited-state quenching reactions occur in several parallel pathways with lifetimes ranging from tens of picoseconds to tens of nanoseconds. The average quenching rate constant is defined as:
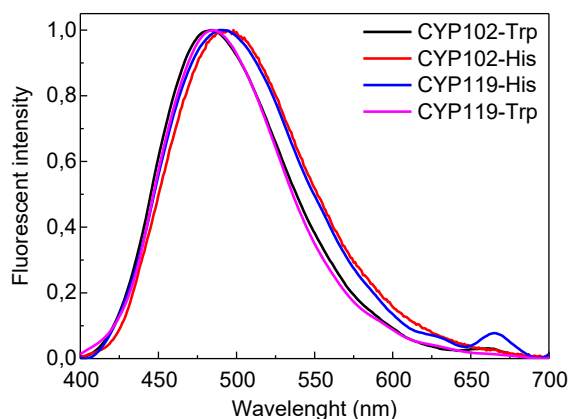
Figure 3.6: Stationary fluorescence spectra of Badan labelled CYPs: CYP102-Trp (black), CYP102-His (red), CYP119-His (blue), CYP119-Trp (magenta). Excited at 370 nm.

$$\langle k_q \rangle = \frac{1}{\langle \tau_{Trp} \rangle} - \frac{1}{\langle \tau_{His} \rangle} \qquad (0.1)$$

where $\langle \tau_{Trp} \rangle$ and $\langle \tau_{Trp} \rangle$ are average fluorescence lifetimes for Trp and His mutants, respectively. The average fluorescence lifetimes were calculated according to the equation (1.16). The average quenching rate constants are comparable for CYP119-Trp and CYP102-Trp (4×10^8 s^{-1} at 288 K), whereas the quenching rate constant $k_{q,3}$ (based on the slow kinetics component τ_3) is 1.4-1.6 times higher for CYP102-Trp, in accordance with a shorter Trp-Badan distance (Figure 3.4). As expected, both quenching rate constants slightly decreased on decreasing the temperature from 296 to 288 K (Table 3.2).

sample	T (K)	Lifetimes (ns)			Amplitudes (%)			Average lifetime [b] (ns)	$\langle k_q \rangle$ (s^{-1})	$k_{q,3}$ (s^{-1})
		τ_1 [a]	τ_2	τ_3	A_1	A_2	A_3			
CYP102-Trp	288	0.03[c]	0.48	2.24	96	3	1	0.86	4.5x10^8	1.0x10^8
CYP102-His	288	0.13	0.74	2.92	66	28	6	1.40		
CYP102-Trp	296	0.03[c]	0.40	2.13	96	3	1	0.95	5.1x10^8	1.4x10^8
CYP102-His	296	0.09	0.70	3.03	65	26	9	1.85		
CYP119-Trp	288	0.05	0.50	2.24	87	11	2	0.90	3.7x10^8	7.3x10^7
CYP119-His	288	0.10	0.69	2.68	69	26	5	1.34		
CYP119-Trp	296	0.05	0.53	2.42	89	10	1	0.94	3.8x10^8	8.8x10^7
CYP119-His	296	0.10	0.80	3.07	72	23	5	1.47		

[a]The τ_1 kinetics occur at the limit of the experimental time resolution and the corresponding lifetime and amplitude values were obtained by IRF deconvolution. Although this might introduce some absolute error, it did not affect significantly the relative change between His- and Trp-containing mutants. [b]Virtually identical average lifetime values were obtained from 4-exponential fits. Accuracy ±50 ps. [c]Estimated, at the limit of IRF deconvolution

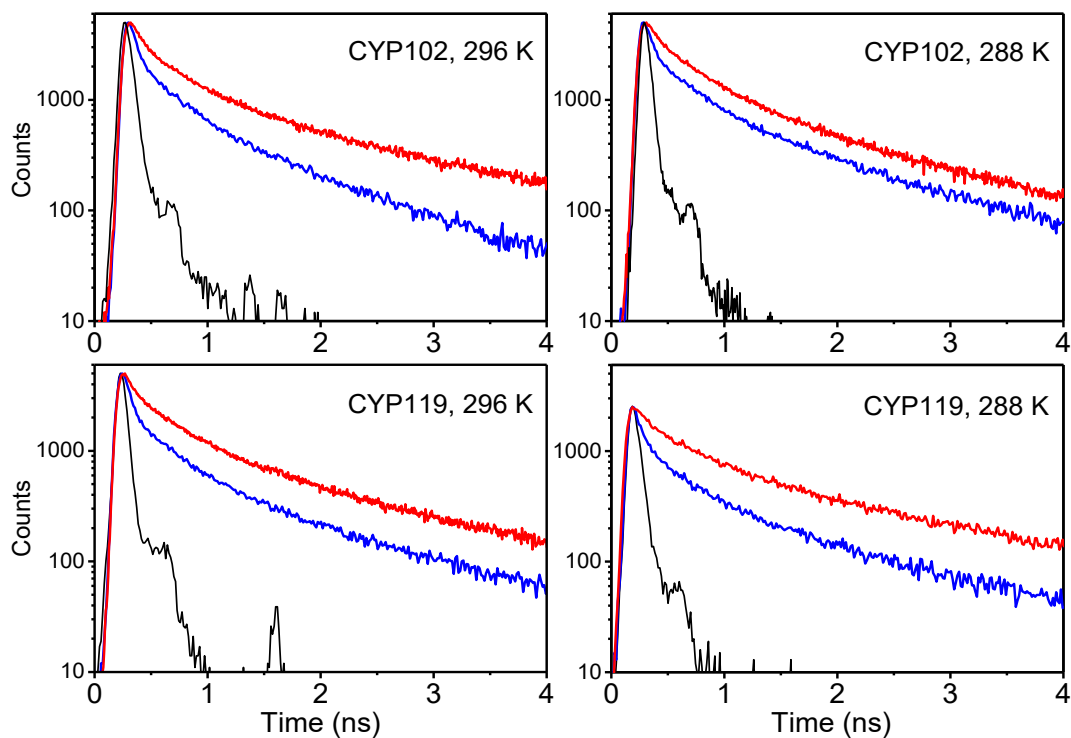**Table 3.2:** Fluorescence decay kinetics of Badan-labelled CYP mutants.

Figure 3.7: Fluorescence decay of Badan-labelled CYPs. Data for His and Trp mutants are shown in red and blue, respectively. Excitation at 373 nm and emission at 550 nm.

3.2.3　　Badan fluorescence quenching in micelles

Addition of a large excess of the surfactant Brij® 58 to an aqueous Badan solution (Tris, pH 8) strongly increased Badan solubility and shifted the fluorescence maximum from 550 to 500 nm (Figure 3.8), indicating the micellar environment is a good model for the protein (λ_{em} = 485 nm). Prodan showed very similar behaviour. Badan fluorescence decayed single-exponentially, τ_0 = 2.64 ns, whereas Prodan showed a small initial 0.55 ns rise followed by a 3.87 ns decay (Table 3.3 and Table 3.4). The lifetime-weighted rise amplitude was less than 10% of the decay amplitude. The rise component is tentatively attributed to a dynamic Stokes shift, whereby the fluorescence intensity initially increases in the red part of the band [4, 10, 20, 21].

Addition of Trp quenched fluorescence intensity more strongly than the lifetime (Figure 3.8 and Figure 3.9). This behaviour is characteristic of combined dynamic and static quenching [4, 10], that is described by Stern-Volmer (SV) plot (equations (1.11) and (1.12)).

Analysis of the lifetime quenching yielded a k_q value of 1.74×10^9 M^{-1}s^{-1} for Badan and 5.79×10^8 M^{-1}s^{-1} for Prodan (based on τ_{decay} values listed in Table 3.4).
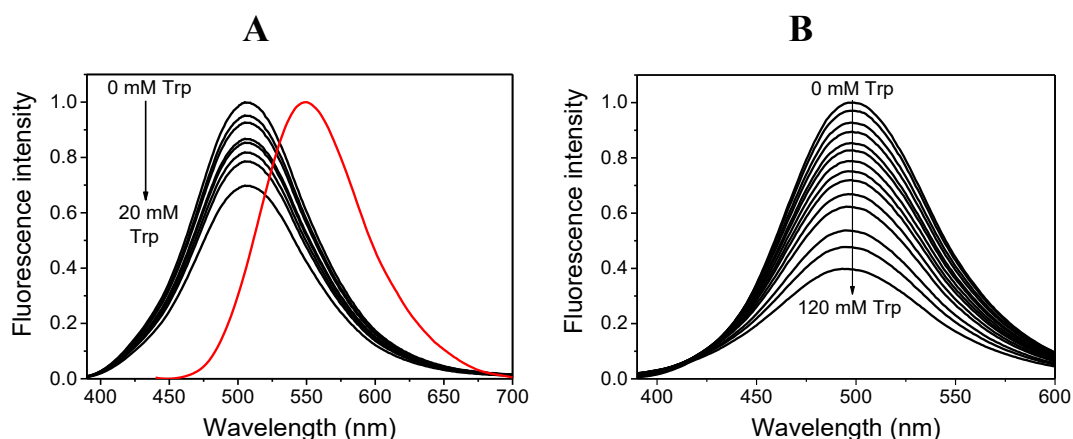
54

Figure 3.8: A) Stationary fluorescence spectra of Badan in Brij® 58 micelles measured at different Trp concentrations (black) and Badan spectrum in pure Tris buffer (red). **B)** Stationary fluorescence spectra of Prodan in Brij® 58 micelles measured at different Trp concentrations. Excited at 370 nm.

Lifetime quenching kinetics are virtually independent of the emission wavelength, as was checked for Badan at 500 nm (1.90×10^9 $M^{-1}s^{-1}$) and Prodan at 490 nm (5.74×10^8 $M^{-1}s^{-1}$).

Intensity-based SV plots (Figure 3.9) yielded (after correction for dynamic quenching) the bimolecular static quenching constant (or stability constant) K_s values of 14.7 M^{-1} and 3.5 M^{-1} for Badan and Prodan, respectively. The percentage of the
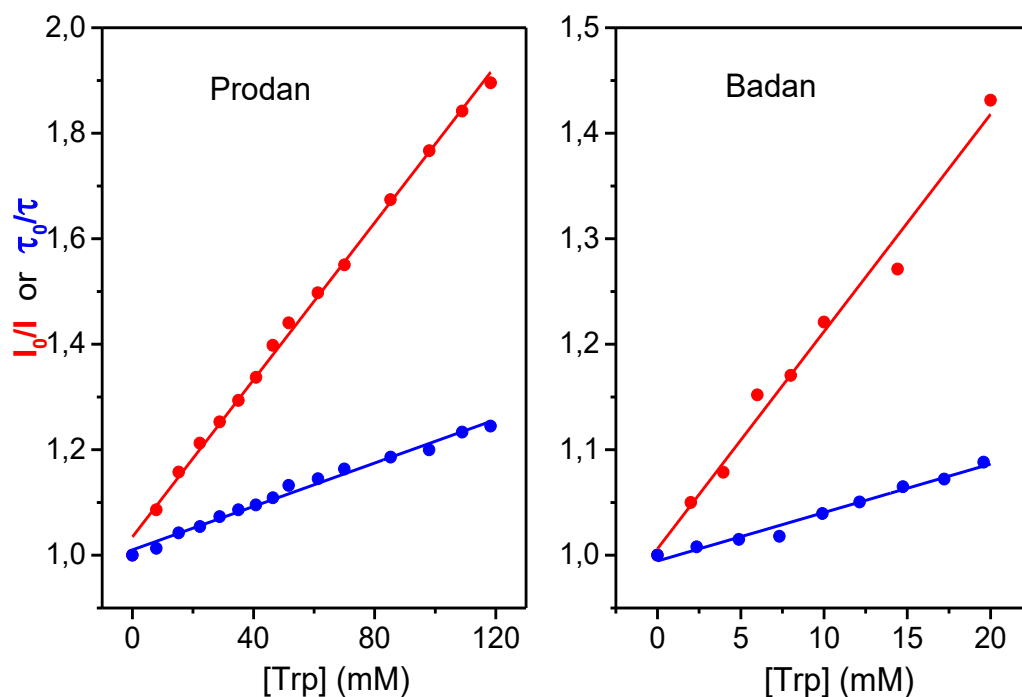

Figure 3.9: Fluorescence intensity (red) and lifetime (blue) Stern-Volmer plots of Prodan (left) and Badan (right) quenching by tryptophan in Brij® 58 micelles. All lifetime values were measured at 550 nm.

total intensity quenching due to static quenching was estimated as $100 \cdot K_s/(K_s + k_q\tau_0) \sim 76\%$ for Badan and ~61% for Prodan. Stationary fluorescence spectra also showed a very small blue shift of Badan fluorescence upon Trp addition, from 509 to 504 nm, with an isoemissive point at 484 nm (Figure 3.5). This effect indicates the presence of at least two slightly different Badan populations in the micelles, the red-absorbing one being preferentially quenched by Trp. The blue shifted species were attributed to the aggregates of Badan.

[Trp] (mM)	Lifetime (ns)	SV ratio τ_0/τ
0.0	2.64	1
2.4	2.62	1.008
4.9	2.60	1.015
7.3	2.60	1.018
9.9	2.54	1.039
12.1	2.51	1.050
14.7	2.48	1.065
17.2	2.46	1.072
19.6	2.43	1.088

Table 3.3: Badan fluorescence lifetime quenching by tryptophan in Brij® 58 micellar solution. Values are based on a single-exponential fitting of fluorescence decay measured at 550 nm.

[Trp] (mM)	Lifetimes (ns)		Amplitudes (%)		Average lifetime	SV ratio $\tau_{dec,0}/\tau_{dec}$
	τ_{rise}	τ_{decay}	A_{rise}	A_{decay}		
0.0	0.55	3.56	-10.4	110.4	3.87	1.000
7.9	0.55	3.51	-10.1	110.1	3.81	1.016
15.3	0.52	3.42	-9.75	109.8	3.70	1.048
22.3	0.49	3.38	-9.07	109.1	3.64	1.065
28.8	0.46	3.32	-8.12	108.1	3.55	1.091
35.0	0.44	3.28	-8.17	108.2	3.51	1.104
40.8	0.43	3.25	-7.74	107.7	3.47	1.117
46.4	0.43	3.21	-7.56	107.6	3.42	1.133
51.6	0.46	3.15	-7.69	107.7	3.35	1.156
61.3	0.43	3.11	-7.28	107.3	3.30	1.172
70.0	0.42	3.06	-6.70	106.7	3.24	1.197
85.3	0.38	3.00	-5.40	105.4	3.14	1.232
98.0	0.37	2.97	-4.42	104.4	3.08	1.257
108.9	0.35	2.89	-2.90	102.9	2.96	1.309
118.3	0.35	2.86	-2.70	102.7	2.93	1.323

Table 3.4: Prodan fluorescence lifetime quenching by tryptophan in Brij® 58 micellar solution. Values are based on a double-exponential fitting of fluorescence decay measured at 550 nm.

3.2.4 Discussion

Fluorescence lifetimes of the two investigated Badan-labeled CYP-Trp mutants were significantly shorter than of their His-containing counterparts, indicating that the emissive singlet excited state of Badan is quenched by the proximal Trp residue. To study the Badan-Trp quenching without any possible interfering effects of the protein environment or the heme cofactor, we also investigated Badan (and analogous Prodan) fluorescence quenching by Trp in Brij® 58 micelles. Both species concentrate in the micelles, promoting formation of contact pairs. Indeed, we observed very efficient static quenching attributable to the formation of non-emissive $\pi\pi$ complexes between the aromatic Trp-indole groups and Badan (Prodan) inside micelles. These complexes are moderately stable, with association constants of 14.7 M^{-1} (3.5 M^{-1}) and their excited-state lifetimes are much shorter than the instrument time resolution (below 30 ps). Residual dynamic quenching, which accounts for 20-30% of the total quenching, is attributable to the highly dynamic nature of the micelles that still allows for diffusive encounters.

Quenching of Badan and Prodan fluorescence can occur either by an energy- or electron transfer mechanism. Energy transfer can be ruled out, since population of $*^1$Trp is energetically uphill (and $*^3$Trp is slightly uphill and spin-forbidden). The feasibility of an electron transfer mechanism, i.e., Trp oxidation by excited dyes, can be assessed using electrochemical arguments. Trp is a redox-active amino acid whose indole side chain is oxidized to the corresponding radical cation at rather positive potentials, between +1.02 and +1.21 V vs. normal hydrogen electrode (NHE) [100–103]. The excited-state reduction potential of Prodan and Badan in aprotic media (MeCN) and can be estimated as a sum of the ground-state reduction potential (−1.85 V) and the excited-state energy of 2.5 eV (estimated from fluorescence spectra), giving the value of +0.6 V vs NHE. Both dyes become much stronger excited-state oxidants (+1.6 V) in the presence of water, as the reduced form is stabilized by a very rapid reaction with the solvent. The actual value depends on the water accessibility of the dye molecules (details can be found in Attachment II). It follows that electron-transfer quenching in aprotic media is endergonic by about 0.5 V (taking $E^{o\prime}$(Trp/Trp$^{\bullet+}$) = +1.1 V [100]). In CYPs, Badan is located at the protein surface, partly exposed to water (Figure 3.4). In Brij® 58 micelles, the dye and Trp molecules likely occur in the regions

between the polyether head groups that are intermixed with water [104]. Therefore, it is the aqueous solvation what makes the photoreduction of (dimethylamino)naphthalene dyes by Trp thermodynamically possible because water changes the dye reduction mechanism and upshifts the excited-state reduction potential to roughly +1.6 V. Trp oxidation by electronically excited Badan (Prodan) in the present systems is thus thermodynamically favourable by ≤0.5 V and ET is coupled to a very fast reaction between the solvating water molecules to the reduced dye (presumably proton transfer).

Having established Badan photoreduction by Trp as the most likely quenching mechanism, we turn our attention to the fluorescence decay kinetics of Badan-labeled CYPs. Both CYP102-His and CYP119-His exhibited multiexponential behaviour that probably reflects conformational heterogeneity, together with medium relaxation dynamics in the Badan vicinity [105]. The longest lifetime measured for the His-containing mutants (τ_3, ~3 ns) is longer than that observed in aqueous solutions (1.3-1.4 ns, Prodan)[106] or in Brij micelles (2.64 ns, Table 3.3), indicating that the Badan label is to some extent shielded from the solvent and oriented to disfavour energy transfer to the heme. The two faster components likely arise from conformations where Badan is more exposed and/or quenched by Förster energy transfer to the heme. Indeed, heme cofactors are known to quench fluorescence of (dimethylamino)naphthalene dyes, such as Dansyl [107]. Crystal structures of unlabeled CYP102-Trp (pdb 2IJ2) and CYP102-His (to be published) show that the 5-membered part of the Trp96 indole ring of CYP102-Trp overlaps perfectly with the imidazole ring of the His mutant. The distances and orientations of the heme are also comparable. In both mutants, the Badan-bearing Cys97 is, on average, 6 Å away from the aromatic side chain (His96 or Trp96). The structure also reveals the presence of various rotamers that introduces significant variability in positions and orientations of the Cys97 sulphur atom and, hence, of the attached Badan label. The similarity between the structures of the Trp and His containing mutants supports our conclusion that the fluorescence lifetime decrease on going from CYP102-His to CYP102-Trp is attributable solely to the photoinduced ET between excited Badan and Trp. Presumably, this conclusion remains valid also for CYP119, where only the structure of the His mutant is available (pdb 1IO7).

In particular, replacing the His residue proximal to Badan by Trp caused partial fluorescence quenching, with an average quenching rate constant of about 4×10^8 M⁻

^{1}s^{-1} for both CYP102-Trp and CYP119-Trp (at 288 K). Quenching influences all three fluorescence decay components (Table 3.2). The most pronounced change was observed for the shortest, tens-of-picosecond, component that became much shorter lived and whose relative amplitude strongly increased. This fastest quenching process presumably occurs in a protein conformation where the Trp-indole and Badan make a close contact, resulting in almost complete quenching. The amplitude increase then reflects a change in conformational distribution, whereby close Trp-Badan contact formation is driven by $\pi\pi$ and/or hydrophobic interactions. Quenching of the longest lifetime τ_3 ($k_{q,3}$ = 1×10^8 and 7×10^7 s^{-1} for CYP102 and CYP119, respectively) is too slow for a contact pair. Instead, it probably corresponds to long-range ET from Trp to the excited Badan label.

We conclude that (dimethylamino)naphthalene-based dyes Badan and Prodan can behave as photooxidants whose excited-state reduction potentials vary from about +0.6 V (vs NHE) in polar aprotic media (MeCN) to approximately +1.6 V in water, where reduction is presumably coupled to proton transfer. Fluorescence of these (dimethylamino)naphthalene dyes is quenched by close-lying tryptophan in proteins as well as in micelles. Excited-state ET reactions in Badan-labeled CYPs occur in several kinetics steps whose lifetimes range from tens of picoseconds to about 10 ns, presumably depending on protein conformation as well as the relative orientation of the Badan and indole aromatic groups. The possibility of photoinduced ET must be considered whenever (dimethylamino)naphthalene dyes are used as fluorescence protein labels, as this reaction channel can complicate the interpretation of FRET experiments as well as analyses of solvation dynamics studied by time-resolved fluorescence spectroscopy. On the other hand, as nanosecond Badan fluorescence quenching kinetics are expected to be sensitive to structural and conformational factors, Badan protein labelling could be employed to investigate short-range ($\leq$ 10 Å) intraprotein interactions and conformational changes due to folding or substrate binding.

3.3 Dipolar relaxation dynamics at the active site of an ATPase regulated by membrane lateral pressure

Integral membrane proteins reside in the plasma membranes that surround cells and subcellular organelles. They couple extracellular stimuli to cellular responses and provide molecular pathways of high chemical specificity for the transport of ions across the lipid bilayer. Membrane proteins expose a belt of hydrophobic residues to the interior of lipid bilayer, whereas hydrophilic side chains reach into the intra- and extracellular aqueous phase [108, 109]. The interaction of membrane proteins with lipids forming the bilayer can be highly specific and is often important for full functional and structural integrity of the protein [110]. For example, membrane curvature or lateral pressure might have a significant influence on tuning membrane protein structure in terms of changes in helix orientation or conformation, or changes in helix–helix interactions [111]. Moreover, selective binding between a membrane protein and a certain lipid in a "co-factor-like" fashion may regulate protein function in a very specific way [112]. However, this specificity is less significant in comparison to the collective effect of lipids [113, 114].

Nevertheless, membrane protein function is mainly linked to the protein conformational changes. These changes are particularly large in P-type ATPases, which catalyze ATP-driven ion transport across biological membranes [115, 116]. The sarcoplasmic P_{II}-type Ca^{2+}-ATPase SERCA1a provides a mechanistic paradigm for such ion pumps [117, 118] and the functional role of lipid–protein interactions is revealed by the lipid-dependent efficiency of SERCA1a [119]. Switching between two main structural states (cytosolic E1 state, and extracellular E2 state), the accessibility to ion binding sites of the ATPase necessarily violates the energy-minimized structure of the membrane protein and requires dynamic re-adjustments between the lipids and the protein [120]. P-type ATPases furthermore couple the conformational changes, involving protein-lipid interactions, to ion dehydration and rehydration during transport. Therefore, the degree of hydration and mobility at the non-lipid-exposed internal ion-binding sites in a transmembrane helical bundle plays crucial role in membrane protein function. However, the experimental determination of the lipid-dependent internal hydration of multi-helical membrane proteins has not been attempted to date. In this particular part of this work, we investigated the influence of

membrane lateral pressure on the internal hydration of the copper-transporting ATPase LpCopA from *Legionella pneumophila*. In order to provide near-natural membrane environment, LpCopA was reconstituted in the nanodiscs (NDs), which support native LpCopA activity in a mixed lipid bilayer. Nanodiscs consist of a discoidal lipid bilayer of ~13 nm diameter surrounded by a membrane-scaffolding protein, in our case MSP1E3D1 [94, 95]. On the other hand, detergent micelles reduce lateral pressure, rendering the fully solubilized state of a membrane protein a reference state for minimal lateral pressure [114].

The copper-binding site of LpCopA is provided by the sulfurs of cysteine residues C382 and C384 in (CPC) motif on transmembrane helix four, and the conserved methionine residue of transmembrane segment six of P_{1B}-type ATPases [121–123] (Figure 3.10). We found that the two cysteines are accessible for chemical modification by Badan fluorophore, rendering LpCopA an ideal model for TDFS studies on intramembrane protein hydration at minimal structural and mutational perturbation within the octahelical bundle. Although, several tryptophan residues are present in the octahelical bundle, all the distances between these tryptophans and both sites labelled with Badan are larger than 10Å. Thus, no interfering quenching of Badan by tryptophan was detected.

3.3.1 Experimental

In order to allow specific Badan-labelling of cysteines in the CPC motif, the four additional cysteines in the N-terminal domain of the protein, C18, C42, C56, and C59 were removed, resulting in mutant CM-LpCopA. Moreover, native cysteines in the CPC motif were changed to serines in the mutant CM-LpCopA. The unlabelled system is catalytically active as shown by the Lanzetta ATPase enzyme assay (Attachment III). Two additional mutations were introduced into CM-LpCopA, leaving a single cysteine residue to bind Badan to either C382 (CM-B382) or C384 (CM-B384). Its structural integrity after Badan labeling at C382 and C384 was assessed by circular dichroism, which confirms a stoichiometry of one CM-LpCopA per ND and agrees with a native secondary structure despite the chemical inactivation of the ion-translocating site. The thermal protein stability was not affected by the label either, in line with tertiary structure conservation. Expression, purification, labelling and reconstitution were done by Elisabeth Fischermeier and Ahmed Sayed from Karim
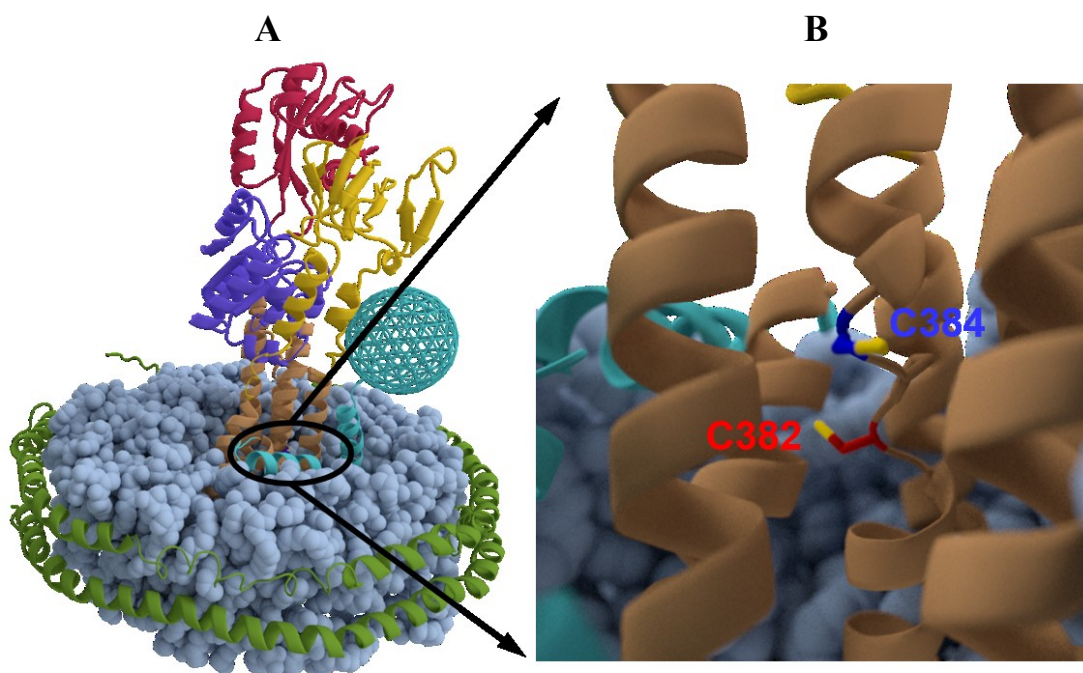
Figure 3.10: A) Schematic representation of LpCopA in a nanodisc. Hypothetic topology of LpCopA in a nanodisc with the amphipathic helix MBb (cyan) aligned running parallel to the lipid bilayer (blue-gray). The cytoplasmic phosphorylation, nucleotide-binding and actuator domains are shown in blue, red, and yellow, respectively. The heavy metal-binding domain (not resolved in the crystal structure) and the helices MA and MB are shown in cyan, other transmembrane segments in light brown. The black circle marks the location of the copper-binding CPC motif. **B)** Close up view of the copper-binding CPC motif comprising C384 (blue) and C382 (red) on helix 4. LpCopA structure from pdb 3RFU and membrane scaffolding protein (green) from pdb 4V6M. Picture courtesy of Philip Gröger, Elisabeth Fischermeier and Karim Fahmy.

Fahmy group at Helmholtz-Zentrum in Dreden. Further details can be found in Attachment III.

TDFS measurements were performed using steady state and TCSPC instrumentation as described in sections 2.1.1 and 2.2.1, respectively. All measurements were performed at 15°C. TDFS data were evaluated as described in section 2.4.1 and time zero estimation were performed as described in section 2.4.2.

3.3.2   TDFS measurements of Badan labeled CM-LpCopA mutants

The effect of membrane lateral pressure on site-specific hydration was quantified by comparing total amount of the Stokes shift (Δv_t) and average relaxation time (τ_R) values of the detergent-solvated state of CM-B382 and CM-B384 with the values obtained from the measurements of the same LpCopA mutants reconstituted into NDs (Table 3.5). In the latter, membrane lateral pressure is comparable to that of plasma

Labeled cysteine	ATPase state	time zero [cm^{-1}]	$\Delta\nu_t$ [cm^{-1}]	τ_R [ns]
CM-B382	nanodiscs	23,950	3200	1.38
	micelles	23,800	4300	1.14
CM-B384	nanodiscs	24,150	3600	1.35
	micelles	23,750	3650	1.94

Table 3.5: The TDFS parameters with time zero estimation for single site-labelled ATPases.

membranes [99, 100], which increases inter-helical contacts in the protein and reduces intra-protein dynamics [101]. In the micellar state, the $\Delta\nu_t$ values of the C382 mutant is close to the $\Delta\nu_t$ value obtained for Badan analog Prodan in lipid vesicles, where small part of the dye ensemble is located in the bulk water (4100 cm^{-1} [33, 34]). Average τ_R in bulk water is about 0.3 ps [77]. On the other hand, about 50% of the time-dependent shift can be detected by the 30 ps time-resolution of our experiments (Figure 3.11A). This finding indicates that the C382 position is fully hydrated, but the mobility is governed by both bulk water and hydrated protein segments. On the contrary, the C384 mutants show a much smaller $\Delta\nu_t$ value and a slower overall relaxation response (Figure 3.11B). This finding suggests that the solvent relaxation is dominated by hydrated protein segmental motions occurring on the ps and ns timescale.

The concerted change of both variables at the two cysteine residues in detergent-solvated state indicates that a higher amount of inter-helical water near C382 in the micellar state, as compared to C384, causes the local "softening" of the intra-membrane protein structure, thereby allowing more efficient solvent relaxation. A similar correlation of low hydration with low mobility has been demonstrated for active site cavities in soluble proteins [37, 102].

On the other hand, lipid bilayer reduced the degree of hydration around C382 from a bulk water-like situation to an environment characterized by hydrated protein segments, reducing the total TDFS by 25% (decrease of $\Delta\nu_t$ = -1100 cm^{-1}, Table 3.5). Concomitantly, the average relaxation time increased by 20% (increase of τ_R = + 0.24 ns), demonstrating reduced local dynamics. TDFS data confirm the expectation that the reduced intra-membrane protein dynamics by the lipidic constrains leads to reduced hydration and mobility in the protein interior. In contrast to the hydration around C382, the amount of hydration in the vicinity of C384 decreased by only 1–2% (decrease of $\Delta\nu_t$ = -50 cm^{-1}) after reconstitution into NDs (Figure 3.11B). This

indicates that already in the micellar situation the Badan environment are dominated by hydrated protein segments and not bulk water. However, the τ_R value for the label at C384 decreased (decrease of τ_R = - 0.59 ns), indicating faster segmental motions at that position when the protein is imbedded in the membrane. Despite the physical equivalence of the hydrated environments of the Badan at C382 and C384 in the membrane-inserted state, the lipidic phase has inverted the hydration gradient across the CPC motif in comparison to the micellar state. The strong modulation of the water pocket around C382 and the transition from mobile to less mobile internal hydrated protein segments around C384 was not expected from the crystal structure and MD calculations.
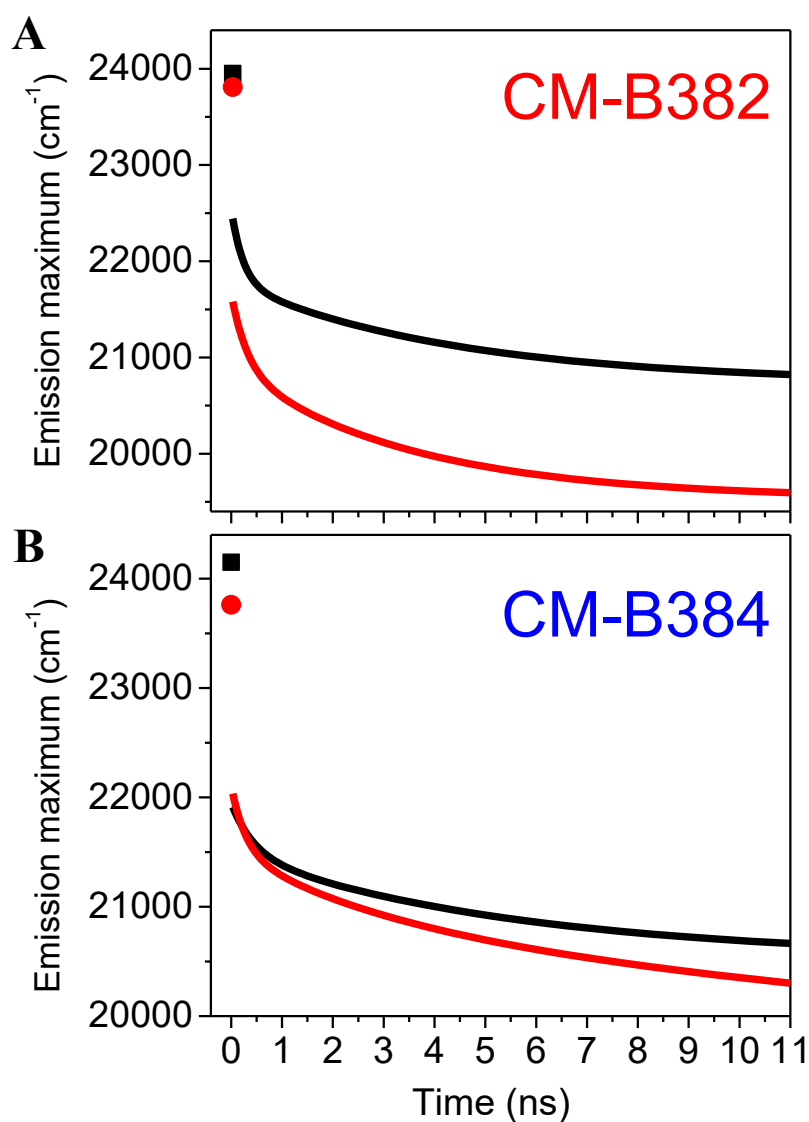

Figure 3.11: TDFS of Badan bound to C382 **(A)** and C384 **(B)** residue of the ATPase CM-LpCopA in detergent solution (red) and NDs (black). The calculated time-zero frequencies are displayed as red (detergent) and black (NDs) circles.

3.3.3 Discussion

The data reveal distinct local responses of internal hydration of LpCopA to membrane lateral pressure despite the close α-carbon positions of the labeled sites. We estimate the maximum center to center distance between the regions sampled by Badan in the two singly labeled constructs to be 15 Å. The microenvironment of the buried C382 changes dramatically upon membrane insertion, which indicates hydrated region of high flexibility, where both micropolarity and microviscosity are tightly controlled by membrane lateral pressure. On the other hand, the more cytoplasmic C384 is less influenced by the membrane insertion which indicates restricted hydration (micropolarity) even in the absence of membrane lateral pressure. Nevertheless, the mobility around C384 is still sensitive to lipid protein interactions since it unexpectedly increased by membrane lateral pressure. The degree to which the polarity around the two cysteine residues depends on lipid-induced helical packing contradicts an intuitive understanding based on the topology of the two residues: C384 resides at the interface of the aqueous and the membrane phase, where a more variable hydration would be expected, whereas one would expect a more stable hydrophobic environment for the more membrane embedded C382, regardless of the lipidic environment.

The dynamic hydration pattern around C382, revealed by TDFS, may enable functional transitions between a hydrated ion-accepting state and a structurally more constrained dehydrated state, in which water coordination becomes replaced by protein side chain coordination during ion transport. Thus, this site may act as flexible conformational "switch" facilitating the copper-ion re-solvation and release to the extracellular side of the membrane. Importantly, the cyclic nature of the ATPase function suggests that membrane lateral pressure can provide a restoring force that dehydrates the C382 environment during the catalytic cycle, when the ion is released to the extracellular opening.

Surprisingly, C384 resides in a more stable hydrophobic environment and we attributed the low water mobility around this residue to a rigid inter-helical H-boded (structural) water network at low membrane later pressure. The network disassembles upon closer helical packing in the presence of membrane lateral pressure in NDs. Moreover, the environment around C384 might serve as a "hydrophobic gate" where the hydration shell of the copper-ion is partially stripped off to enable its binding to the protein and its back-diffusion to the cytoplasm is prevented.

In summary, the data show that TDFS can resolve distinct patterns of intra-membrane protein hydration and dynamics, which are shaped by membrane lateral pressure. Importantly, the cyclic nature of the ATPase function implies that membrane lateral pressure may provide a restoring force that reverts transient hydration-promoting conformational changes which are presumably required for ion translocation across membranes in general [124, 125].

3.4 Heavy atom effects on excited-state dynamics of iodinated metallocorroles

Corroles are synthetic tetrapyrrolic macrocycles similar to the large group of naturally occurring porphyrins. However, the first synthesis of corrole was reported in 1964, the chemistry of corroles has remained largely undeveloped since 1999. In the following decade, corroles have rapidly expanded and they have found the place in many interesting applications and promising possibilities.

Corroles exhibit very rich photophysical and redox behaviour that is tunable and controllable by varying substituents on the corrole periphery, as well as the central metal atom (metal complexes) [126, 127]. Corroles are intensively studied for their catalytic and, namely, spectroscopic properties that are significant with nanosecond exited singlet states lifetimes and tenth or hundreds of microsecond triplet lifetimes [128, 129]. Corroles and their metal complexes are excellent agents for photodynamic therapy, cancer-targeted imaging [126, 130], and tumor elimination [131–134], as well as solar-cell [135, 136] and singlet-oxygen photosensitizers [137, 138]. They also exhibit pronounced 2-photon absorption and high nonlinear optical coefficients, opening interesting possibilities for optoelectronic applications [139]. Moreover, corroles spontaneously form tightly bound conjugates with proteins (human serum albumin [140], and transferrin [141]), which opens the possibilities for dynamical protein studies and many medicine-oriented applications. Such a wide variety of spectroscopic applications stem from the diverse and tunable corrole excited-state properties, which emphasizes the need of addressing fundamental questions about mechanisms of excited-state relaxation.

Absorption and emission spectral patterns of corroles are similar to those of porphyrins, however, they are stronger fluorophores than porphyrins. The Soret band occurs between 400 and 450 nm and, in some cases, is split in two because of the lower symmetry of the corrole structure [142]. The Q-type bands occurs around 500-650 nm [143], and quantum yield of the Q fluorescence increases from 0.1-0.2 in free-base corroles [142, 144, 145] to 0.3-0.5 and 0.76 in their Ga and Al complexes, respectively [146]. Very weak fluorescence from the higher-lying Soret state(s) has been detected in free-base corroles [128] and their Ga and Al complexes, but the Soret excited-state

lifetimes (140-550 fs) are shorter than for porphyrins. The Q states are ultimately populated after Soret excitation with a near-unity efficiency [147].

Population of the lowest Q triplet state by intersystem crossing (ISC, sections 1.3.4 and 1.3.5) is a crucial process, essential for singlet-oxygen sensitization and photodynamic therapy, as well as electroluminescence and triplet-triplet annihilation up-conversion [148]. Moreover, agents that emit beyond 700 nm with microsecond lifetime can help to circumvent the most common obstacles to efficient biological imaging: tissue absorbance and intrinsic fluorescence.

The ISC rate and yield sensitively depend on the corrole structure, manifesting the "heavy atom effect" [1, 149]. For free-base corroles, the ISC rate depends, for example, on the extent of fluorination of the *meso*-phenyl groups [128], or upon complexation with main-group elements Ga^{III} and Al^{III} [147], as well as P^{V} and Ge^{IV} [150]. The (near) absence of fluorescence in emission spectra of phosphorescent Ir^{III} and Au^{III} complexes point to ultrafast ISC [151, 152]. Iodination of the pyrrole rings produces corrole complexes bearing zero, three, or four β-iodine atoms (Figure 3.12), further abbreviated 0-M, 3-M, and 4-M, respectively, (M = Al, Ga) [153, 154]. The fluorescence yield is strongly quenched, for example, from 0.76 in 0-Al to 0.0034 in 4-Al, while 192-373 µs phosphorescence emerges, thus indicative of fast and efficient triplet population. Besides, iodinated corroles display delayed thermal fluorescence (section 1.3.5) [154].

Corroles present excellent systems for quantitative investigations of the intramolecular "heavy atom effect". Such studies are particularly relevant from a fundamental perspective, as they reveal ISC timescales and their structural
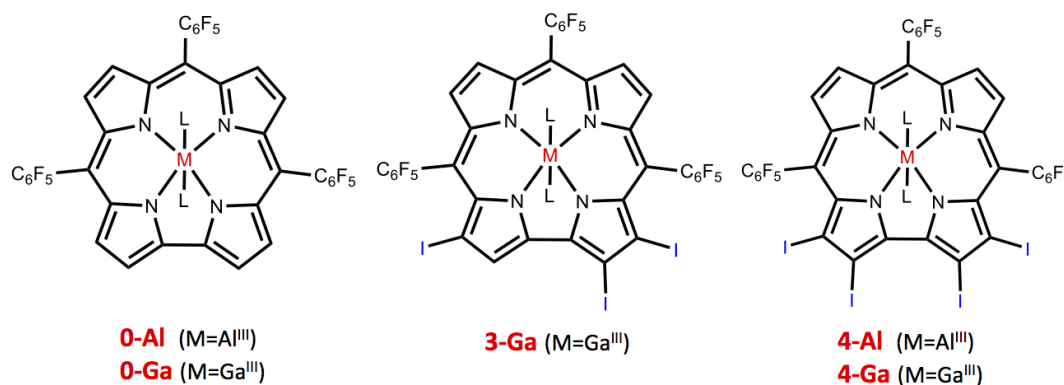

Figure 3.12: Schematic structures of investigated complexes of corroles (L = pyridine).

dependence. We have now seized the opportunity offered by the sequential iodination of Al and Ga corroles for investigating their photophysics using spectrally broad-band femtosecond time-resolved fluorescence up-conversion in combination with quantum chemical calculations that include spin-orbit (SO) coupling explicitly.

3.4.1   Experimental

Corrole complexes were synthesized and characterized by literature methods by Jenya Vestfrid from Zeev Gross group at Technion in Haifa [153, 154]. Samples for time-resolved spectroscopic studies were obtained by dissolving 20-40 mg in 80 mL of toluene containing 5% of pyridine resulting in approx. 0.1-1 mM concentration. 5% pyridine in toluene mixture were chosen as a solvent to minimize dissociation of axial pyridine ligands. All measurements were performed at room temperature under argon atmosphere. Spectroscopic-quality anhydrous solvents were used as obtained from Sigma-Aldrich.

Steady-state absorption and emission measurements have been carried out in 0.1 mm quartz cuvettes using ~ 1mM sample concentrations, to match the concentrations used in up-conversion experiments. Up-conversion measurements and analysis were done with the great help from Enrico Pomarico from Majed Chergui lab. All instrumentation used in this part of the work, UV-VIS and fluorescence spectrometers, TCSPC and FlUC, are described in sections 2.1.1, 2.2.1 and 2.3.1, respectively.

Quantum chemical calculations were performed by Stanislav Záliš from J. Heyrovský Institute in Prague and only the main outcome of these calculations is discussed in the following text. The details can be found in Attachment IV.

3.4.2   Steady-state absorption and emission spectroscopy

All examined corroles exhibit an intense Soret absorption band between 400 nm and 450 nm and a weaker Q band in the 550–650 nm range (Figure 3.13) [146, 153, 154]. Small differences (peak maxima shifts, occasional band splitting) between the present spectra and those published before are attributable to the 5% pyridine addition in the present case that maintains the 6-coordinated bis-pyridine adducts as the predominant species in the solution [154]. All complexes exhibit steady-state emission
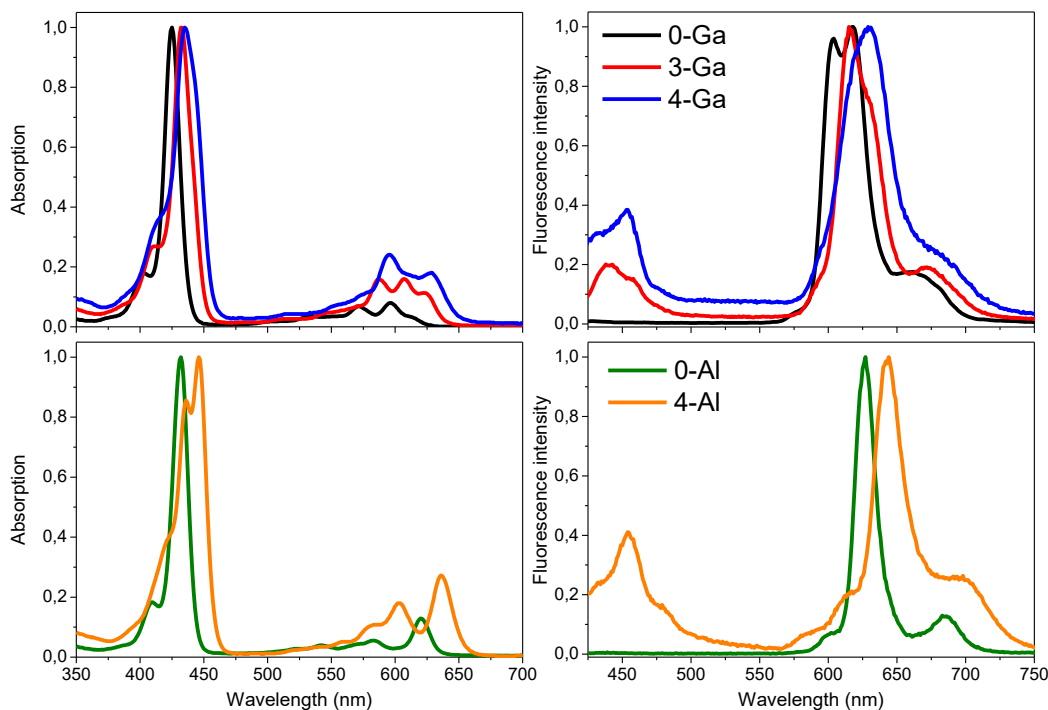
Figure 3.13: Comparison of normalized steady-state absorption (left) and emission spectra (right) of investigated complexes of corroles. Spectra were obtained upon 400 nm excitation.

in 420-480 nm and 500-650 nm ranges due the radiative decay of the Soret and Q excited states, respectively (Figure 3.13). Phosphorescence reported for the iodinated derivatives above 800 nm was not studied in this work [153, 154].

Quantum chemical calculations for 0-Ga and 0-Al well reproduced the experimental absorption spectra, including the observed red shift and increase of the relative Q-band intensity upon iodination (Attachment IV). Calculations revealed a dense manifold of states occurring between the Soret and Q states of the iodinated complexes. These states involve excitations from lower-lying iodine-localized molecular orbitals (MOs) to the LUMO (Lowest Unoccupied Molecular Orbital) and possess an iodine→corrole charge transfer (CT) character. The corresponding transitions have oscillator strengths in the range from 10^{-4} to 5×10^{-3}, thus they are too weak to contribute to the absorption spectra. Whereas transitions to the predominantly singlet states have oscillator strengths in the range 0.1-0.9. Quantum chemical calculations revealed no CT states for 0-Ga and 0-Al.

In order to prove the Soret origin of the 420-480 nm spectral feature, emission spectra were measured at several excitation wavelengths in the blue side of the Soret absorption (Figure 3.14). The spectra clearly distinguish the fluorescence band, which
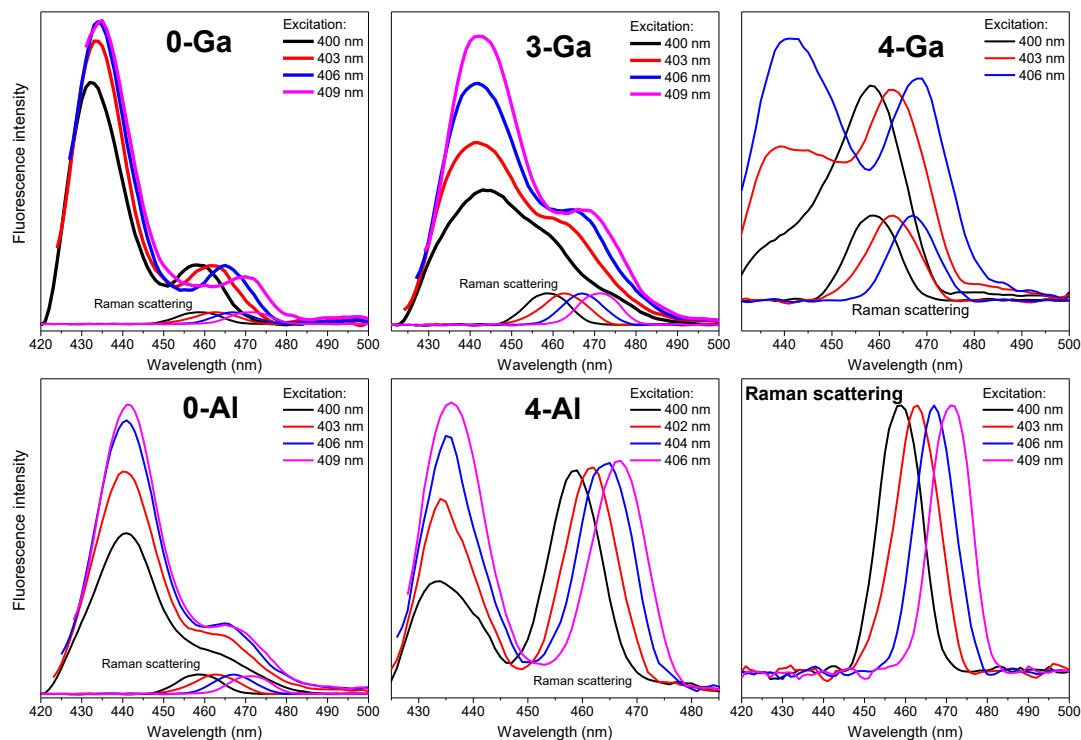
Figure 3.14: Steady-state emission spectra of investigated complexes of corroles in the region of the Soret emission. Bottom-right: pure Raman scattering. All measurements in 5% pyridine in toluene except 4-Al (pure toluene).

does not shift with the excitation wavelength while its intensity increases as the excitation wavelength moves deeper into the Soret absorption band, from the Raman solvent peak, whose maximum shifts with the excitation wavelength while its intensity stays approximately constant. Relative to the Raman peak, the Soret emission of 0-Al and 0-Ga is much stronger than of the iodinated derivatives, indicating higher quantum yield. The Soret emission of 0-Al and 0-Ga was described before [147]. It is not seen in the graphs, because the Q emission of 0-Al,Ga (to which the spectra are normalized) is very strong (Figure 3.13 and Figure 3.14). In all cases, the Soret emission shows a weak tail toward lower energies with a shoulder at 480-500 nm, i.e. overlapping with the solvent Raman signal. This low-energy tail is attributable to radiative transitions to higher ground-state vibrational level(s). Structured Q fluorescence spectra are approximately mirror images of the corresponding Q absorption features. The presence of 5% pyridine in the toluene solvent causes small red shifts relative to the previously reported spectra [146, 147, 153, 154].

3.4.3 Time-resolved fluorescence

Decay kinetics of the Q emission of 0-Al and 0-Ga was investigated by TCSPC. In accordance with previous data from benzene/pyridine mixtures [146], a biexponential decay kinetics was observed with principal lifetimes of 5.6 and 2.9 ns, respectively. The minor 0.80 (0-Al) and 0.69 ns (0-Ga) components were related to the kinetics of pyridine dissociation from the excited state, as was discussed in detail in Kowalska et al [146]. Emission decay of all iodinated complexes was too fast to be measured by TCSPC. Ultrafast excited state dynamics were therefore studied by fluorescence up-conversion with a femtosecond time resolution. Soret excitation at 400 nm together with spectrally broadband detection made it possible observing simultaneously the Soret decay, Q rise and subsequent decay, as well as accompanying relaxation processes.

Figure 3.15 shows the time-wavelength (t-λ) plots of the fs-resolved fluorescence, together with transient spectra at selected time delays. In all cases the signal at and shortly after time-zero extends over the whole spectral range and exhibits a strong feature below 500 nm, which corresponds to the Soret emission. The fluorescence decay in the Soret part of the spectrum occurs within the first picosecond and is accompanied by a concomitant signal rise at longer wavelengths (600-650 nm) that belongs to the Q emission. For all the iodinated complexes the Q feature is clearly observable at the earliest times after excitation (see the spectra recorded at t = 0, Figure 3.15) and then growths further within the first 500 fs. Initially, until approx. 1 ps, the Q-emission extends to shorter wavelengths and merges with the tailing Soret band. For 0-Al,Ga, the Q feature is absent at t = 0 and growths in the first 20 ps, while the Soret emission and its long-wavelength tail decays. At longer time delays, the 2D maps shows that the Q emission is very long-lived in the case of 0-Al and 0-Ga, whereas it is completely quenched in approx. 50 ps in the iodinated compounds.

Sample	τ_1 [fs]	τ_2 [ps]	τ_3 [ps]
0-Al	540 ± 20	16 ± 2	5600 ± 200[a]
0-Ga	320 ± 20	14 ± 1	2900 ± 300[a]
3-Ga	180 ± 6	1.4 ± 0.1	24.1 ± 0.5
4-Ga	70 ± 10	0.36 ± 0.03	14.9 ± 0.6
4-Al	185 ± 5	1.4 ± 0.2	23.6 ± 0.6

[a] Determined by TCSPC

Table 3.6: Fluorescence lifetimes determined by SVD analysis of the t-λ time-resolved fluorescence up-conversion data of investigated complexes of corroles.

Kinetics analysis of the fluorescence time evolution was performed by Singular Value Decomposition (SVD) [16], from which three lifetimes and corresponding Decay Associated Spectra (DAS) were extracted (Table 3.6). SVD results are supported by global fitting whereby a triexponential kinetics model was applied to the
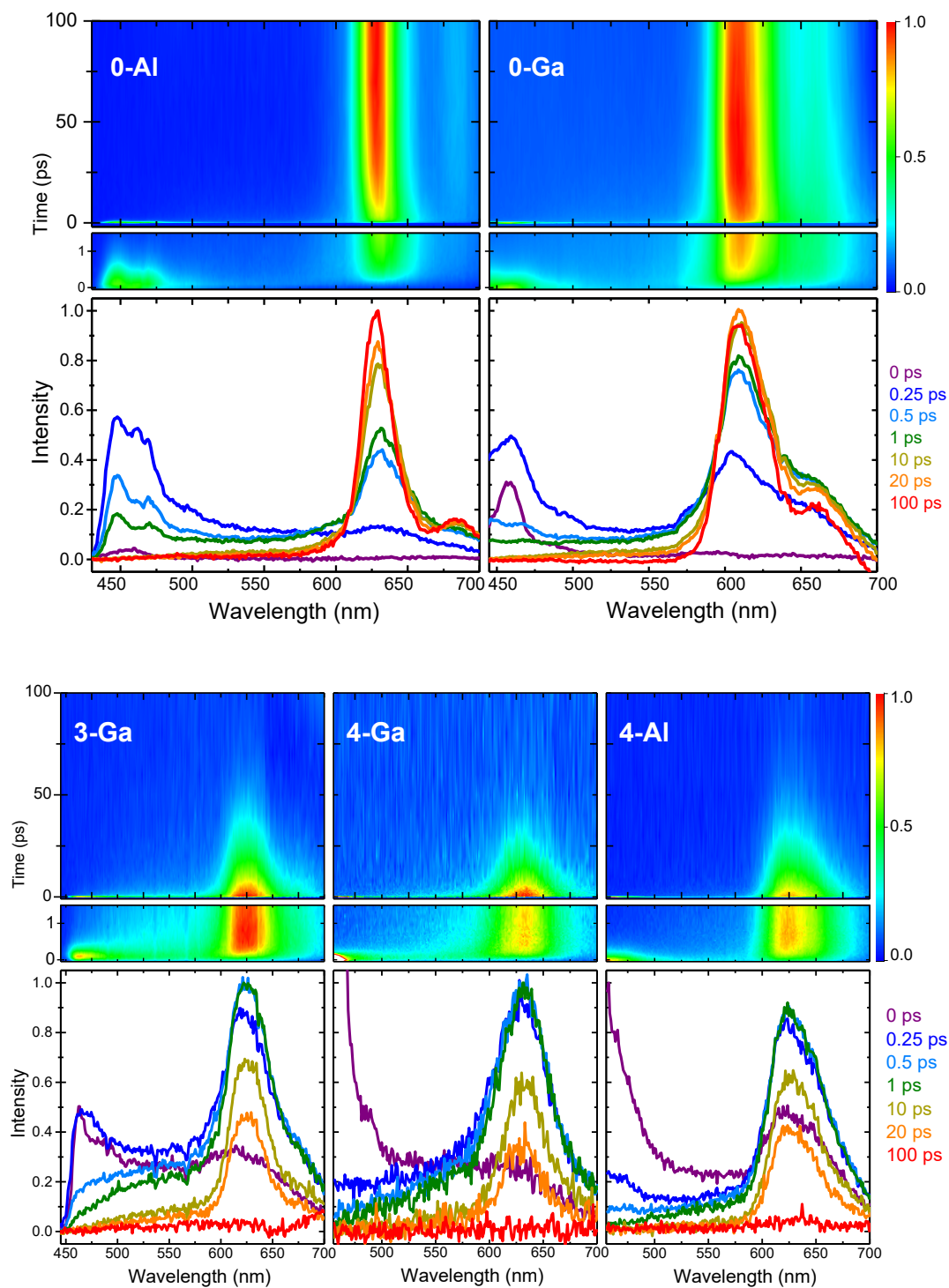

Figure 3.15: The fluorescence t-λ 2D plots and selected time-resolved spectra of investigated complexes of corroles. The lower 2D plot shows the early time evolution up to 1.5 ps. The upper panel covers the time range up to 100 ps.

kinetics traces measured at 10-15 wavelengths across the spectra (Figure 3.16 and Figure 3.17).

DAS$_1$ corresponding to the first subpicosecond step (τ_1) is positive in the Soret emission region and negative in the range of the Q emission, reflecting their respective decay and rise. The τ_1 time constant thus corresponds to the Soret-state(s) lifetime that is equal to the Q-state rise-time. For the iodinated complexes, DAS$_1$ is also positive in the region between the Soret and Q features (up to ~570 nm), showing that the broad emission background partly decays on the τ_1 timescale.

DAS$_2$ resembles in all cases the second derivative of the Q emission band, manifesting its narrowing: decay in the wings accompanied by rise of the central
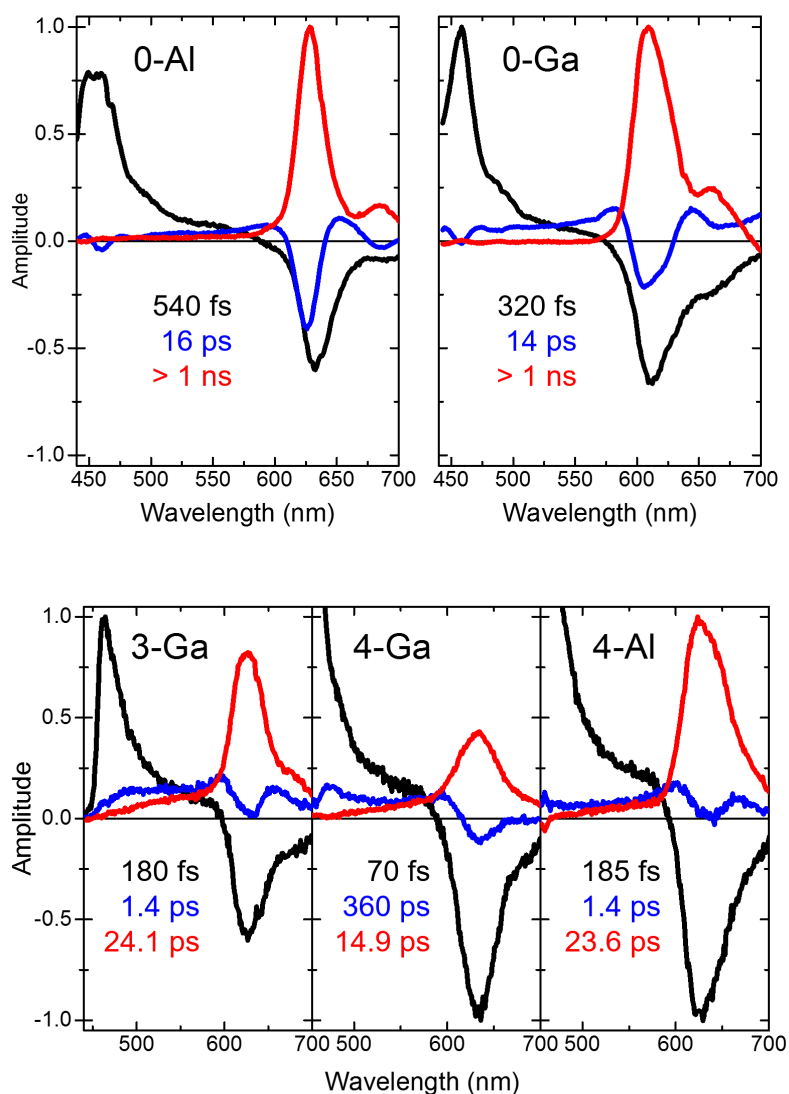

Figure 3.16: Decay associated spectra (DAS) obtained by SVD analysis of the t-λ time-resolved fluorescence up-conversion data of investigated complexes of corroles. Lifetimes corresponding to the DAS$_1$ (black) and DAS$_2$ (blue) and DAS$_3$ (red) spectra are specified in the insets.
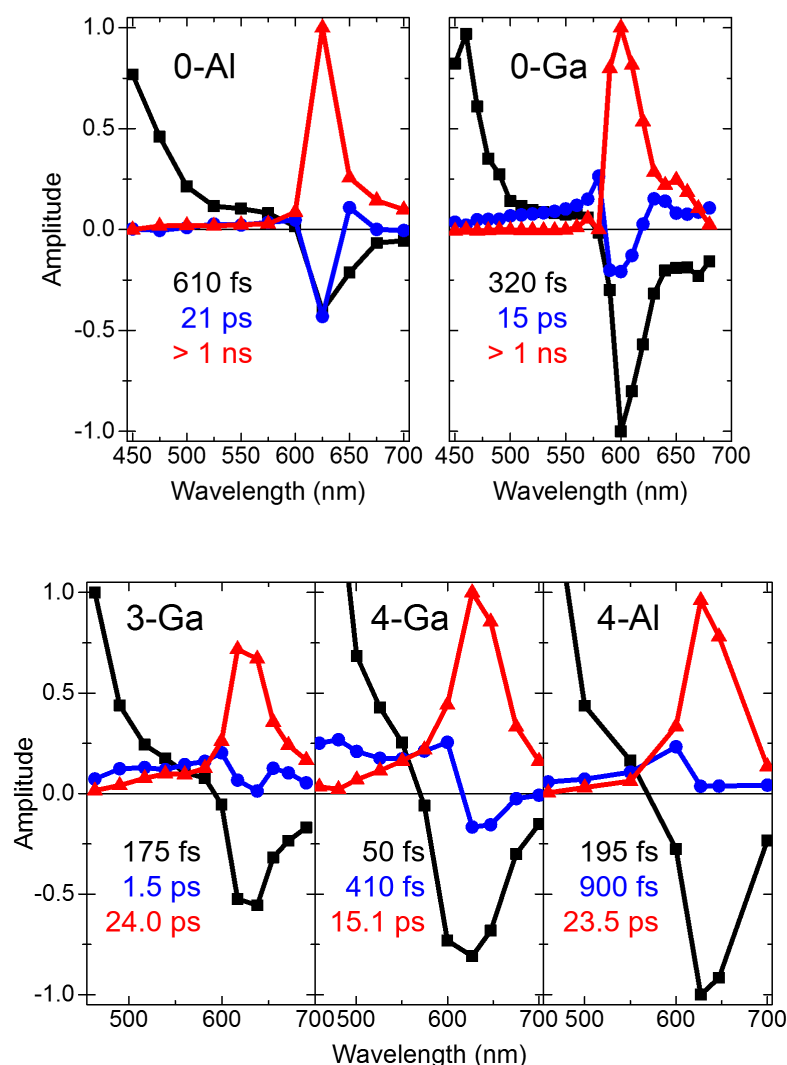
Figure 3.17: Results of global triexponential fitting of 10-15 fluorescence kinetics traces of investigated complexes of corroles. The plots show dependences of the corresponding preexponential factors on the emission wavelength. Lifetimes are specified in the insets. The global fitting closely matches the SVD analysis.

region around the maximum. Hence, the second kinetics step (τ_2) is attributable to vibrational cooling of the Q singlet state(s). For 3-Ga and 4-Ga (less for 4-Al and 0-Ga), the positive part of DAS2 extends to shorter wavelengths (up to 480-500 nm) indicating that the broad emission background decays with the same kinetics.

DAS3 is positive and has the shape of the Q emission band. The respective kinetics thus corresponds to the decay of the lowest Q singlet state with a τ_3 lifetime.

All three time constants depend on the number of iodine atoms (Figure 3.18). The Soret excited state decay and the relaxation rate constants strongly increase from 3 to 4 iodine atoms, whereas the Q excited state decay lifetime displays a nearly linear dependence along the whole series.
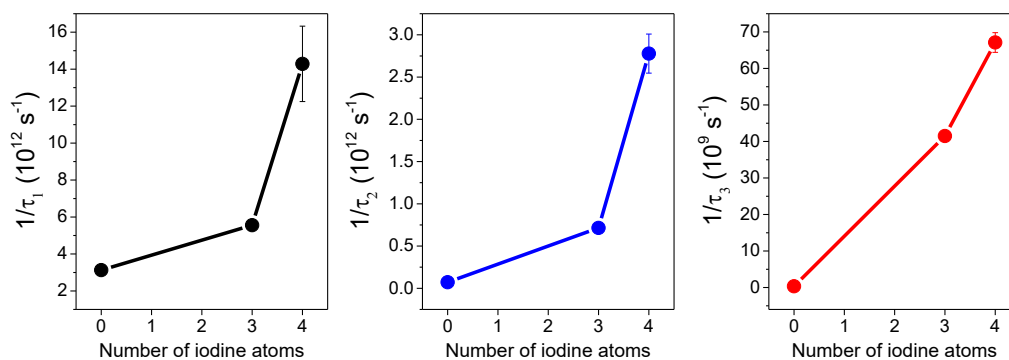
Figure 3.18: Photophysical rate constants as a function of the number of iodine atoms in the Ga-based corroles.

3.4.4   Discussion

Excited-state dynamics of iodine-free as well as iodinated Al and Ga corrole complexes can be described in terms of two radiative (Soret and Q emissions) and three nonradiative decay pathways, whose mechanisms, rates and yields sensitively depend on the degree of iodination and, to a lesser extent, on the nature of the metal atom, Al vs. Ga.

Near-UV excitation populates the Soret pair of singlet excited states. This is manifested by the instantaneous appearance of the fluorescence feature at about 450 nm, accompanied by a broad weak emission signal that extends to lower energies. For the iodinated complexes, this broad signal initially looks like a combination of a long-wavelength tail of the Soret fluorescence overlapping with hot Q emission from higher vibronic levels of the higher Q state, further broadened and upshifted by vibrational energy redistribution (IVR) into low-frequency/large amplitude modes. In addition, a weak Q emission band at ~630 nm appears "instantaneously" after excitation. It follows that the Franck-Condon excited Soret states are strongly coupled with higher Q levels and part of the excitation energy is redistributed among Q vibronic/vibrational levels within the experimental time resolution, concomitantly with relaxation of the Soret states. Similar ultrafast (≤10 fs) energy redistribution and relaxation from higher excited states has been observed in transition metal complexes as well as organic chromophores [16, 155, 156].

Soret states of non-iodinated as well as iodinated complexes undergo nonradiative internal conversion (IC) to the Q states, which is testified by simultaneous decay and rise of the Soret and Q emission signals, respectively, with a τ_1 time constant. The τ_1

values of 0-Al (540 fs) and 0-Ga (320 fs) are very close to those reported earlier for 5-coordinated mono-pyridine adducts in benzene (520±30, 280±30 fs, respectively) [147]. The Soret→Q conversion accelerates upon iodination to 180 fs (3-Ga), 70 fs (4-Ga), and 185 fs (4-Al). This is attributable to the manifold of CT excited states introduced between Soret and Q states by iodination as revealed by quantum chemical calculations. These states provide an energy relaxation cascade from the Soret states to various vibronic levels of the two Q states. The faster IC in 4-Ga relative to 3-Ga is relatable to the higher density of the cascade states in 4-Ga. There are no intervening electronic states in iodine-free complexes and the IC has to take place into high vibrational levels of the Q states.

The τ_2 kinetics correspond to vibrational cooling as is indicated by narrowing of the Q-emission band. For 4-Ga, 3-Ga and (less) 4-Al and 0-Ga, the concomitant decay of the residual broad emission background indicates that the τ_2 relaxation step also involves relaxation of higher vibronic levels of hot Q states. In 0-Al (and, to some extent also 0-Ga and 4-Al), the latter process was mostly completed in the previous step (on the τ_1 timescale), concomitantly with the Soret→Q internal conversion. The τ_2 values are approx. 10-times shorter in the iodinated complexes than in 0-Al and 0-Ga, attributable to the presence of intermediate states, higher density of vibrational levels in the energetically relevant region (due to much higher mass of iodine than hydrogen), and better coupling with solvent modes owing to the dipolar character of the iodinated molecules and solvation of polarizable iodine atoms. The 4-fold acceleration of the relaxation step from 3-Ga to 4-Ga could be attributed to higher vibrational state density in the latter complex.

The third kinetics component τ_3 is due to the decay of the Q singlet excited states to the corresponding lowest triplet state by intersystem crossing (k_{ISC}), as well as to the ground state: $\tau_3 = 1/(k_r + k_{nr}^0 + k_{ISC})$. The rate constants of the radiative (k_r) and nonradiative (k_{nr}^0) decay to the ground state are expected to be only little dependent on the number of iodine atoms. For 0-Ga, values of the nonradiative decay rate constant ($k_{nr}^0 + k_{ISC}$) and the triplet formation quantum yield ($k_{ISC}/(k_{nr}^0 + k_{ISC})$) were both determined [146, 157], providing the k_{ISC} value of 2.34×10^8 s^{-1} [157]. In the absence of the triplet quantum yield value of 0-Al, the nonradiative decay rate constant of the lowest Q singlet state (3.64×10^7 s^{-1}) is regarded as the k_{ISC} upper limit. Strong fluorescence quenching and lifetime shortening occurs in the iodinated corrole

complexes [153, 154], indicating that ISC is the prevailing decay process of the Q singlet state(s), so that the Q singlet lifetime can be expressed as $1/k_{ISC}$.

The ISC rate increases with increasing number of iodine atoms and with up to 200-fold acceleration of the Q singlet→triplet it is the biggest iodination effect observed (Table 3.6). The magnitude of the "heavy atom effect" correlates with the singlet-triplet mixing induced by spin-orbit (SO) coupling. Qualitatively, both the SO coupling strength and ISC rate can be correlated with the iodine participation in the relevant molecular orbitals. Importantly, the quantum mechanical calculations showed the importance of SO coupling of the lowest Q singlet with higher-lying CT triplets introduced by iodination. The latter is not available in iodine-free complexes, and it is a newly recognized factor that affects not only ISC but the whole excited-state dynamics.

To sum up, peripheral iodination of Ga and Al corrole complexes facilitates all their nonradiative excited-state decay processes: Soret→Q internal conversion, vibrational and electronic relaxation of the two Q singlet states, and intersystem crossing to the lowest Q triplet state. These photophysical "heavy-atom effects" are attributable to the profound changes of the electronic structure upon iodination.

3.5 Interaction of antimicrobial peptides magainin 2 and PGLa in membranes studied by FCS

Antimicrobial peptides (AMPs) are evolutionary ancient protection against intruding microorganisms (Gram-positive or Gram-negative bacteria, fungi and even enveloped viruses), that are part of the innate immune response of practically all types of organisms [158, 159]. Despite of the large variability, AMPs share some common characteristics in the physicochemical properties, mainly the net positive charge and amphiphilic character. Although, AMPs are evolutionary old weapons, they have been proposed as a potential source of new strategies in the never ending fight with pathogens [160–165]. Unlike conventional antibiotics, they predominantly act without specific receptors and directly disrupt bacterial membranes [161, 162, 166]. This fact makes bacterial resistance almost improbable, since substantial modification of the lipid composition could affect the cell's vital functions. Moreover, degradation by proteases is problematic as most AMPs lack recognition sites for proteases and multi-cellular organisms under attack of bacteria usually defend themselves with a number of AMPs of different structural classes [159, 164].

The exact molecular mechanism by which the AMPs kill bacteria is still under investigations, however, several mechanistic models of the peptide-lipid interaction have been suggested [161, 163, 167, 168]. Overall, the high affinity of AMPs for lipid bilayers is attributed to their cationic amphiphilic structure [162, 164]. AMPs target fundamental differences in the design of the membranes of microbes and multicellular organisms. While the outermost leaflet of a bacterial cell membrane is populated by negatively charged phospholipids, e.g. phosphatidylglycerol (PG), cardiolipin and phosphatidylethanolamine (PE), the outer leaflet of eukaryote membranes exposes mostly neutral lipids (phosphatidylcholine and sphingomyelin). This results in a lower affinity of these cationic peptides towards host cells as compared to bacteria, thus toxicity for multi-cellular organisms is low.

An intriguing property of some AMPs is the synergistic effect, where the activity of the two peptides is substantially higher in a mixture compared to the sum of the activities of the individual agents [166, 169–172]. PGLa and magainin 2 (Mag2) is a well-studied example of a synergistic pair. Both peptides can be found in the skin of the African clawed frog *Xenopus laevis* and represent some of the first antimicrobial

peptides discovered. In addition to their antibacterial properties [173], it has been reported that PGLa and Mag2 show anticancer [174], antiviral [175], and antifungal activity [162, 176]. The antimicrobial activity of these two AMPs is generally attributed to the formation of stable pores in membranes. The mode of peptide-lipid interaction depends on the peptide sequence, three-dimensional structure (distribution of hydrophilic and hydrophobic amino acids), the peptide concentration and the physicochemical properties of the membrane (charge or curvature), which together establish a delicate balance of interactions [161, 165, 167].

In the case of the mixture of PGLa and Mag2, the maximum of membrane permeabilization is reached at a 1:1 molar ratio, which indicates that the two peptides may form a 1:1 heterodimeric complex that creates stable pores in the membrane [171]. Despite a significant effort that has been dedicated to determine the orientation of incorporated AMPs, mainly by solid-state NMR on isotope labelled peptides [158, 166, 170, 171, 177, 178], and demonstration of the synergic activity between PGLa and Mag2 [169, 179, 180], there are only a few works that address the composition of the PGLa-Mag2 complex and its creation [181].

In this part of the work, we address the question whether PGLa and Mag2 really constitute heterodimers or even heteromultimers within the membrane by the FCS method. The labelled and unlabelled PGLa and Mag2 peptides were prepared for the auto- and cross-correlation measurements. Cross-correlation measurements address mainly the question about the forming of heteromultimers within the membrane, while simple correlation measurements shed light on the intriguing cooperative incorporation of PGLa and Mag2 into the membrane. The investigations were performed within the POPE/POPG (2:1) lipid bilayer in order to mimic the bacterial membrane [182].

3.5.1   Experimental

Two antimicrobial peptides from magainin family (Mag2 and PGLa) were provided by the group of Burkhard Bechinger in Strasbourg. There were prepared two samples from each peptide, one labelled and one unlabelled, resulting in four samples in total. Bodipy-like FluoProbesFL SE (emission max. 510 nm) and BODIPY® (emission max. 665 nm) were used for labelling PGLa (PGLa-g) and Mag2 (Mag2-r), respectively. Mag-r and PGLa-g are considered 100% labelled.

1-palmitoyl-2-oleoyl-*sn*-glycero-3-phosphoethanolamine (POPE) and 1-palmitoyl-2-oleoyl-*sn*-glycero-3-phosphoglycerol (POPG) were obtained from Avanti Polar Lipids, Inc. POPE and POPG (2:1) were mixed in 1 ml chloroform (approx. 0.28 mg lipids /ml) in order to prepare Giant Unilamellar Vesicles (GUVs) base on the procedure described by Akashi et al. [183]. The solution was dried with a rotary evaporated to form a lipid film and then kept under vacuum (6 h) to eliminate traces of the solvent. The dried film was hydrated with 1mL of pre-warmed buffer (10 mM Tris, 100 mM NaCl, 0.1 M sucrose, pH=7.1) that had been purged with nitrogen. The tube was then sealed and incubated at 37°C overnight. The resulting suspension of liposomes was gently vortexed prior to use. Lipid mixtures contained 2 mol % of biotinyl Cap PE necessary for attaching the GUVs to BSA-biotin/streptavidin coated Lab-Tek® chambers. Lab-Tek® chambers were first filled with 200microL of Buffer (10 mM Tris, 100 mM NaCl, 0.1 M Glucose, pH=7.1) and then 40 µl of the suspension containing GUVs was added (16 nmol). After inspection of the GUVs quality, PGLa-g or Mag2-r (3.5 pmol) were added to the chamber at a final concentration of 13 nM (FCS and FCCS) or 18 nM (FCCS only) and 58 µM of lipids. The sample was left for 15 minutes to equilibrate after every addition of peptides.

Instrumentation for the FCS and FCCS is described in section 2.5.3. Auto- and cross-correlation curves were determined from the Z-scans measurements (sections 2.5.1 and 2.5.3) on at least two GUVs for every titration step (Figure 3.19). Both curves were analysed using the 2D3D model including triplet state as described by the equation (2.25). The amplitude of the cross-correlation curve $\left(G(0)_{rg} \right)$ relative to the amplitude of one of the autocorrelation curves $(G(0)_r)$ or $G(0)_g)$ is a direct measure of binding or dynamic colocalization:

$$\frac{G(0)_{rg}}{G(0)_r} = \frac{C_{RG}}{C_G} \tag{0.2}$$

$$\frac{G(0)_{rg}}{G(0)_g} = \frac{C_{RG}}{C_r} \tag{0.3}$$

where C_{RG}, C_G and C_r denotes the concentration of double labelled complex, concentration of all green-labelled species and concentration of all red-labelled species, respectively. Relations (0.2) and (0.3) are only true for uniformly labelled species, 1:1 binding stoichiometry and a setup with ideal detection volume overlap. In the case of incomplete overlap, correction factors can be introduced:
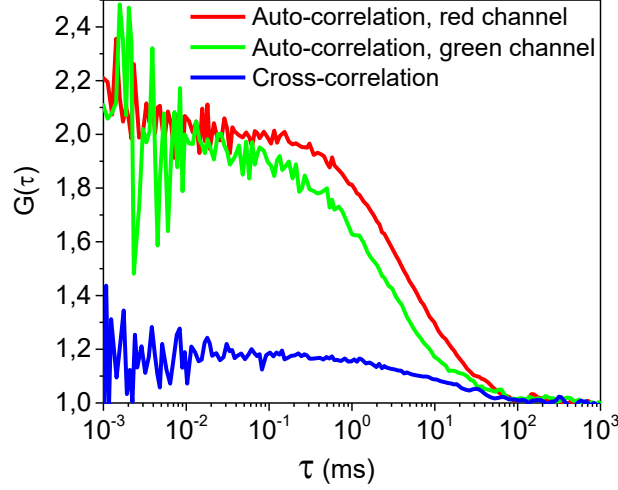
Figure 3.19: Auto- and cross-correlation curves for the red (Mag-r) and green (PGLa-g) channels and cross-correlation between these two signals (blue) obtained using a 1:1 mixture of PGLa-g and Mag2-r solutions (13nM) and 58 μM of POPE/POPG (2:1) GUVs.

$$f_{xr} \frac{G(0)_{rg}}{G(0)_r} = \frac{C_{RG}}{C_G} \tag{0.4}$$

$$f_{xg} \frac{G(0)_{rg}}{G(0)_g} = \frac{C_{RG}}{C_r} \tag{0.5}$$

We determined both correction factors using the method described in the section 2.5.2. We obtained $f_{xr} = 1.25$ and $f_{xg} = 1.41$.

Particle numbers (PNs) obtained from the analysis of the autocorrelation curves, were fitted using the model described by equation (2.27) resulting in the determination of the concentration of membrane bound peptides.

3.5.2 Cross-correlation measurements

Cross-correlation measurements were performed on the samples with the 1:1 concentration ratio of the both peptides (13 nM and 18 nM). Data were collected from at least 9 GUVs measurements and average values of the fraction of green (equation (0.4)) and red molecules (equation (0.5)) forming the membrane bound complex were calculated (Figure 3.20). The analysis of the cross-correlation curves revealed that approximately half of the membrane bound peptides, Mag2-r and PGLa-g, are involved in formation of Mag2-PGLa complex. However, the assumption made here, such as 1:1 complex stoichiometry, might not be correct. This is explored in the discussion below.
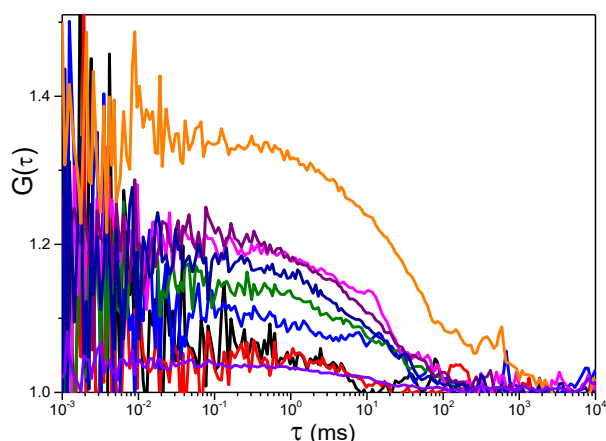
Figure 3.20: Cross-correlation functions obtained using a 1:1 mixture of PGLa-g and Mag2-r solutions (13 nM) and 58 μM of POPE/POPG (2:1) GUVs. Each curve represents measurement on different GUV.

3.5.3   Titration with unlabelled peptide

Samples consisting of GUVs and Mag2-r in solution were titrated with unlabelled PGLa till the ratio of total concentration of both peptides in the samples reaches 1:1. Figure 3.21A shows that the amount of bound Mag2-r increases upon titration with PGLa. Fitting the data revealed that the proportionality factor is 0.47±0.07 pmol/(m^2·nM).

Surprisingly, the reverse titration of PGLa with unlabelled Mag2 revealed that the amount of bound PGLa was not dependent on addition of Mag2 (Figure 3.21B).
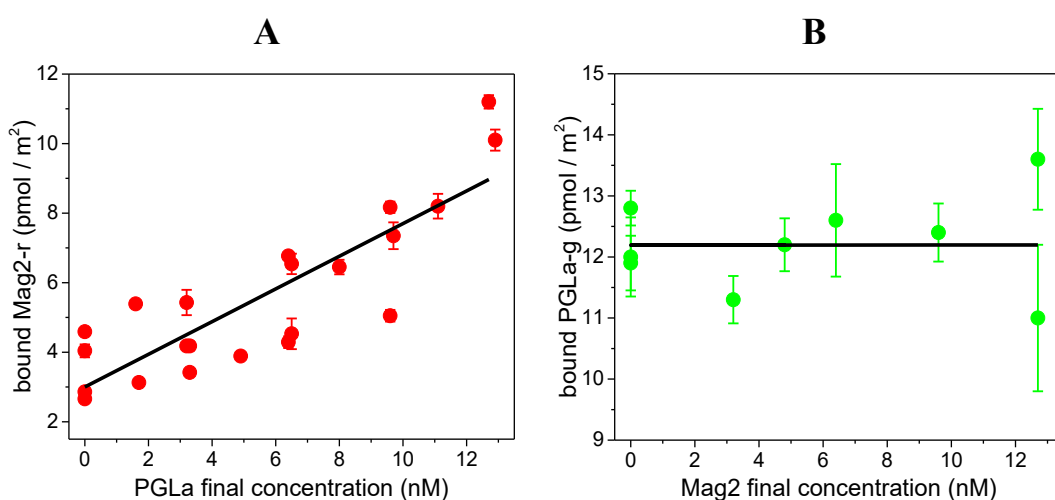

Figure 3.21: A) The amount of bound Mag2-r vs. final concentration of added unlabelled PGLa. Black line represents linear fit, where the slope parameter is 0.47±0.07 pmol/(m^2·nM). **B)** The amount of bound PGLa-g vs. final concentration of added unlabelled Mag2. Black line represents linear fit, with zero slope parameter.
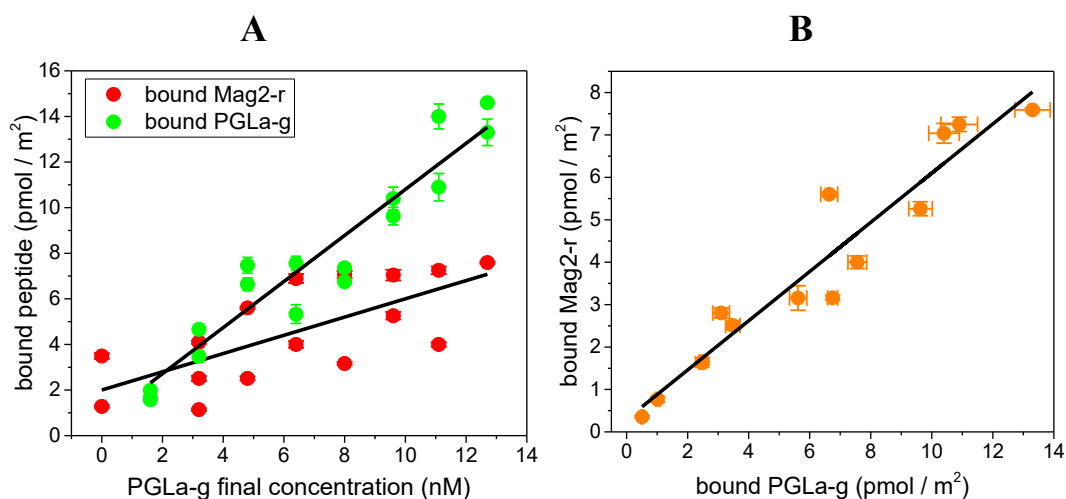
Figure 3.22: A) Amounts of bound peptides on bilayer vs. final concentration of PGLa-g in the sample. Black lines represent linear fits that yield the slopes 1.01 ± 0.08 pmol/(m^2·nM) and 0.4 ± 0.1 pmol/(m^2·nM) for PGLa-g and Mag2-r, respectively. **B)** The amount of bound Mag2-r vs. the amount of bound PGLa-g. Black line represents the linear fit with the slope of 0.58 ± 0.04.

3.5.4 Titration with labelled peptide

Mag2-r was titrated with PGLa-g till the final concentration ratio 1:1 (13 nM). The measurements were made in two-colour mode, i.e., data is obtained simultaneously for both peptides, for each particular GUV. Amount of bound PGLa-g increases with titration, as PGLa-g incorporates into the membrane. The proportionality factor determined by the linear fit is 1.01 ± 0.08 pmol/(m^2·nM). Amount of bound Mag2-r increases upon titration with PGLa-g, however, data points are more scattered compared to titration with unlabelled PGLa. Proportionality factor is similar to the Mag-r/PGLa titration (0.4 ± 0.1 pmol/(m^2·nM)), however, the total amount of bound Mag2 is slightly lower (Figure 3.22A).

Figure 3.22B shows that the amount of bound Mag2-r increases with the amount of bound PGLa-g. Linear fitting yields a slope of 0.58 ± 0.04. This fact suggests that the complexes form in a 3:2 (PGLa-g:Mag2-r) binding stoichiometry, assuming that the increasing of Mag2 binding to the membrane is driven entirely by the formation of complexes with membrane bound PGLa.

The titration with Mag2-r was also performed under the same experimental conditions as previous experiments. The amount of PGLa-g is independent of addition of Mag2-r (Figure 3.23), however, the data-points are considerably more scattered here compared to reverse titration (Figure 3.21B).
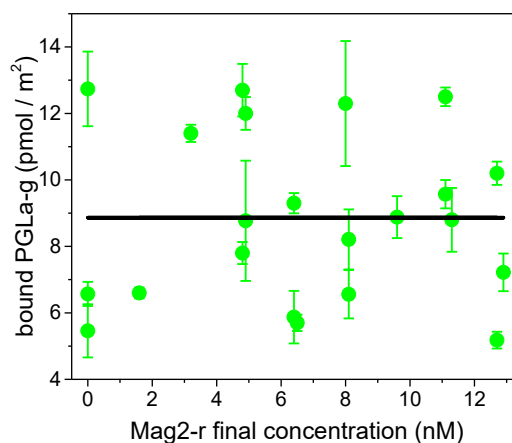
Figure 3.23: The amount of bound PGLa-g vs. final concentration of Mag2-r. Black line represents linear fit with zero slope parameter.

3.5.5　　Discussion

The FCCS data clearly shows that there is a cross-correlation between the green signal of the PGLa-g and the red signal from the Mag2-r. This data unequivocally shows that the two peptides form complexes that diffuse as one entity within the POPE/POPG (2:1) bilayer. The results also suggest there is a dynamic equilibrium between the bound peptide monomers and formed complexes within the membrane, since only approx. 50% of bound peptides (both Mag2 and PGLa) are involved in the formation of the complexes. However, this conclusion is yielded by using the equations (0.4) and (0.5) being only valid when there is 1:1 binding stoichiometry and provided the correction factors are correct. It should be noted that the correction factors were determined for a 3D system, not a planar one as is the case of the GUVs bilayer. Moreover, the 100% labelling of the peptide and no quenching of the dyes (FRET) were assumed. All these factors have to be also included for the proper analysis of FCCS. Unfortunately, problems during the preparation of the samples and lack of time, restricted us from performing further necessary experiments. Therefore, it is not beyond doubt that only 50% of membrane bound peptides form complexes.

Nevertheless, the FCCS results can be taken only as a confirmation of complex creation, which is further supported by the corresponding titration experiments (Figure 3.22). The titrations clearly show that the surface concentration of Mag2-r is proportional to the surface concentration of PGLa-g, by a factor of 0.58±0.04. Therefore, we can suggest a 3:2 (PGLa-g:Mag2-r) binding stoichiometry assuming

that the increase in binding of Mag2 upon addition of PGLa is driven by the formation of complexes with PGLa within the membrane. However, this suggestion is in contradiction with previous published results, where the binding stoichiometry is determined to be 1:1 [181]. Concerning the uncertainty of the FCS measurement and the uncertainty of the fit, more experiments concerning this stoichiometry binding ratio should be done to verify beyond doubt the true stoichiometry binding ratio.

Further titration experiments support the idea that the PGLa peptide increases the binding of Mag2 (Mag2-r) to the bilayer (Figure 3.21A), whereas the amount of bound PGLa (PGLa-g) is independent of the amount of Mag2 present (Figure 3.21B and Figure 3.23). Comparison between titration of Mag2-r with labelled and unlabelled PGLa shows that the increase in the amount of bound Mag2-r is slightly lower when using PGLa-g (0.47 ± 0.07 pmol/(m^2·nM) for PGLa unlabelled, and 0.4 ± 0.1 pmol/(m^2·nM) for PGLa-g). This effect could be caused by either the labelling of PGLa interfering with its binding equilibrium in a defined manner thus decreasing the amount of bound PGLa-g, compared to PGLa and therefore total amount of bound Mag2-r, or PGLa-g decreases the brightness of Mag2-r. However, the first value is within the error of the second one thus the effect is small and could be considered insignificant.

The amount of PGLa-g bound to the bilayer varies in a linear fashion, within the range tested, increasing by a factor of 1 relative to the increase in the bulk final concentration of PGLa (Figure 3.22A). This result also supports the idea that incorporation of PGLa into the membrane is independent of the presence of Mag2.

Fluorescence and dye-leakage experiments showed that the mixture of Mag2 and PGLa possesses the same mechanism of action as the individual peptides and exhibits faster pore formation but moderate pore lifetime [177, 181]. This synergistic effect of Mag2 and PGLa could be connected to the fact that PGLa enhances the binding of Mag2 to the membrane as the titration experiments showed. Moreover, FCCS results show without doubt that there is a complex formation between the two peptides, even though we cannot state beyond doubt what is the binding stoichiometry.

Bibliography

[1]   TURRO, Nicolas J. *Modern molecular photochemistry*. B.m.: University Science Books, 1991. ISBN 978-0935702712.

[2]   PARSON, William W. *Modern Optical Spectroscopy* [online]. Berlin, Heidelberg: Springer Berlin Heidelberg, 2007. ISBN 978-3-540-95895-6. Available at: doi:10.1007/978-3-540-37542-5

[3]   ATKINS, Peter and Ronald FRIEDMAN. *Molecular quantum mechanics*. B.m.: Oxford University Press, USA, 2005. ISBN 0--19--927498--3.

[4]   VALEUR, Bernard. *Molecular Fluorescence* [online]. Weinheim, FRG: Wiley-VCH Verlag GmbH, 2001. ISBN 352729919X. Available at: doi:10.1002/3527600248

[5]   STRICKLER, S. J. and Robert a. BERG. Relationship between Absorption Intensity and Fluorescence Lifetime of Molecules. *The Journal of Chemical Physics* [online]. 1962, **37**(4), 814–822. ISSN 0021-9606. Available at: doi:10.1063/1.1733166

[6]   M.HOF, R.HUTTERER and V. FIDLER. *Springer Series on Fluorescence: Methods and application. Fluorescence Spectroscopy in Biology*. 2004. ISBN 354022338X.

[7]   MARONCELLI, Mark, Richard S FEE, Curtis F CHAPMAN and Graham R FLEMING. Comment on 'dynamic Stokes shift in coumarin: is it only relaxation?' *The Journal of Physical Chemistry* [online]. 1991, **95**(2), 1012–1014. ISSN 0022-3654. Available at: doi:10.1021/j100155a096

[8]   HIRAYAMA, Satoshi and David PHILLIPS. Correction for refractive index in the comparison of radiative lifetimes in vapour and solution phases. *Journal of Photochemistry* [online]. 1980, **12**(2), 139–145. ISSN 00472670. Available at: doi:10.1016/0047-2670(80)85036-2

[9]   CHUNG, Pei-Hua, Carolyn TREGIDGO and Klaus SUHLING. Determining a fluorophore's transition dipole moment from fluorescence lifetime measurements in solvents of varying refractive index. *Methods and Applications in Fluorescence* [online]. 2016, **4**(4), 45001. ISSN 2050-6120. Available at: doi:10.1088/2050-6120/4/4/045001

[10]   LAKOWICZ, Joseph R. *Principles of Fluorescence Spectroscopy* [online].

Boston, MA: Springer US, 2006. ISBN 978-0-387-31278-1. Available at: doi:10.1007/978-0-387-46312-4

[11]   DOOSE, Soren, Hannes NEUWEILER and Markus SAUER. Fluorescence Quenching by Photoinduced Electron Transfer: A Reporter for Conformational Dynamics of Macromolecules. *ChemPhysChem* [online]. 2009, **10**(9–10), 1389–1398. ISSN 1439-7641. Available at: doi:10.1002/cphc.200900238

[12]   KAPUSTA, Peter, Michael WAHL and Rainer ERDMANN. *Advanced Photon Counting* [online]. Cham: Springer International Publishing, 2015. Springer Series on Fluorescence. ISBN 978-3-319-15635-4. Available at: doi:10.1007/978-3-319-15636-1

[13]   WAHL, Michael. Time-correlated single photon counting. *Technical Note* [online]. 2014, 1–14. Available at: https://www.picoquant.com/images/uploads/page/files/7253/technote_tcspc .pdf

[14]   ISTRATOV, Andrei A and Oleg F VYVENKO. Exponential analysis in physical phenomena. *Review of Scientific Instruments* [online]. 1999, **70**(2), 1233–1257. Available at: doi:http://dx.doi.org/10.1063/1.1149581

[15]   CANNIZZO, A, O BRÄM, G ZGRABLIC, A TORTSCHANOFF, a Ajdarzadeh OSKOUEI, F VAN MOURIK and M CHERGUI. Femtosecond fluorescence upconversion setup with broadband detection in the ultraviolet. *Optics Letters* [online]. 2007, **32**(24), 3555. ISSN 0146-9592. Available at: doi:10.1364/OL.32.003555

[16]   CANNIZZO, Andrea, Ana Maria BLANCO-RODRIGUEZ A. M.GUEZ, Amal EL NAHHAS, Jakub ŠEBERA, Stanislav ZÁLIŠ, Antonín VLCEK JR. and Majed CHERGUI. Femtosecond Fluorescence and Intersystem Crossing in Rhenium(I) Carbonyl-Bipyridine Complexes. *Journal of the American Chemical Society* [online]. 2008, **130**(28), 8967–8974. Available at: doi:10.1021/ja710763w

[17]   KAWSKI, A and P BOJARSKI. Comments on the determination of excited state dipole moment of molecules using the method of solvatochromism. *Spectrochimica Acta Part A: Molecular and Biomolecular Spectroscopy* [online]. 2011, **82**(1), 527–528. ISSN 1386-1425. Available at: doi:10.1016/j.saa.2011.05.102

[18]   DESAI, Vani R., A.H. SIDARAI, Shirajahammad M. HUNAGUND, M.

BASANAGOUDA, R.M. MELAVANKI, R.H. FATTEPUR and J.S. KADADEVARMATH. Steady state absorption and fluorescence study: Estimation of ground and excited state dipole moments of newly synthesized pyridazin-3(2H)-one derivatives. *Journal of Molecular Liquids* [online]. 2016, **223**, 141–149. ISSN 01677322. Available at: doi:10.1016/j.molliq.2016.08.015

[19] JURKIEWICZ, P, L CWIKLIK, P JUNGWIRTH and M HOF. Lipid hydration and mobility: An interplay between fluorescence solvent relaxation experiments and molecular dynamics simulations. *Biochimie* [online]. 2012, **94**(1), 26–32. ISSN 03009084. Available at: doi:10.1016/j.biochi.2011.06.027

[20] JURKIEWICZ, Piotr, Jan SYKORA, Agnieszka OLZYNSKA, Jana HUMPOLICKOVA and Martin HOF. Solvent Relaxation in Phospholipid Bilayers: Principles and Recent Applications. *Journal of Fluorescence* [online]. 2005, **15**(6), 883–894. ISSN 1053-0509. Available at: doi:10.1007/s10895-005-0013-4

[21] HORNG, M L, J A GARDECKI, A PAPAZYAN and M MARONCELLI. Subpicosecond Measurements of Polar Solvation Dynamics: Coumarin 153 Revisited. *The Journal of Physical Chemistry* [online]. 1995, **99**(48), 17311–17337. Available at: doi:10.1021/j100048a004

[22] STRATT, Richard M and Mark MARONCELLI. Nonreactive Dynamics in Solution: The Emerging Molecular View of Solvation Dynamics and Vibrational Relaxation. *The Journal of Physical Chemistry* [online]. 1996, **100**(31), 12981–12996. Available at: doi:10.1021/jp9608483

[23] FURSE, K E and S A CORCELLI. Molecular Dynamics Simulations of DNA Solvation Dynamics. *The Journal of Physical Chemistry Letters* [online]. 2010, **1**(12), 1813–1820. Available at: doi:10.1021/jz100485e

[24] ARZHANTSEV, S, N ITO, M HEITZ and M MARONCELLI. Solvation dynamics of coumarin 153 in several classes of ionic liquids: cation dependence of the ultrafast component. *Chemical Physics Letters* [online]. 2003, **381**(3–4), 278–286. ISSN 0009-2614. Available at: doi:10.1016/j.cplett.2003.09.131

[25] RICHERT, R, F STICKEL, R S FEE and M MARONCELLI. Solvation dynamics and the dielectric response in a glass-forming solvent: from picoseconds to seconds. *Chemical Physics Letters* [online]. 1994, **229**(3), 302–308. ISSN 0009-2614. Available at: doi:10.1016/0009-2614(94)01032-3

[26] BRÄM, O., A. Ajdarzadeh OSKOUEI, A. TORTSCHANOFF, F. VAN

MOURIK, M. MADRID, J. ECHAVE, A. CANNIZZO and M. CHERGUI. Relaxation Dynamics of Tryptophan in Water: A UV Fluorescence Up-Conversion and Molecular Dynamics Study. *The Journal of Physical Chemistry A* [online]. 2010, **114**(34), 9034–9042. ISSN 1089-5639. Available at: doi:10.1021/jp101778u

[27] LI, Tanping. Validity of Linear Response Theory for Time-Dependent Fluorescence in Staphylococcus Nuclease. *The Journal of Physical Chemistry B* [online]. 2014, **118**(45), 12952–12959. ISSN 1520-6106. Available at: doi:10.1021/jp506599d

[28] AMARO, Mariana, Jan BREZOVSKÝ, Silvia KOVÁČOVÁ, Lukáš MAIER, Radka CHALOUPKOVÁ, Jan SÝKORA, Kamil PARUCH, Jiří DAMBORSKÝ and Martin HOF. Are Time-Dependent Fluorescence Shifts at the Tunnel Mouth of Haloalkane Dehalogenase Enzymes Dependent on the Choice of the Chromophore? *The Journal of Physical Chemistry B* [online]. 2013, **117**(26), 7898–7906. ISSN 1520-6106. Available at: doi:10.1021/jp403708c

[29] TRIPATHY, Jagnyaseni and Warren F BECK. Nanosecond-Regime Correlation Time Scales for Equilibrium Protein Structural Fluctuations of Metal-Free Cytochrome c from Picosecond Time-Resolved Fluorescence Spectroscopy and the Dynamic Stokes Shift. *The Journal of Physical Chemistry B* [online]. 2010, **114**(48), 15958–15968. Available at: doi:10.1021/jp1044964

[30] SIANO, Donald B. and David E. METZLER. Band Shapes of the Electronic Spectra of Complex Molecules. *The Journal of Chemical Physics* [online]. 1969, **51**(5), 1856–1861. ISSN 0021-9606. Available at: doi:10.1063/1.1672270

[31] SÝKORA, Jan, Petr SLAVÍČEK, Pavel JUNGWIRTH, Justyna BARUCHA and Martin HOF. Time-Dependent Stokes Shifts of Fluorescent Dyes in the Hydrophobic Backbone Region of a Phospholipid Bilayer: Combination of Fluorescence Spectroscopy and Ab Initio Calculations. *The Journal of Physical Chemistry B* [online]. 2007, **111**(21), 5869–5877. ISSN 1520-6106. Available at: doi:10.1021/jp0719255

[32] YANG, Min and Ranko RICHERT. Observation of heterogeneity in the nanosecond dynamics of a liquid. *The Journal of Chemical Physics* [online]. 2001, **115**(6), 2676–2680. ISSN 0021-9606. Available

at: doi:10.1063/1.1380206

[33]   SÝKORA, Jan, Piotr JURKIEWICZ, Richard M. EPAND, Ruud KRAAYENHOF, Marek LANGNER and Martin HOF. Influence of the curvature on the water structure in the headgroup region of phospholipid bilayer studied by the solvent relaxation technique. *Chemistry and Physics of Lipids* [online]. 2005, **135**(2), 213–221. ISSN 00093084. Available at: doi:10.1016/j.chemphyslip.2005.03.003

[34]   RIEBER, K., J. SÝKORA, A. OLŻYŃSKA, R. JELINEK, G. CEVC and M. HOF. The use of solvent relaxation technique to investigate headgroup hydration and protein binding of simple and mixed phosphatidylcholine/surfactant bilayer membranes. *Biochimica et Biophysica Acta (BBA) - Biomembranes* [online]. 2007, **1768**(5), 1050–1058. ISSN 00052736. Available at: doi:10.1016/j.bbamem.2006.12.018

[35]   JURKIEWICZ, Piotr, Agnieszka OLŻYŃSKA, Marek LANGNER and Martin HOF. Headgroup Hydration and Mobility of DOTAP/DOPC Bilayers: A Fluorescence Solvent Relaxation Study. *Langmuir* [online]. 2006, **22**(21), 8741–8749. ISSN 0743-7463. Available at: doi:10.1021/la061597k

[36]   FEE, R S and M MARONCELLI. Estimating the time-zero spectrum in time-resolved emmsion measurements of solvation dynamics. *Chemical Physics* [online]. 1994, **183**(2–3), 235–247. ISSN 0301-0104. Available at: doi:10.1016/0301-0104(94)00019-0

[37]   FEE, Richard S, John A MILSOM and Mark MARONCELLI. Inhomogeneous decay kinetics and apparent solvent relaxation at low temperatures. *The Journal of Physical Chemistry* [online]. 1991, **95**(13), 5170–5181. ISSN 0022-3654. Available at: doi:10.1021/j100166a048

[38]   SYKORA, Jan, Jan BREZOVSKY, Tana KOUDELAKOVA, Maryna LAHODA, Andrea FORTOVA, Tatsiana CHERNOVETS, Radka CHALOUPKOVA, Veronika STEPANKOVA, Zbynek PROKOP, Ivana Kuta SMATANOVA, Martin HOF and Jiri DAMBORSKY. Dynamics and hydration explain failed functional transformation in dehalogenase design. *Nature Chemical Biology* [online]. 2014, **10**(6), 428–430. ISSN 1552-4450. Available at: doi:10.1038/nchembio.1502

[39]   SÝKORA, J., P. KAPUSTA, V. FIDLER and M. HOF. On What Time Scale Does Solvent Relaxation in Phospholipid Bilayers Happen? *Langmuir* [online].

2002, **18**(3), 571–574. ISSN 0743-7463. Available at: doi:10.1021/la011337x

[40] ERNSTING, Nikolaus P, Jens BREFFKE, Dmitry Yu VOROBYEV, David a DUNCAN and Inga PFEFFER. Sub-picosecond fluorescence evolution of amino-cyano-stilbenes in methanol: polar solvation obeys continuum theory without evidence of twisting. *Physical chemistry chemical physics : PCCP* [online]. 2008, **10**(15), 2043–9. ISSN 1463-9076. Available at: doi:10.1039/b717541h

[41] SAJADI, Mohsen, Thorsten OBERNHUBER, Sergey A. KOVALENKO, Manuel MOSQUERA, Bernhard DICK and Nikolaus P. ERNSTING. Dynamic Polar Solvation Is Reported by Fluorescing 4-Aminophthalimide Faithfully Despite H-Bonding. *The Journal of Physical Chemistry A* [online]. 2009, **113**(1), 44–55. ISSN 1089-5639. Available at: doi:10.1021/jp807605b

[42] SCHWILLE, Petra and Elke HAUSTEIN. *Fluorescence Correlation Spectroscopy An Introduction to its Concepts and Applications*. 2003

[43] KRICHEVSKY, Oleg and Grégoire BONNET. Fluorescence correlation spectroscopy: the technique and its applications. *Reports on Progress in Physics* [online]. 2002, **65**(2), 251–297. ISSN 0034-4885. Available at: doi:10.1088/0034-4885/65/2/203

[44] RIGLER, R., U. METS, J. WIDENGREN and P. KASK. Fluorescence correlation spectroscopy with high count rate and low background: analysis of translational diffusion. *European Biophysics Journal* [online]. 1993, **22**(3), 169–175. ISSN 0175-7571. Available at: doi:10.1007/BF00185777

[45] IVANCHENKO, Sergey and Don C LAMB. Fluorescence Correlation Spectroscopy: Principles and Developments. In: Jasminka BRNJAS-KRALJEVIĆ and Greta PIFAT-MRZLJAK, eds. *Supramolecular Structure and Function 10* [online]. Dordrecht: Springer Netherlands, 2011, p. 1–30. ISBN 978-94-007-0893-8. Available at: doi:10.1007/978-94-007-0893-8_1

[46] HAUSTEIN, Elke and Petra SCHWILLE. Fluorescence Correlation Spectroscopy: Novel Variations of an Established Technique. *Annual Review of Biophysics and Biomolecular Structure* [online]. 2007, **36**(1), 151–169. ISSN 1056-8700. Available at: doi:10.1146/annurev.biophys.36.040306.132612

[47] RIES, Jonas and Petra SCHWILLE. Fluorescence correlation spectroscopy. *BioEssays* [online]. 2012, **34**(5), 361–368. ISSN 02659247. Available

at: doi:10.1002/bies.201100111

[48] BENDA, A., M. BENEŠ, V. MAREČEK, A. LHOTSKÝ, W. Th HERMENS and M. HOF. How to determine diffusion coefficients in planar phospholipid systems by confocal fluorescence correlation spectroscopy. *Langmuir* [online]. 2003, **19**(10), 4120–4126. ISSN 07437463. Available at: doi:10.1021/la0270136

[49] MACHÁŇ, Radek and Martin HOF. Lipid diffusion in planar membranes investigated by fluorescence correlation spectroscopy. *Biochimica et Biophysica Acta (BBA) - Biomembranes* [online]. 2010, **1798**(7), 1377–1391. ISSN 00052736. Available at: doi:10.1016/j.bbamem.2010.02.014

[50] HAUSTEIN, Elke and Petra SCHWILLE. Single-molecule spectroscopic methods. *Current Opinion in Structural Biology* [online]. 2004, **14**(5), 531–540. ISSN 0959440X. Available at: doi:10.1016/j.sbi.2004.09.004

[51] ŠTEFL, Martin, Anna KUŁAKOWSKA and Martin HOF. Simultaneous Characterization of Lateral Lipid and Prothrombin Diffusion Coefficients by Z-Scan Fluorescence Correlation Spectroscopy. *Biophysical Journal* [online]. 2009, **97**(3), L1–L3. ISSN 00063495. Available at: doi:10.1016/j.bpj.2009.05.031

[52] BACIA, Kirsten and Petra SCHWILLE. Practical guidelines for dual-color fluorescence cross-correlation spectroscopy. *Nature Protocols* [online]. 2007, **2**(11), 2842–2856. ISSN 1754-2189. Available at: doi:10.1038/nprot.2007.410

[53] FOO, Yong Hwee, Nikolaus NAREDI-RAINER, Don C. LAMB, Sohail AHMED and Thorsten WOHLAND. Factors Affecting the Quantification of Biomolecular Interactions by Fluorescence Cross-Correlation Spectroscopy. *Biophysical Journal* [online]. 2012, **102**(5), 1174–1183. ISSN 00063495. Available at: doi:10.1016/j.bpj.2012.01.040

[54] RIES, Jonas, Zdeněk PETRÁŠEK, Anna J GARCÍA-SÁEZ and Petra SCHWILLE. A comprehensive framework for fluorescence cross-correlation spectroscopy. *New Journal of Physics* [online]. 2010, **12**(11), 113009. ISSN 1367-2630. Available at: doi:10.1088/1367-2630/12/11/113009

[55] BACIA, Kirsten, Sally A KIM and Petra SCHWILLE. Fluorescence cross-correlation spectroscopy in living cells. *Nature Methods* [online]. 2006, **3**(2), 83–89. ISSN 1548-7091. Available at: doi:10.1038/nmeth822

[56] VERMA, Sachin Dev, Nibedita PAL, Moirangthem Kiran SINGH and Sobhan

SEN. Sequence-Dependent Solvation Dynamics of Minor-Groove Bound Ligand Inside Duplex-DNA. *The journal of physical chemistry. B* [online]. 2015 [accessed. 2015-08-11]. ISSN 1520-5207. Available at: doi:10.1021/acs.jpcb.5b01977

[57] WILSON, James N and Eric T KOOL. Fluorescent DNA base replacements: reporters and sensors for biological systems. *Organic & Biomolecular Chemistry* [online]. 2006, **4**(23), 4265. ISSN 1477-0520. Available at: doi:10.1039/b612284c

[58] WILHELMSSON, L Marcus. Fluorescent nucleic acid base analogues. *Quarterly Reviews of Biophysics* [online]. 2010, **43**(2), 159–183. ISSN 0033-5835. Available at: doi:10.1017/S0033583510000090

[59] WILCOX, Jennifer L and Philip C. BEVILACQUA. A Simple Fluorescence Method for p K a Determination in RNA and DNA Reveals Highly Shifted p K a 's. *Journal of the American Chemical Society* [online]. 2013, **135**(20), 7390–7393. ISSN 0002-7863. Available at: doi:10.1021/ja3125299

[60] WAHBA, Alexander S., Abbasali ESMAEILI, Masad J. DAMHA and Robert H E HUDSON. A single-label phenylpyrrolocytidine provides a molecular beacon-like response reporting HIV-1 RT RNase H activity. *Nucleic Acids Research* [online]. 2010, **38**(3), 1048–1056. ISSN 0305-1048. Available at: doi:10.1093/nar/gkp1022

[61] TOKUGAWA, Munefumi, Yoshiaki MASAKI, Jan Christian CANGGADIBRATA, Kazuhei KANEKO, Takashi SHIOZAWA, Takashi KANAMORI, Morten GRØTLI, L Marcus WILHELMSSON, Mitsuo SEKINE and Kohji SEIO. 7-(Benzofuran-2-yl)-7-deazadeoxyguanosine as a fluorescence turn-ON probe for single-strand DNA binding protein. *Chem. Commun.* [online]. 2016, **52**(19), 3809–3812. ISSN 1359-7345. Available at: doi:10.1039/C5CC09700B

[62] SU, Xin, Xianjin XIAO, Chen ZHANG and Meiping ZHAO. Nucleic Acid Fluorescent Probes for Biological Sensing. *Applied Spectroscopy* [online]. 2012, **66**(11), 1249–1262. ISSN 00037028. Available at: doi:10.1366/12-06803

[63] SINKELDAM, Renatus W., Nicholas J. GRECO and Yitzhak TOR. Fluorescent Analogs of Biomolecular Building Blocks: Design, Properties, and Applications. *Chemical Reviews* [online]. 2010, **110**(5), 2579–2619. ISSN 0009-2665. Available at: doi:10.1021/cr900301e

[64] SHOLOKH, Marianna, Rajhans SHARMA, Dongwon SHIN, Ranjan DAS, Olga A. ZAPOROZHETS, Yitzhak TOR and Yves MÉLY. Conquering 2-Aminopurine's Deficiencies: Highly Emissive Isomorphic Guanosine Surrogate Faithfully Monitors Guanosine Conformation and Dynamics in DNA. *Journal of the American Chemical Society* [online]. 2015, **137**(9), 3185–3188. ISSN 0002-7863. Available at: doi:10.1021/ja513107r

[65] NADLER, André, Julian STROHMEIER and Ulf DIEDERICHSEN. 8-Vinyl-2′-deoxyguanosine as a Fluorescent 2′-Deoxyguanosine Mimic for Investigating DNA Hybridization and Topology. *Angewandte Chemie International Edition* [online]. 2011, **50**(23), 5392–5396. ISSN 14337851. Available at: doi:10.1002/anie.201100078

[66] MING, Xin and Frank SEELA. A Nucleobase-Discriminating Pyrrolo-dC Click Adduct Designed for DNA Fluorescence Mismatch Sensing. *Chemistry - A European Journal* [online]. 2012, **18**(31), 9590–9600. ISSN 09476539. Available at: doi:10.1002/chem.201103385

[67] KIM, Ki Tae and Byeang Hyean KIM. A fluorescent probe for the 3′-overhang of telomeric DNA based on competition between two interstrand G-quadruplexes. *Chemical Communications* [online]. 2013, **49**(17), 1717. ISSN 1359-7345. Available at: doi:10.1039/c3cc37504h

[68] KANAMORI, Takashi, Hiroki OHZEKI, Yoshiaki MASAKI, Akihiro OHKUBO, Mari TAKAHASHI, Kengo TSUDA, Takuhiro ITO, Mikako SHIROUZU, Kanako KUWASAKO, Yutaka MUTO, Mitsuo SEKINE and Kohji SEIO. Controlling the Fluorescence of Benzofuran-Modified Uracil Residues in Oligonucleotides by Triple-Helix Formation. *ChemBioChem* [online]. 2015, **16**(1), 167–176. ISSN 14394227. Available at: doi:10.1002/cbic.201402346

[69] HUDSON, Robert H E and Arash GHORBANI-CHOGHAMARANI. Oligodeoxynucleotides incorporating structurally simple 5-alkynyl-2′-deoxyuridines fluorometrically respond to hybridization. *Org. Biomol. Chem.* [online]. 2007, **5**(12), 1845–1848. ISSN 1477-0520. Available at: doi:10.1039/B705805E

[70] DZIUBA, Dmytro, Radek POHL and Michal HOCEK. Polymerase synthesis of DNA labelled with benzylidene cyanoacetamide-based fluorescent molecular rotors: fluorescent light-up probes for DNA-binding proteins. *Chem. Commun.*

[online]. 2015, **51**(23), 4880–4882. ISSN 1359-7345. Available at: doi:10.1039/C5CC00530B

[71] BEN GAIED, Nouha, Nicole GLASSER, Nick RAMALANJAONA, Hervé BELTZ, Philippe WOLFF, Roland MARQUET, Alain BURGER and Yves MÉLY. 8-vinyl-deoxyadenosine, an alternative fluorescent nucleoside analog to 2'-deoxyribosyl-2-aminopurine with improved properties. *Nucleic acids research* [online]. 2005, **33**(3), 1031–9. ISSN 1362-4962. Available at: doi:10.1093/nar/gki253

[72] WEBER, Gregorio and Fay J FARRIS. Synthesis and spectral properties of a hydrophobic fluorescent probe: 6-propionyl-2-(dimethylamino)naphthalene. *Biochemistry* [online]. 1979, **18**(14), 3075–3078. Available at: doi:10.1021/bi00581a025

[73] KIMURA, Takumi, Kiyohiko KAWAI and Tetsuro MAJIMA. Probing the microenvironments in the grooves of Z-DNA using dan-modified oligonucleotides. *Chemical communications (Cambridge, England)* [online]. 2006, (14), 1542–4. ISSN 1359-7345. Available at: doi:10.1039/b600026f

[74] KIMURA, Takumi, Kiyohiko KAWAI and Tetsuro MAJIMA. Monitoring of microenvironmental changes in the major and minor grooves of DNA by dan-modified oligonucleotides. *Organic letters* [online]. 2005, **7**(26), 5829–32. ISSN 1523-7060. Available at: doi:10.1021/ol052473m

[75] TAINAKA, Kazuki, Kazuo TANAKA, Shuji IKEDA, Ken-ichiro NISHIZA, Tomo UNZAI, Yoshimasa FUJIWARA, Isao SAITO and Akimitsu OKAMOTO. PRODAN-conjugated DNA: synthesis and photochemical properties. *Journal of the American Chemical Society* [online]. 2007, **129**(15), 4776–84. ISSN 0002-7863. Available at: doi:10.1021/ja069156a

[76] PAL, Nibedita, Him SHWETA, Moirangthem Kiran SINGH, Sachin Dev VERMA and Sobhan SEN. Power-Law Solvation Dynamics in G-Quadruplex DNA: Role of Hydration Dynamics on Ligand Solvation inside DNA. *The Journal of Physical Chemistry Letters* [online]. 2015, **6**(9), 1754–1760. ISSN 1948-7185. Available at: doi:10.1021/acs.jpclett.5b00653

[77] JIMENEZ, Ralph, Graham R FLEMING, P V KUMAR and M MARONCELLI. Femtosecond solvation dynamics of water. *Nature* [online]. 1994, **369**(6480), 471–473. Available at: http://dx.doi.org/10.1038/369471a0

[78] BRÁZDOVÁ, Marie, Jan PALECEK, Dmitry I CHERNY, Sabina BILLOVÁ,

Miroslav FOJTA, Petr PECINKA, Borivoj VOJTESEK, Thomas M JOVIN and Emil PALECEK. Role of tumor suppressor p53 domains in selective binding to supercoiled DNA. *Nucleic acids research*. 2002, **30**(22), 4966–74. ISSN 1362-4962.

[79] FOJTA, Miroslav, Hana PIVONKOVA, Marie BRAZDOVA, Katerina NEMCOVA, Jan PALECEK and Borivoj VOJTESEK. Investigations of the supercoil-selective DNA binding of wild type p53 suggest a novel mechanism for controlling p53 function. *European Journal of Biochemistry* [online]. 2004, **271**(19), 3865–3876. ISSN 00142956. Available at: doi:10.1111/j.1432-1033.2004.04323.x

[80] VERMA, Sachin Dev, Nibedita PAL, Moirangthem Kiran SINGH and Sobhan SEN. Probe Position-Dependent Counterion Dynamics in DNA: Comparison of Time-Resolved Stokes Shift of Groove-Bound to Base-Stacked Probes in the Presence of Different Monovalent Counterions. *The Journal of Physical Chemistry Letters* [online]. 2012, **3**(18), 2621–2626. ISSN 1948-7185. Available at: doi:10.1021/jz300934x

[81] SAJADI, Mohsen, Kristina E. FURSE, Xin Xing ZHANG, Lars DEHMEL, Sergey a. KOVALENKO, Steven a. CORCELLI and Nikolaus P. ERNSTING. Detection of DNA-ligand binding oscillations by stokes-shift measurements. *Angewandte Chemie - International Edition* [online]. 2011, **50**(40), 9501–9505. ISSN 14337851. Available at: doi:10.1002/anie.201102942

[82] DALLMANN, André, Matthias PFAFFE, Clemens MÜGGE, Rainer MAHRWALD, Sergey a KOVALENKO and Nikolaus P ERNSTING. Local THz time domain spectroscopy of duplex DNA via fluorescence of an embedded probe. *The journal of physical chemistry. B* [online]. 2009, **113**(47), 15619–28. ISSN 1520-5207. Available at: doi:10.1021/jp906037g

[83] BANERJEE, Debapriya and Samir Kumar PAL. Dynamics in the DNA Recognition by DAPI: Exploration of the Various Binding Modes. *The Journal of Physical Chemistry B* [online]. 2008, **112**(3), 1016–1021. ISSN 1520-6106. Available at: doi:10.1021/jp077090f

[84] ANDREATTA, Daniele, Sobhan SEN, J. Luis PÉREZ LUSTRES, Sergey a. KOVALENKO, Nikolaus P. ERNSTING, Catherine J. MURPHY, Robert S. COLEMAN and Mark a. BERG. Ultrafast dynamics in DNA: 'Fraying' at the end of the helix. *Journal of the American Chemical Society* [online]. 2006,

128(21), 6885–6892. ISSN 00027863. Available at: doi:10.1021/ja0582105

[85] PAL, Nibedita, Sachin Dev VERMA and Sobhan SEN. Probe position dependence of DNA dynamics: Comparison of the time-resolved Stokes shift of groove-bound to base-stacked probes. *Journal of the American Chemical Society* [online]. 2010, **132**(27), 9277–9279. ISSN 00027863. Available at: doi:10.1021/ja103387t

[86] DZIUBA, Dmytro, Piotr JURKIEWICZ, Marek CEBECAUER, Martin HOF and Michal HOCEK. A Rotational BODIPY Nucleotide: An Environment-Sensitive Fluorescence-Lifetime Probe for DNA Interactions and Applications in Live-Cell Microscopy. *Angewandte Chemie International Edition* [online]. 2016, **55**(1), 174–178. ISSN 14337851. Available at: doi:10.1002/anie.201507922

[87] SUN, Bingbing, Hong SHEN, Elsa BIOLOGICS and P O BOX. Controlling Surface-Induced Nanocomposites by Lipoplexes for Enhanced Gene Transfer. *Journal of Nanomaterials* [online]. 2015, **2015**, 1–13. ISSN 1687-4110. Available at: doi:10.1155/2015/784836

[88] KLYMCHENKO, Andrey S. and Yves MELY. Fluorescent Environment-Sensitive Dyes as Reporters of Biomolecular Interactions. In: *Progress in Molecular Biology and Translational Science* [online]. 1st ed. B.m.: Elsevier Inc., 2013, p. 35–58. ISBN 9780123869326. Available at: doi:10.1016/B978-0-12-386932-6.00002-8

[89] NOVAIRA, Mercedes, M Alicia BIASUTTI, Juana J SILBER and N Mariano CORREA. New Insights on the Photophysical Behavior of PRODAN in Anionic and Cationic Reverse Micelles: From Which State or States Does It Emit? *The Journal of Physical Chemistry B* [online]. 2007, **111**(4), 748–759. Available at: doi:10.1021/jp065528q

[90] GUHA, Soumi, Kalyanasis SAHU, Durba ROY, Sudip Kumar MONDAL, Siddhartha ROY and Kankan BHATTACHARYYA. Slow Solvation Dynamics at the Active Site of an Enzyme: Implications for Catalysis †. *Biochemistry* [online]. 2005, **44**(25), 8940–8947. ISSN 0006-2960. Available at: doi:10.1021/bi0473915

[91] SAMADDAR, Soma, Amit Kumar MANDAL, Sudip Kumar MONDAL, Kalyanasis SAHU, Kankan BHATTACHARYYA and Siddhartha ROY. Solvation Dynamics of a Protein in the Pre Molten Globule State. *The Journal*

of Physical Chemistry B [online]. 2006, **110**(42), 21210–21215. ISSN 1520-6106. Available at: doi:10.1021/jp064136g

[92]   SAXL, Tania, Faaizah KHAN, Daniel R MATTHEWS, Zheng-Liang ZHI, Olaf ROLINSKI, Simon AMEER-BEG and John PICKUP. Fluorescence lifetime spectroscopy and imaging of nano-engineered glucose sensor microcapsules based on glucose/galactose-binding protein. *Biosensors and Bioelectronics* [online]. 2009, **24**(11), 3229–3234. ISSN 0956-5663. Available at: doi:http://dx.doi.org/10.1016/j.bios.2009.04.003

[93]   BATABYAL, Subrata, Tanumoy MONDOL and Samir Kumar PAL. Picosecond-resolved solvent reorganization and energy transfer in biological and model cavities. *Biochimie* [online]. 2013, **95**(6), 1127–1135. ISSN 03009084. Available at: doi:10.1016/j.biochi.2012.12.018

[94]   BOULEY FORD, Nicole D., Dong Woo SHIN, Harry B. GRAY and Jay R. WINKLER. Intrachain contact dynamics in unfolded cytochrome cb 562. *Journal of Physical Chemistry B* [online]. 2013, **117**(42), 13206–13211. ISSN 15206106. Available at: doi:10.1021/jp403234h

[95]   YAMADA, Seiji, Nicole D BOULEY FORD, Gretchen E KELLER, William C FORD, Harry B GRAY and Jay R WINKLER. Snapshots of a protein folding intermediate. *Proceedings of the National Academy of Sciences of the United States of America* [online]. 2013, **110**(5), 1606–10. ISSN 1091-6490. Available at: doi:10.1073/pnas.1221832110/-/DCSupplemental.www.pnas.org/cgi/doi/10.1073/pnas.1221832110

[96]   TSALKOVA, Tamara N, Nadezhda Y DAVYDOVA, James R HALPERT and Dmitri R DAVYDOV. Mechanism of Interactions of alfa-Naphthoflavone with Cytochrome P450 3A4 Explored with an Engineered Enzyme Bearing a Fluorescent Probes. *Biochemistry* [online]. 2007, **46**(1), 106–119. Available at: doi:10.1021/bi061944p

[97]   MONDOL, Tanumoy, Subrata BATABYAL and Samir Kumar PAL. Ultrafast electron transfer in the recognition of different DNA sequences by a DNA-binding protein with different dynamical conformations. *Journal of Biomolecular Structure and Dynamics* [online]. 2012, **30**(3), 362–370. Available at: doi:10.1080/07391102.2012.680035

[98]   KISHAN, K V, M E NEWCOMER, T H RHODES and S D GUILLIOT. Effect of pH and salt bridges on structural assembly: molecular structures of the

monomer and intertwined dimer of the Eps8 SH3 domain. *Protein science : a publication of the Protein Society* [online]. 2001, **10**, 1046–1055. ISSN 0961-8368. Available at: doi:10.1110/ps.50401

[99] GIRVAN, Hazel M., Harriet E. SEWARD, Helen S. TOOGOOD, Myles R. CHEESMAN, David LEYS and Andrew W. MUNRO. Structural and Spectroscopic Characterization of P450 BM3 Mutants with Unprecedented P450 Heme Iron Ligand Sets: NEW HEME LIGATION STATES INFLUENCE CONFORMATIONAL EQUILIBRIA IN P450 BM3. *Journal of Biological Chemistry* [online]. 2007, **282**(1), 564–572. ISSN 0021-9258. Available at: doi:10.1074/jbc.M607949200

[100] GAGLIARDI, Christopher J., Robert A. BINSTEAD, H. Holden THORP and Thomas J. MEYER. Concerted Electron–Proton Transfer (EPT) in the Oxidation of Tryptophan with Hydroxide as a Base. *Journal of the American Chemical Society* [online]. 2011, **133**(49), 19594–19597. ISSN 0002-7863. Available at: doi:10.1021/ja207379n

[101] HARRIMAN, Anthony. Further comments on the redox potentials of tryptophan and tyrosine. *The Journal of Physical Chemistry* [online]. 1987, **91**(24), 6102–6104. ISSN 0022-3654. Available at: doi:10.1021/j100308a011

[102] STEWART, David J., Michael J. NAPOLITANO, Ekaterina V. BAKHMUTOVA-ALBERT and Dale W. MARGERUM. Kinetics and mechanisms of chlorine dioxide oxidation of tryptophan. *Inorganic Chemistry* [online]. 2008, **47**(5), 1639–1647. ISSN 00201669. Available at: doi:10.1021/ic701761p

[103] TOMMOS, Cecilia, Jack J. SKALICKY, Denis L. PILLOUD, A. Joshua WAND and P. Leslie DUTTON. De Novo Proteins as Models of Radical Enzymes †. *Biochemistry* [online]. 1999, **38**(29), 9495–9507. ISSN 0006-2960. Available at: doi:10.1021/bi990609g

[104] SCHEFER, Jurg, Robert MCDANIEL and Benno P SCHOENBORN. Small-angle neutron scattering studies on Brij-58 micelles. *The Journal of Physical Chemistry* [online]. 1988, **92**(3), 729–732. Available at: doi:10.1021/j100314a029

[105] JESENSKÁ, Andrea, Jan SÝKORA, Agnieszka OLŻYŃSKA, Jan BREZOVSKÝ, Zbyněk ZDRÁHAL, Jiří DAMBORSKÝ and Martin HOF. Nanosecond Time-Dependent Stokes Shift at the Tunnel Mouth of Haloalkane

Dehalogenases. *Journal of the American Chemical Society* [online]. 2009, **131**(2), 494–501. ISSN 0002-7863. Available at: doi:10.1021/ja804020q

[106] SENGUPTA, Bidisa, Jayanti GUHARAY and Pradeep K SENGUPTA. Characterization of the fluorescence emission properties of prodan in different reverse micellar environments. *Spectrochimica Acta Part A: Molecular and Biomolecular Spectroscopy* [online]. 2000, **56**(7), 1433–1441. ISSN 1386-1425. Available at: http://www.sciencedirect.com/science/article/pii/S1386142500002456

[107] DUNN, Alexander R, Anna-Maria A HAYS, David B GOODIN, C David STOUT, Richard CHIU, Jay R WINKLER and Harry B GRAY. Fluorescent Probes for Cytochrome P450 Structural Characterization and Inhibitor Screening. *Journal of the American Chemical Society* [online]. 2002, **124**(35), 10254–10255. ISSN 0002-7863. Available at: doi:10.1021/ja0271678

[108] CYMER, Florian, Gunnar VON HEIJNE and Stephen H. WHITE. Mechanisms of Integral Membrane Protein Insertion and Folding. *Journal of Molecular Biology* [online]. 2015, **427**(5), 999–1022. ISSN 00222836. Available at: doi:10.1016/j.jmb.2014.09.014

[109] VON HEIJNE, Gunnar. Membrane-protein topology. *Nature Reviews Molecular Cell Biology* [online]. 2006, **7**(12), 909–918. ISSN 1471-0072. Available at: doi:10.1038/nrm2063

[110] HUNTE, Carola and Sebastian RICHERS. Lipids and membrane protein structures. *CURRENT OPINION IN STRUCTURAL BIOLOGY* [online]. 2008, **18**(4), 406–411. ISSN 0959-440X. Available at: doi:10.1016/j.sbi.2008.03.008

[111] CYMER, Florian, Anbazhagan VEERAPPAN and Dirk SCHNEIDER. Transmembrane helix-helix interactions are modulated by the sequence context and by lipid bilayer properties. *Biochimica et Biophysica Acta - Biomembranes* [online]. 2012, **1818**(4), 963–973. ISSN 00052736. Available at: doi:10.1016/j.bbamem.2011.07.035

[112] LEE, Anthony G. How lipids affect the activities of integral membrane proteins. *Biochimica et Biophysica Acta (BBA) - Biomembranes* [online]. 2004, **1666**(1–2), 62–87. ISSN 00052736. Available at: doi:10.1016/j.bbamem.2004.05.012

[113] MARSH, Derek and László I HORVÁTH. Structure, dynamics and composition of the lipid-protein interface. Perspectives from spin-labelling. *Biochimica et Biophysica Acta (BBA) - Reviews on Biomembranes* [online].

1998, **1376**(3), 267–296. ISSN 03044157. Available at: doi:10.1016/S0304-4157(98)00009-4

[114] LUNDBÆK, Jens A., Pia BIRN, Anker J. HANSEN, Rikke SØGAARD, Claus NIELSEN, Jeffrey GIRSHMAN, Michael J. BRUNO, Sonya E. TAPE, Jan EGEBJERG, Denise V. GREATHOUSE, Gwendolyn L. MATTICE, Roger E. KOEPPE and Olaf S. ANDERSEN. Regulation of Sodium Channel Function by Bilayer Elasticity. *The Journal of General Physiology* [online]. 2004, **123**(5), 599–621. ISSN 0022-1295. Available at: doi:10.1085/jgp.200308996

[115] APELL, H-J. Structure-function relationship in P-type ATPases--a biophysical approach. *Reviews of physiology, biochemistry and pharmacology* [online]. 2003, **150**, 1–35. ISSN 0303-4240. Available at: doi:10.1007/s10254-003-0018-9

[116] PALMGREN, M G and P NISSEN. P-type ATPases. *Annu Rev Biophys* [online]. 2011, **40**, 243–266. ISSN 1936-122X. Available at: doi:10.1146/annurev.biophys.093008.131331

[117] BUBLITZ, Maike, Maria MUSGAARD, Hanne POULSEN, Lea THØGERSEN, Claus OLESEN, Birgit SCHIØTT, J. Preben MORTH, Jesper Vuust MØLLER and Poul NISSEN. Ion pathways in the sarcoplasmic reticulum Ca2+-ATPase. *Journal of Biological Chemistry* [online]. 2013, **288**(15), 10759–10765. ISSN 00219258. Available at: doi:10.1074/jbc.R112.436550

[118] TOYOSHIMA, Chikashi. How Ca2+-ATPase pumps ions across the sarcoplasmic reticulum membrane. *Biochimica et Biophysica Acta - Molecular Cell Research* [online]. 2009, **1793**(6), 941–946. ISSN 01674889. Available at: doi:10.1016/j.bbamcr.2008.10.008

[119] STARLING, a P, J M EAST and a G LEE. Effects of phosphatidylcholine fatty acyl chain length on calcium binding and other functions of the (Ca(2+)-Mg2+)-ATPase. *Biochemistry* [online]. 1993, **32**(6), 1593–600. ISSN 0006-2960. Available at: doi:10.1021/bi00057a025

[120] THØGERSEN, Lea and Poul NISSEN. Flexible P-type ATPases interacting with the membrane. *Current Opinion in Structural Biology* [online]. 2012, **22**(4), 491–499. ISSN 0959440X. Available at: doi:10.1016/j.sbi.2012.05.009

[121] GOURDON, Pontus, Xiang-Yu LIU, Tina SKJØRRINGE, J Preben MORTH, Lisbeth Birk MØLLER, Bjørn Panyella PEDERSEN and Poul NISSEN. Crystal structure of a copper-transporting PIB-type ATPase. *Nature* [online]. 2011,

475(7354), 59–64. ISSN 0028-0836. Available at: doi:10.1038/nature10191

[122] ANDERSSON, Magnus, Daniel MATTLE, Oleg SITSEL, Tetyana KLYMCHUK, Anna Marie NIELSEN, Lisbeth Birk MØLLER, Stephen H WHITE, Poul NISSEN and Pontus GOURDON. Copper-transporting P-type ATPases use a unique ion-release pathway. *Nature structural & molecular biology* [online]. 2014, **21**(1), 43–8. ISSN 1545-9985. Available at: doi:10.1038/nsmb.2721

[123] MATTLE, Daniel, Limei ZHANG, Oleg SITSEL, Lotte Thue PEDERSEN, Maria Rosa MONCELLI, Francesco TADINI-BUONINSEGNI, Pontus GOURDON, Douglas C REES, Poul NISSEN and Gabriele MELONI. A sulfur-based transport pathway in Cu+-ATPases. *EMBO reports* [online]. 2015, **16**(6), 728–740. ISSN 1469-221X. Available at: doi:10.15252/embr.201439927

[124] MAHMMOUD, Yasser A., Wojciech KOPEC and Himanshu KHANDELI. K+ Congeners That Do Not Compromise Na+ Activation of the Na+,K+-ATPase Hydration of the ion binding cavity likely controls ion selectivity. *Journal of Biological Chemistry* [online]. 2015, **290**(6), 3720–3731. ISSN 1083351X. Available at: doi:10.1074/jbc.M114.577486

[125] LI, Jing, Saher A SHAIKH, Giray ENKAVI, Po-chao WEN, Zhijian HUANG and Emad TAJKHORSHID. Transient formation of water-conducting states in membrane transporters. *Proceedings of the National Academy of Sciences of the United States of America* [online]. 2013, **110**(19), 7696–7701. ISSN 1091-6490. Available at: doi:10.1073/pnas.1218986110

[126] LIANG, Xu, John MACK, Li-Min ZHENG, Zhen SHEN and Nagao KOBAYASHI. Phosphorus(V)-Corrole: Synthesis, Spectroscopic Properties, Theoretical Calculations, and Potential Utility for in Vivo Applications in Living Cells. *Inorganic Chemistry* [online]. 2014, **53**(6), 2797–2802. ISSN 0020-1669. Available at: doi:10.1021/ic402347w

[127] AVIV-HAREL, Iris and Zeev GROSS. Coordination chemistry of corroles with focus on main group elements. *Coordination Chemistry Reviews* [online]. 2011, **255**(7–8), 717–736. ISSN 00108545. Available at: doi:10.1016/j.ccr.2010.09.013

[128] ZHANG, Lei, Zi-Yu LIU, Xuan ZHAN, Li-Li WANG, Hui WANG and Hai-Yang LIU. Photophysical properties of electron-deficient free-base corroles bearing meso-fluorophenyl substituents. *Photochem. Photobiol. Sci.* [online].

2015, **14**(5), 953–962. ISSN 1474-905X. Available at: doi:10.1039/C5PP00060B

[129] KNYUKSHTO, Valeriy N., Thien Huynh NGO, Wim DEHAEN, Wouter MAES and Mikalai M. KRUK. Phosphorescence of free base corroles. *RSC Adv.* [online]. 2016, **6**(50), 43911–43915. ISSN 2046-2069. Available at: doi:10.1039/C6RA06196F

[130] SOLL, Matan, Kolanu SUDHAKAR, Natalia FRIDMAN, Alexander MÜLLER, Beate RÖDER and Zeev GROSS. One-Pot Conversion of Fluorophores to Phosphorophores. *Organic Letters* [online]. 2016, **18**(22), 5840–5843. ISSN 1523-7060. Available at: doi:10.1021/acs.orglett.6b02877

[131] AGADJANIAN, Hasmik, Jun MA, Altan RENTSENDORJ, Vinod VALLURIPALLI, Jae Youn HWANG, Atif MAHAMMED, Daniel L FARKAS, Harry B GRAY, Zeev GROSS and Lali K MEDINA-KAUWE. Tumor detection and elimination by a targeted gallium corrole. *Proceedings of the National Academy of Sciences* [online]. 2009, **106**(15), 6105–6110. ISSN 0027-8424. Available at: doi:10.1073/pnas.0901531106

[132] BLUMENFELD, Carl M., Robert H. GRUBBS, Rex A. MOATS, Harry B. GRAY and Karn SORASAENEE. Decorating Metal Oxide Surfaces with Fluorescent Chlorosulfonated Corroles. *Inorganic Chemistry* [online]. 2013, **52**(9), 4774–4776. ISSN 0020-1669. Available at: doi:10.1021/ic400410k

[133] PRIBISKO, Melanie, Joshua PALMER, Robert H GRUBBS, Harry B GRAY, John TERMINI and Punnajit LIM. Cellular uptake and anticancer activity of carboxylated gallium corroles. *Proceedings of the National Academy of Sciences* [online]. 2016, **113**(16), E2258–E2266. ISSN 0027-8424. Available at: doi:10.1073/pnas.1517402113

[134] TEO, Ruijie D., Jae Youn HWANG, John TERMINI, Zeev GROSS and Harry B. GRAY. Fighting Cancer with Corroles. *Chemical Reviews* [online]. 2017, **117**(4), 2711–2729. ISSN 0009-2665. Available at: doi:10.1021/acs.chemrev.6b00400

[135] SUDHAKAR, Kolanu, Lingamallu GIRIBABU, Paolo SALVATORI and Filippo De ANGELIS. Triphenylamine-functionalized corrole sensitizers for solar-cell applications. *physica status solidi (a)* [online]. 2015, **212**(1), 194–202. ISSN 18626300. Available at: doi:10.1002/pssa.201431169

[136] WALKER, Don, Shlomit CHAPPEL, Atif MAHAMMED, Bruce S.

BRUNSCHWIG, Jay R. WINKLER, Harry B. GRAY, Arie ZABAN and Zeev GROSS. Corrole-sensitized TiO 2 solar cells. *Journal of Porphyrins and Phthalocyanines* [online]. 2006, **10**(11), 1259–1262. ISSN 1088-4246. Available at: doi:10.1142/S1088424606000624

[137] SINHA, Woormileela, Luca RAVOTTO, Paola CERONI and Sanjib KAR. NIR-emissive iridium(iii) corrole complexes as efficient singlet oxygen sensitizers. *Dalton Trans.* [online]. 2015, **44**(40), 17767–17773. ISSN 1477-9226. Available at: doi:10.1039/C5DT03041B

[138] POHL, J., I. SALTSMAN, A. MAHAMMED, Z. GROSS and Beate RÖDER. Inhibition of green algae growth by corrole-based photosensitizers. *Journal of Applied Microbiology* [online]. 2015, **118**(2), 305–312. ISSN 13645072. Available at: doi:10.1111/jam.12690

[139] ANUSHA, P. T., Debasis SWAIN, S. HAMAD, L. GIRIBABU, T. Shuvan PRASHANT, Surya P. TEWARI and S. Venugopal RAO. Ultrafast Excited-State Dynamics and Dispersion Studies of Third-Order Optical Nonlinearities in Novel Corroles. *The Journal of Physical Chemistry C* [online]. 2012, **116**(33), 17828–17837. ISSN 1932-7447. Available at: doi:10.1021/jp305497b

[140] MAHAMMED, Atif and Zeev GROSS. Albumin-Conjugated Corrole Metal Complexes: Extremely Simple Yet Very Efficient Biomimetic Oxidation Systems. *Journal of the American Chemical Society* [online]. 2005, **127**(9), 2883–2887. ISSN 0002-7863. Available at: doi:10.1021/ja045372c

[141] HABER, Adi, Hasmik AGADJANIAN, Lali K. MEDINA-KAUWE and Zeev GROSS. Corroles that bind with high affinity to both apo and holo transferrin. *Journal of Inorganic Biochemistry* [online]. 2008, **102**(3), 446–457. ISSN 01620134. Available at: doi:10.1016/j.jinorgbio.2007.10.026

[142] LEMON, Christopher M., Robert L. HALBACH, Michael HUYNH and Daniel G. NOCERA. Photophysical Properties of β-Substituted Free-Base Corroles. *Inorganic Chemistry* [online]. 2015, **54**(6), 2713–2725. ISSN 0020-1669. Available at: doi:10.1021/ic502860g

[143] FLAMIGNI, Lucia and Daniel T GRYKO. Photoactive corrole-based arrays. *Chem. Soc. Rev.* [online]. 2009, **38**(6), 1635–1646. Available at: doi:10.1039/B805230C

[144] NASTASI, Francesco, Sebastiano CAMPAGNA, Thien H NGO, Wim DEHAEN, Wouter MAES and Mikalai KRUK. Luminescence of meso-

pyrimidinylcorroles: relationship with substitution pattern and heavy atom effects. *Photochem. Photobiol. Sci.* [online]. 2011, **10**(1), 143–150. ISSN 1474-905X. Available at: doi:10.1039/C0PP00282H

[145] VENTURA, Barbara, Alessandra DEGLI ESPOSTI, Beata KOSZARNA, Daniel T. GRYKO and Lucia FLAMIGNI. Photophysical characterization of free-base corroles, promising chromophores for light energy conversion and singlet oxygen generation. *New Journal of Chemistry* [online]. 2005, **29**(12), 1559. ISSN 1144-0546. Available at: doi:10.1039/b507979a

[146] KOWALSKA, Dorota, Xia LIU, Umakanta TRIPATHY, Atif MAHAMMED, Zeev GROSS, Satoshi HIRAYAMA and Ronald P STEER. Ground- and Excited-State Dynamics of Aluminum and Gallium Corroles. *Inorganic Chemistry* [online]. 2009, **48**(6), 2670–2676. ISSN 0020-1669. Available at: doi:10.1021/ic900056n

[147] LIU, Xia, Atif MAHAMMED, Umakanta TRIPATHY, Zeev GROSS and Ronald P. STEER. Photophysics of Soret-excited tetrapyrroles in solution. III. Porphyrin analogues: Aluminum and gallium corroles. *Chemical Physics Letters* [online]. 2008, **459**(1–6), 113–118. ISSN 00092614. Available at: doi:10.1016/j.cplett.2008.05.038

[148] SINGH-RACHFORD, Tanya N. and Felix N. CASTELLANO. Photon upconversion based on sensitized triplet–triplet annihilation. *Coordination Chemistry Reviews* [online]. 2010, **254**(21–22), 2560–2573. ISSN 00108545. Available at: doi:10.1016/j.ccr.2010.01.003

[149] MCCLURE, Donald S. Triplet-Singlet Transitions in Organic Molecules. Lifetime Measurements of the Triplet State. *The Journal of Chemical Physics* [online]. 1949, **17**(10), 905–913. ISSN 0021-9606. Available at: doi:10.1063/1.1747085

[150] RAAVI, Sai Santosh Kumar, Jun YIN, Giulia GRANCINI, Cesare SOCI, Venugopal Rao SOMA, Guglielmo LANZANI and Lingamallu GIRIBABU. Femtosecond to Microsecond Dynamics of Soret-Band Excited Corroles. *The Journal of Physical Chemistry C* [online]. 2015, **119**(52), 28691–28700. ISSN 1932-7447. Available at: doi:10.1021/acs.jpcc.5b08235

[151] RABINOVICH, Elena, Israel GOLDBERG and Zeev GROSS. Gold(I) and Gold(III) Corroles. *Chemistry - A European Journal* [online]. 2011, **17**(44), 12294–12301. ISSN 09476539. Available at: doi:10.1002/chem.201102348

[152] PALMER, Joshua H., Alec C. DURRELL, Zeev GROSS, Jay R. WINKLER and Harry B. GRAY. Near-IR Phosphorescence of Iridium(III) Corroles at Ambient Temperature. *Journal of the American Chemical Society* [online]. 2010, **132**(27), 9230–9231. ISSN 0002-7863. Available at: doi:10.1021/ja101647t

[153] VESTFRID, Jenya, Mark BOTOSHANSKY, Joshua H PALMER, Alec C DURRELL, Harry B GRAY and Zeev GROSS. Iodinated Aluminum(III) Corroles with Long-Lived Triplet Excited States. *Journal of the American Chemical Society* [online]. 2011, **133**(33), 12899–12901. Available at: doi:10.1021/ja202692b

[154] VESTFRID, Jenya, Israel GOLDBERG and Zeev GROSS. Tuning the Photophysical and Redox Properties of Metallocorroles by Iodination. *Inorganic Chemistry* [online]. 2014, **53**(19), 10536–10542. ISSN 0020-1669. Available at: doi:10.1021/ic501585a

[155] CANNIZZO, Andrea, Frank VAN MOURIK, Wojciech GAWELDA, Goran ZGRABLIC, Christian BRESSLER and Majed CHERGUI. Broadband Femtosecond Fluorescence Spectroscopy of [Ru(bpy)3]2+. *Angewandte Chemie International Edition* [online]. 2006, **45**(19), 3174–3176. ISSN 1433-7851. Available at: doi:10.1002/anie.200600125

[156] MESSINA, Fabrizio, Enrico POMARICO, Mahsa SILATANI, Etienne BARANOFF and Majed CHERGUI. Ligand-Centred Fluorescence and Electronic Relaxation Cascade at Vibrational Time Scales in Transition-Metal Complexes. *The Journal of Physical Chemistry Letters* [online]. 2015, **6**(22), 4475–4480. ISSN 1948-7185. Available at: doi:10.1021/acs.jpclett.5b02146

[157] SHAO, Wenli, Hui WANG, Shuang HE, Lei SHI, Kaimei PENG, Yongfeng LIN, Lei ZHANG, Liangnian JI and Haiyang LIU. Photophysical Properties and Singlet Oxygen Generation of Three Sets of Halogenated Corroles. *The Journal of Physical Chemistry B* [online]. 2012, **116**(49), 14228–14234. ISSN 1520-6106. Available at: doi:10.1021/jp306826p

[158] SALNIKOV, Evgeniy S. and Burkhard BECHINGER. Lipid-Controlled Peptide Topology and Interactions in Bilayers: Structural Insights into the Synergistic Enhancement of the Antimicrobial Activities of PGLa and Magainin 2. *Biophysical Journal* [online]. 2011, **100**(6), 1473–1480. ISSN 00063495. Available at: doi:10.1016/j.bpj.2011.01.070

[159] ZASLOFF, Michael. Antimicrobial peptides of multicellular organisms. *Nature* [online]. 2002, **415**(6870), 389–395. ISSN 00280836. Available at: doi:10.1038/415389a

[160] WENZEL, Michaela, Alina Iulia CHIRIAC, Andreas OTTO, Dagmar ZWEYTICK, Caroline MAY, Catherine SCHUMACHER, Ronald GUST, H Bauke ALBADA, Maya PENKOVA, U. KRAMER, Ralf ERDMANN, Nils METZLER-NOLTE, Suzana K STRAUS, Erhard BREMER, Dörte BECHER, H. BROTZ-OESTERHELT, H.-G. SAHL and Julia Elisabeth BANDOW. Small cationic antimicrobial peptides delocalize peripheral membrane proteins. *Proceedings of the National Academy of Sciences* [online]. 2014, **111**(14), E1409–E1418. ISSN 0027-8424. Available at: doi:10.1073/pnas.1319900111

[161] BECHINGER, Burkhard. The SMART model: Soft Membranes Adapt and Respond, also Transiently, in the presence of antimicrobial peptides. *Journal of Peptide Science* [online]. 2015, **21**(5), 346–355. ISSN 10752617. Available at: doi:10.1002/psc.2729

[162] ULMSCHNEIDER, Jakob P., Jeremy C. SMITH, Martin B. ULMSCHNEIDER, Anne S. ULRICH and Erik STRANDBERG. Reorientation and Dimerization of the Membrane-Bound Antimicrobial Peptide PGLa from Microsecond All-Atom MD Simulations. *Biophysical Journal* [online]. 2012, **103**(3), 472–482. ISSN 00063495. Available at: doi:10.1016/j.bpj.2012.06.040

[163] BECHINGER, Burkhard. Insights into the mechanisms of action of host defence peptides from biophysical and structural investigations. *Journal of Peptide Science* [online]. 2011, **17**(5), 306–314. ISSN 10752617. Available at: doi:10.1002/psc.1343

[164] LOHNER, K. New strategies for novel antibiotics: peptides targeting bacterial cell membranes. *General Physiology and Biophysics* [online]. 2009, **28**(2), 105–116. ISSN 02315882. Available at: doi:10.4149/gpb_2009_02_105

[165] BECHINGER, Burkhard and Karl LOHNER. Detergent-like actions of linear amphipathic cationic antimicrobial peptides. *Biochimica et Biophysica Acta (BBA) - Biomembranes* [online]. 2006, **1758**(9), 1529–1539. ISSN 00052736. Available at: doi:10.1016/j.bbamem.2006.07.001

[166] STRANDBERG, Erik, Diana HORN, Sabine REISSE, Jonathan ZERWECK, Parvesh WADHWANI and Anne S. ULRICH. 2H-NMR and MD Simulations

Reveal Membrane-Bound Conformation of Magainin 2 and Its Synergy with PGLa. *Biophysical Journal* [online]. 2016, **111**(10), 2149–2161. ISSN 00063495. Available at: doi:10.1016/j.bpj.2016.10.012

[167] BECHINGER, Burkhard. Rationalizing the membrane interactions of cationic amphipathic antimicrobial peptides by their molecular shape. *Current Opinion in Colloid & Interface Science* [online]. 2009, **14**(5), 349–355. ISSN 13590294. Available at: doi:10.1016/j.cocis.2009.02.004

[168] AFONIN, Sergii, Stephan L GRAGE, Marco IERONIMO, Parvesh WADHWANI and Anne S ULRICH. Temperature-Dependent Transmembrane Insertion of the Amphiphilic Peptide PGLa in Lipid Bilayers Observed by Solid State 19 F NMR Spectroscopy. *Journal of the American Chemical Society* [online]. 2008, **130**(49), 16512–16514. ISSN 0002-7863. Available at: doi:10.1021/ja803156d

[169] STRANDBERG, Erik, Jonathan ZERWECK, Diana HORN, Günther PRITZ, Marina BERDITSCH, Jochen BÜRCK, Parvesh WADHWANI and Anne S. ULRICH. Influence of hydrophobic residues on the activity of the antimicrobial peptide magainin 2 and its synergy with PGLa. *Journal of Peptide Science* [online]. 2015, **21**(5), 436–445. ISSN 10752617. Available at: doi:10.1002/psc.2780

[170] STRANDBERG, Erik, Jonathan ZERWECK, Parvesh WADHWANI and Anne S. ULRICH. Synergistic Insertion of Antimicrobial Magainin-Family Peptides in Membranes Depends on the Lipid Spontaneous Curvature. *Biophysical Journal* [online]. 2013, **104**(6), L9–L11. ISSN 00063495. Available at: doi:10.1016/j.bpj.2013.01.047

[171] STRANDBERG, Erik, Pierre TREMOUILHAC, Parvesh WADHWANI and Anne S. ULRICH. Synergistic transmembrane insertion of the heterodimeric PGLa/magainin 2 complex studied by solid-state NMR. *Biochimica et Biophysica Acta (BBA) - Biomembranes* [online]. 2009, **1788**(8), 1667–1679. ISSN 00052736. Available at: doi:10.1016/j.bbamem.2008.12.018

[172] TREMOUILHAC, Pierre, Erik STRANDBERG, Parvesh WADHWANI and Anne S. ULRICH. Synergistic Transmembrane Alignment of the Antimicrobial Heterodimer PGLa/Magainin. *Journal of Biological Chemistry* [online]. 2006, **281**(43), 32089–32094. ISSN 0021-9258. Available at: doi:10.1074/jbc.M604759200

[173] SORAVIA, Emilia, Giuseppe MARTINI and Michael ZASLOFF. Antimicrobial properties of peptides from Xenopus granular gland secretions. *FEBS Letters* [online]. 1988, **228**(2), 337–340. ISSN 00145793. Available at: doi:10.1016/0014-5793(88)80027-9

[174] HOSKIN, David W. and Ayyalusamy RAMAMOORTHY. Studies on anticancer activities of antimicrobial peptides. *Biochimica et Biophysica Acta (BBA) - Biomembranes* [online]. 2008, **1778**(2), 357–375. ISSN 00052736. Available at: doi:10.1016/j.bbamem.2007.11.008

[175] CHINCHAR, V.G, L. BRYAN, U. SILPHADAUNG, E. NOGA, D. WADE and L. ROLLINS-SMITH. Inactivation of viruses infecting ectothermic animals by amphibian and piscine antimicrobial peptides. *Virology* [online]. 2004, **323**(2), 268–275. ISSN 00426822. Available at: doi:10.1016/j.virol.2004.02.029

[176] HELMERHORST, Eva J., Ingrid M. REIJNDERS, Wim VAN 'T HOF, Enno C.I VEERMAN and Arie V. NIEUW AMERONGEN. A critical comparison of the hemolytic and fungicidal activities of cationic antimicrobial peptides. *FEBS Letters* [online]. 1999, **449**(2–3), 105–110. ISSN 00145793. Available at: doi:10.1016/S0014-5793(99)00411-1

[177] PINO-ANGELES, Almudena, John M. LEVERITT and Themis LAZARIDIS. Pore Structure and Synergy in Antimicrobial Peptides of the Magainin Family. *PLOS Computational Biology* [online]. 2016, **12**(1), e1004570. ISSN 1553-7358. Available at: doi:10.1371/journal.pcbi.1004570

[178] STRANDBERG, Erik, Deniz TILTAK, Sebastian EHNI, Parvesh WADHWANI and Anne S. ULRICH. Lipid shape is a key factor for membrane interactions of amphipathic helical peptides. *Biochimica et Biophysica Acta (BBA) - Biomembranes* [online]. 2012, **1818**(7), 1764–1776. ISSN 00052736. Available at: doi:10.1016/j.bbamem.2012.02.027

[179] ZERWECK, Jonathan, Erik STRANDBERG, Jochen BÜRCK, Johannes REICHERT, Parvesh WADHWANI, Olga KUKHARENKO and Anne S. ULRICH. Homo- and heteromeric interaction strengths of the synergistic antimicrobial peptides PGLa and magainin 2 in membranes. *European Biophysics Journal* [online]. 2016, **45**(6), 535–547. ISSN 0175-7571. Available at: doi:10.1007/s00249-016-1120-7

[180] GLATTARD, Elise, Evgeniy S. SALNIKOV, Christopher AISENBREY and

Burkhard BECHINGER. Investigations of the synergistic enhancement of antimicrobial activity in mixtures of magainin 2 and PGLa. *Biophysical Chemistry* [online]. 2016, **210**, 35–44. ISSN 03014622. Available at: doi:10.1016/j.bpc.2015.06.002

[181] MATSUZAKI, Katsumi, Yasuyuki MITANI, Ken-ya AKADA, Osamu MURASE, Shuji YONEYAMA, Michael ZASLOFF and Koichiro MIYAJIMA. Mechanism of Synergism between Antimicrobial Peptides Magainin 2 and PGLa †. *Biochemistry* [online]. 1998, **37**(43), 15144–15153. ISSN 0006-2960. Available at: doi:10.1021/bi9811617

[182] MURZYN, Krzysztof, Tomasz RÓG and Marta PASENKIEWICZ-GIERULA. Phosphatidylethanolamine-Phosphatidylglycerol Bilayer as a Model of the Inner Bacterial Membrane. *Biophysical Journal* [online]. 2005, **88**(2), 1091–1103. ISSN 00063495. Available at: doi:10.1529/biophysj.104.048835

[183] AKASHI, K, H MIYATA, H ITOH and K KINOSITA. Preparation of giant liposomes in physiological conditions and their characterization under an optical microscope. *Biophysical Journal* [online]. 1996, **71**(6), 3242–3250. ISSN 00063495. Available at: doi:10.1016/S0006-3495(96)79517-6

List of Figures

List of Tables

List of Abbreviations

ADC	Analog-to-digital converter
AMP	Antimicrobial peptide
Badan	6-bromoacetyl-2-dimethylaminonaphthalene
BBO	β-barium borate crystal
CFD	Constant-fraction-discriminator
CM-B382	Badan-labelled cysteine at position 382 in LpCopA
CM-B384	Badan-labelled cysteine at position 384 in LpCopA
CMC	Critical micelle concentration
CPC	Cysteine-proline-cysteine motif
CYP	Badan-labelled cytochrome P450 mutant
DAS	Decay associated spectra
DNAFL	Fluorene labelled double stranded DNA
DOTAP	1,2-dioleoyl-3-trimethylammonium-propane
FC	Franck-Condon state
FCCS	Fluorescence cross-correlation spectroscopy
FCS	Fluorescence correlation spectroscopy
FLIM	Fluorescence lifetime imaging
FRET	Forster resonance energy transfer
FWHM	Full width at half maximum
GUV	Giant unilamellar vesicle
His	Histidine
IC	Internal conversion
ICT	Intramolecular charge transfer
IRF	Instrument-response-function
ISC	Intersystem crossing
LpCopA	Copper-transporting ATPase from Legionella pneumophila
LUMO	Lowest unoccupied molecular orbital
Mag2	Magainin 2
MCP	Microchannel plate
ND	Nanodisc
NHE	Normal hydrogen electrode
NL	Non-linear crystal

PE	Phosphatidylethanolamine
PET	Photon induced electron transfer
PG	Phosphatidylglycerol
PMT	Photomultiplier tubes
POPE	1-palmitoyl-2-oleoyl-sn-glycero-3-phosphoethanolamine
POPG	1-palmitoyl-2-oleoyl-sn-glycero-3-phosphoglycerol
Prodan	6-Propionyl-2-Dimethylaminonaphthalene
RET	Resonance energy transfer
SNR	Signal-to-noise ratio
SPAD	Single photon avalanche diode
SR	Solvent relaxation
SUV	Small unilamellar vesicle
SV	Stern-Volmer plot
SVD	Singular value decomposition
TAC	Time-to-amplitude converter
TCSPC	Time correlated single photon counting
TDC	Time-to-digital converter
TDFS	Time-dependent fluorescence shifts
TRES	Time-resolved emission spectra
Trp	Tryptophan

Attachments

Attachment I:

Dziuba, D.; Pospíšil, P.; Matyašovský, J.; Brynda, J.; Nachtigallová, D.; Rulíšek, L.; Pohl, R.; Hof, M.; Hocek, M. **Solvatochromic Fluorene-Linked Nucleoside and DNA as Color-Changing Fluorescent Probes for Sensing Interactions**. *Chem. Sci.* **2016**, *7* (9), 5775–5785.

Attachment II:

Pospíšil, P.; Luxem, K. E.; Ener, M.; Sýkora, J.; Kocábová, J.; Gray, H. B.; Vlček, A.; Hof, M. **Fluorescence Quenching of (Dimethylamino)naphthalene Dyes Badan and Prodan by Tryptophan in Cytochromes P450 and Micelles.** *J. Phys. Chem. B* **2014**, *118* (34), 10085–10091.

Attachment III:

Fischermeier, E.; Pospíšil, P.; Sayed, A.; Hof, M.; Solioz, M.; Fahmy, K. **Dipolar Relaxation Dynamics at the Active Site of an ATPase Regulated by Membrane Lateral Pressure.** *Angew. Chemie Int. Ed.* **2017**, *56* (5), 1269–1272.

Attachment IV

Pomarico, E.; Pospíšil, P.; Bouduban, M.; Vestfrid, J.; Gross, Z.; Záliš, S.; Chergui, M.; Vlček, A. **Heavy atom effects on excited-state dynamics of iodinated metallocorroles.** *In preparation*